# Simulations of Magnetic Reversal Properties in Granular Recording Media

**Matthew Ellis**

Doctor of Philosophy

University of York
Physics

September 2015

## ABSTRACT

With increasing demand for high density magnetic recording devices a paradigm shift is required to overcome the super-paramagnetic limit. By using a high anisotropy material, such as $L1_0$ FePt, and heat assisted magnetic recording the areal density can be taken well beyond 1 Tbit/in$^2$. For FePt the grains on which the data is stored can be reduced to 3nm in size before thermal noise becomes an issue. Therefore, the understanding of how magnetic grains of only a few nanometres in size behave and switch is highly important. Here an atomistic model of magnetic materials, based on the Heisenberg exchange interaction and localised classical atomic moments, is used to investigate the magnetic reversal properties of granular recording media. A detailed model for FePt, parametrised from *ab-initio* is presented and this is used to investigate the finite size effects in nanometre grains. Using this model, the finite size effects on the linear reversal regime is investigated. Comparing a model using the Landau-Lifshitz-Bloch macrospin equation to the atomistic results show that multi-scale modelling may be valid down to the 3 nm length scale. The intergranular exchange interaction between neighbouring grains is investigated using a model invoking the presence of magnetic impurities in the grain inter-layer. Using constrained Monte-Carlo methods the effective exchange is calculated for different impurity density, grain separation and temperature. Following this, helicity dependent all optical switching in granular FePt is investigated. The phase space for switching through the Inverse Faraday effect is explored. Using the Master equation, a model for thermal switching with magnetic circular dichroism is explored which qualitatively explains the induced magnetisation observed experimentally. Finally, the coupling of the spin and lattice system is modelled by combining spin and molecular dynamics. The coupling to the lattice excites magnons which appear to decay implying that some damping processes are occurring.

LIST OF CONTENTS

# LIST OF FIGURES

# LIST OF TABLES

# ACKNOWLEDGEMENTS

I would like to first thank my supervisor, Professor Roy Chantrell, who has enabled me to undertake this work. I owe him a great deal for his guidance and for the wealth of knowledge he has imparted to me throughout my years at York.

Secondly I would like to thank my family for their continuing support and their encouragement over many years study. Especially my parents, John and Linda, that have instilled in me a passion for science and computing and my wife, Katie, that has been my rock providing endless love and patience throughout.

Lastly I would like to thank my friends and colleagues in the Department of Physics, who have helped me along this research. I am particularly indebted to Tom Ostler, Joe Barker, Richard Evans and Sergiu Ruta who have taught me a lot over the years. I would also like to thank to thank Jake Tatman, Helen Wilson and Pete Dodd who have been steadfast friends for many years and made my time a York particularly enjoyable.

# DECLARATION

The author hereby declares that the work presented in this thesis is his own work, except for previous acknowledged contributions. This work has not previously been presented for an award at this, or any other, University. All sources are acknowledged as References. The following lists specific research that was done in collaboration with others.

The hybrid constrained-unconstrained Monte-Carlo method for the simulation of the granular nano-structures with a dilute magnetic inter-layer was developed and implemented by Dr Richard Evans for the atomistic spin dynamics software package, VAMPIRE. The calculations were performed by the author and are presented here.

The majority of this thesis has been presented at various conferences by the author and the following scientific articles stemmed from this research:

1. M. O. A. Ellis and R. W. Chantrell, "Switching times of nanoscale FePt: Finite size effects on the linear reversal mechanism," *Appl. Phys. Lett.*, **106**, 162407 (2015).

2. M. O. A. Ellis, R. F. L. Evans, T. A. Ostler, J. Barker, U. Atxitia, O. Chubykalo-Fesenko, and R. W. Chantrell, "The Landau Lifshitz equation in atomistic models," *Low Temperature Physics*, **41**, 705 (2015); Originally published in Russia in *Fizika Nizkikh Temperatur*, **41**, 9 (2015)

# 1

# INTRODUCTION

The unique properties of magnetic materials have made them invaluable for modern technology. In the recent 2014 magnetism roadmap[1] 12 different areas of research are highlighted over a broad range of topics from bio-medical applications to magnetic logic devices. Whilst these topics are diverse a strong theme remains, that of data storage using the orientation of the magnetisation to represent the binary logic states (bits). One topic in the 2014 magnetism roadmap of special interest on this theme is that of Heat Assisted Magnetic Recording (HAMR).

In the half century that magnetic recording has existed it has experienced a dramatic increase in its capacity to store information, driven by the ever expanding consumer market for data storage, which in 2007 had passed 295 optimally compressed exabytes ($2.95 \times 10^{20}$ bytes)[2]. This has been achieved by the miniaturisation of the required components and key breakthroughs, such as giant magneto-resistance[3, 4] which has allowed for better sensing of the recorded data. However further miniaturisation is becoming increasingly more difficult as the natural limit imposed by thermal fluctuations is restricting the current paradigm of magnetic recording. HAMR is one of the technologies in development by the magnetic recording industry to achieve higher storage densities beyond the current limit. This forms the motivation for this thesis whereby the properties of HAMR in granular media will be investigated using modelling techniques which simulate the magnetic properties and dynamics from an atomistic level[5].

## 1.1 THE FUTURE OF MAGNETIC RECORDING

The current paradigm for magnetic recording is known as perpendicular magnetic recording (PMR)[6], where data is stored onto magnetic grains on thin film platters with the up/down orientations of the magnetisation representing the binary 1s and 0s. This was a shift from the previous longitudinal recording with the aim of allowing

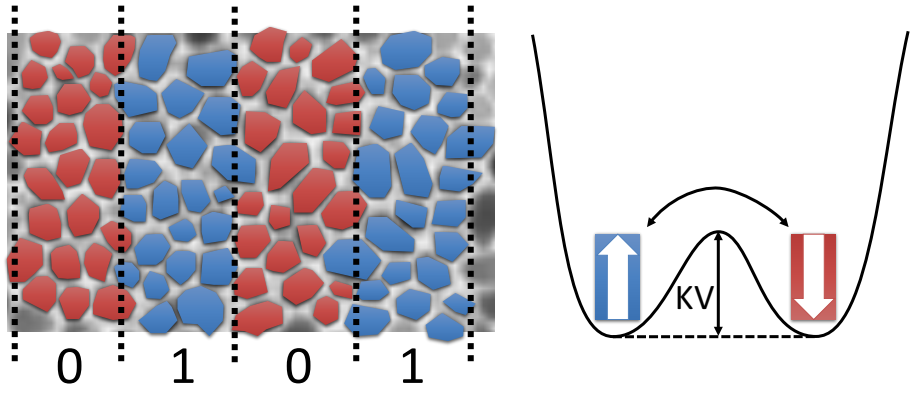


Figure 1.1.: (a) An example of a typical grain structure with data bits of different orientation. The size and shape of the grains can affect the bit boundaries. (b) The energy barrier between the orientations is given by the anisotropy energy barrier. Switching can occur with an applied field to overcome the barrier or if the barrier is low enough thermal fluctuations can switch the grains.

the grains to be more tightly packed giving a greater areal density (number of bits per unit area). An example of the granular media used is shown in figure 1.1.(a); a single bit of data is comprised of multiple grains with each grain separated from each other by a non-magnetic inter-layer (segregant). Due to the method of creating the granular media the grains are not uniformly shaped, this distribution in grain size and shape can play a big role in recording process. As figure 1.1.(a) shows the boundaries of each bit can become rough if there is a large size dispersion. Alongside the areal density, the stability of the stored data is a key factor, since it needs to be stored safely against thermal effects for a long time. The uniaxial anisotropy provides the energy barrier between the two magnetisation orientations (figure 1.1.(b)) and the characteristic thermal switching time between them is given by the Arrhenius-Neel law[7]:

$$\tau = \tau_0 \exp(K_u V / k_B T) \tag{1.1}$$

Here the $K_u$ is the uniaxial anisotropy constant and V the volume of a single grain. To achieve thermal stability over a timescale of decades the product of $K_u V / k_B T$ is required to be large. Typically the target for thermal stability is $K_u V / k_B T > 60$. This simple model shows that the desired reduction in the grain size would

lead to a loss of thermal stability. For the current generation of magnetic media used in devices the areal density would be limited at around 1000 Gb/in$^2$. This is known as the super-paramagnetic limit, since the magnetisation orientation would be dominated by the thermal fluctuations and behave paramagnetically. The solution to the super-paramagnetic limit would be to utilise a different magnetic medium with a higher anisotropy constant as this would give a smaller grain size before the magnetisation becomes thermally unstable. The drawback to this is the limitation of the the write field; not only is it required that the data written is stable for long periods it is also necessary to re-write the data regularly. The magnetic field generated by the write head is physically limited and so by employing high anisotropy media it may not be possible to overcome the coercive field. This is known as the magnetic recording trilemma since it is not possible with current generation devices to satisfy the three areas of minimising grain size, thermal stability and limited write field. Recently it has been expanded to a quadrilemma by Evans *et al.*[8] as the Bit Error Rate (BER) also constrains the system; which is shown schematically in figure 1.2. Evans *et al.* specifically studied the case for HAMR on bit patterned media where a single bit is stored a single grain and it is required that there is no backswitching of the magnetisation. It is found that there is a stronger constraint of the write field than simply exceeding the switching field to minimise this. In conventional media (with many grains per bit) this requirement is still relevant as it is still possible for individual grains to back-switch which reduces the net magnetisation of the bit, this is referred to dc noise.

To achieve areal densities beyond the current generation limit of 1000 Gb/in$^2$ requires a different scheme for magnetic storage. As described by Shiroshi *et al.*[9] there is a variety of different options with different benefits and drawbacks. The most popular future technology options are HAMR, Bit Patterned Magnetic Recording (BPMR) and Microwave Assisted Magnetic Recording (MAMR). HAMR and MAMR[10] both utilise high anisotropy media to achieve small grain sizes and the write phase is assisted to allow recording. In HAMR the writing is assisted by heating the media so that the coercivity drops below the available write field. MAMR uses an alternating field to excite precessional motion of the magnetisation to assist the write field. BPMR approaches the problem differently[11]; in BPMR advanced lithographic techniques are used to pattern the magnetic media into islands. Whilst the grain size is not minimised by having ordered arrays of islands a high signal to noise ratio is achieved with only a single island per bit.

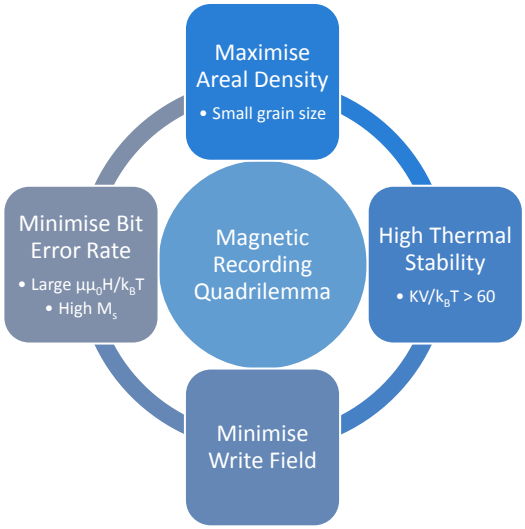


Figure 1.2.: The magnetic recording quadrilemma[8] showing competing factors reqired to develop high areal density devices.

An important part of these potential new magnetic recording devices is the choice of recording media. Both HAMR and MAMR require high anisotropy materials to provide thermal stability at the target areal density. Possible candidates are summarised by Weller *et al.*[12] and of particular interest to the industry is $L1_0$ phase FePt. $L1_0$ FePt exhibits an anisotropy of $K_u \approx 7.0 \times 10^6\,\mathrm{J\,m^{-3}}$ which is sufficient to support a minimum stable grain size of $D_p \approx 3\,\mathrm{nm}$. There is a significant interest in the properties of FePt to tailor it for magnetic recording[13–15]. Various studies of FePt have been performed over a variety of length scales, ranging from modelling nanoscale clusters[16, 17] to micro-magnetic models of granular media[18, 19], as well as extensive experimental analysis[10, 14, 15]. *Ab-initio* studies[20, 21] have shown that despite Pt being non-magnetic in the $L1_0$ crystal structure a moment is induced. Since Pt exhibits a high spin-orbit coupling this creates the enhanced anisotropy that is so desired for HAMR. Whilst *ab-initio* methods provide a detailed treatment of system it is limited in the number of atoms (a few hundred atoms) and length of time that can be simulated effectively. Therefore, an atomistic spin model[5, 22], which still retains the atomic level view of the system but can access system sizes up to the 10's nm scale, is ideal for investigating HAMR-related processes.

## 1.2 THESIS OUTLINE

In this thesis the properties relating the HAMR in granular media will be investigated. The aim is to probe these properties on the nanometre length scale for which the atomistic model is suited. Important areas are the linear reversal switching mechanism[23] which has been studied in bulk and large grains but not in grains close to the super-paramagnetic limit and inter-granular coupling in recording media[24, 25] which can play an important role in the stability of the grains. Later parts of the thesis deal with the emerging phenomena of magnetic recording using polarised light, and understanding the role the lattice plays in the magnetic damping. Recent reports of using a femto-second laser to switch the magnetisation in granular FePt[26] has not been completely understood and here the viability of the possible causes to the recorded magnetisation is analysed using the atomistic model of FePt. The role the lattice plays in the magnetisation damping requires an extended model; one where the atoms are free to move from their crystal positions to simulate the lattice effects. This model has been pioneered by Ma *et al.*[27] for bcc Fe and here we utilise this to investigate the induced damping and the effects the lattice causes on the magnetisation.

Following this introduction to the context and overview, the rest of the thesis is now outlined here. The second chapter details the atomistic model that is utilised throughout of the rest of the thesis. The atomistic Hamiltonian is discussed and further detail of the Hamiltonian for FePt is given. Details of the simulation methods are given for both atomistic spin dynamics and Monte-Carlo techniques and the chapter is completed with a some tests of the model.

The third chapter investigates the finite size effects that occur in FePt close to the super-paramagnetic limit. Particular focus is on the finite size effects on the reversal mechanism close to the Curie temperature. The equilibrium properties are calculated to connect the results from the atomistic model to predictions made from a micro-magnetic model. By comparing these a judgment of the possibility of multi-scale modelling on the nanometre scale is made.

In chapter four the atomistic model is used to calculate the inter-granular exchange using the constrained Monte-Carlo model. The atomistic model is used to construct an approximate granular media using hexagonal grains with magnetic impurities between the grains. By computing the free energy of rotating a grain against its neighbours the inter-granular exchange parameter required for micro-magnetic

calculations is found. The dependence of this parameter on impurity density, temperature and grain separation are calculated.

The fifth chapter deals with the recent phenomenon of switching in FePt granular media using circularly polarised femtosecond lasers. The two temperature model and the inverse Faraday effect are introduced to model the effect of the laser on the ferromagnet. The required strength and duration of the field generated by the inverse Faraday effect is calculated for various laser fluences. This shows that the field would need to last much longer than the laser pulse and so a simple model based on the Master equation is used to calculate the switching caused by magnetic circular dichroism. The resulting induced magnetisation agrees will with experimental measurements for an absorption difference of 3% between the different magnetisation orientations.

Chapter six describes an advanced atomistic model which incorporates the dynamics of the crystal lattice. The model Hamiltonian and the integration scheme based on a Suzuki-Trotter decomposition is described. The model is tested for basic energy and magnetisation conservation for the case without damping and the phonon and magnon spectra are calculated from the auto-correlation functions. Calculations of the coupling to the lattice through a psuedo-dipolar anisotropy term shows that magnons are generated at high k-vectors before decaying to the gamma point. The effect of free surfaces is also modelled showing that the surface relaxation alters the exchange coupling and triggers coherent phonons which couple to the magnetisation.

Following this conclusions are presented, summarising the main results of the thesis and their implications on the field.

# 2

# ATOMISTIC SPIN MODEL

To investigate the magnetic properties and dynamics of granular recording media we shall employ an atomistic spin model. This model considers permanent magnetic moments localised on each atomic site within the system of interest. Early work by Binder[28] using Monte-Carlo methods established spin models as valuable technique for investigating thermodynamic properties. More recently they have been adapted to investigate magnetisation dynamics at finite temperatures using the Landau-Lifshitz-Gilbert equation of motion and Langevin dynamics. This versatility has allows atomistic spin models to investigate out-of-equilibrium dynamic processes, such as the thermally induced magnetic switching in ferrimagnets,[29, 30] and for systems with complicated crystal structure[31]. They have also been used to investigate $L1_0$ FePt since it is simple to parameterise from *ab-initio* calculations[20]; this includes important microscopic effects that accurately predicts properties such as the bulk anisotropy strength and that it scales with $\propto M(T)^{2.1}$ which is important for its use in HAMR[32].

Atomistic models provide a bridge between the quantum *ab-initio* models, such as Density Functional Theory (DFT), and micro-magnetic models. As stated earlier, for *ab-initio* models system sizes of a few hundred atoms becomes computationally very hard; whilst micro-magnetic models are built within the long-wave length limit and so atomic level details, i.e. interfaces or small grains, cannot be treated effectively. Therefore, considering the focus of this investigation, atomistic spin models are ideally suited. A further advantage of the model is that thermal effects can be introduced and properties at elevated temperatures can be investigated. Whilst the model is essentially classical, as it is based on normalised Heisenberg spin vectors, quantum information can be included through the model parameters, allowing for a multi-scale approach. This however is one of the limitations of the model; the moments are have a fixed magnitude and localised to an atomic site. For most materials this is a reasonable assumption but other materials, with higher levels

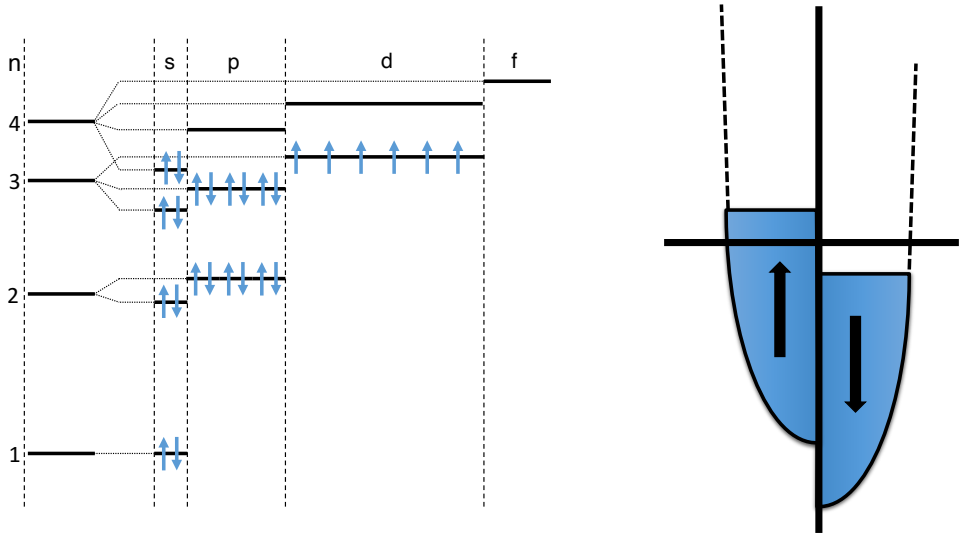


(a) Energy level diagram (b) Spin split band

Figure 2.1.: (a) The energy level diagram for an isolated atom with electrons filling the shells in order. By Hund's rules S is maximised first leaving unpaired electrons which form a net magnetic moment. (b) Spontaneous splitting of majority and minority spin bands in a ferromagnet due to the reduction in energy by forming an ordered state.

of delocalisation, are found disagree with experimental measurements. Extensive details on atomistic spin models are given in reviews by Evans *et al.*[5] and Skubic *et al.*[33] In this chapter the atomistic spin model will be detailed. This model is based on the interaction of atomic magnetic moments thus the general atomistic Hamiltonian, based on the Heisenberg Hamiltonian will be described. The specific Hamiltonian for the technologically important $L1_0$ FePt is also described. Following this the simulation methods, both the Langevin dynamics and constrained Monte Carlo methods, are introduced with tests of each presented.

## 2.1 LOCALISED ATOMIC MAGNETIC MOMENTS

In an atomistic spin model the ensemble is constructed as a set of magnetic moments that are localised to atomic positions. Typically these atoms form a crystalline structure with translational invariance but they may also exist in an approximated amorphous structure. To this end each atom has a position, $\mathbf{r}_i$, within the structure and a corresponding magnetic moment, $\boldsymbol{\mu}_i$. In isolated atoms these magnetic moments are formed from electrons in shells that are not full. Each orbital shell

has a set of spin states, $\mathbf{s}$ and an orbital angular momentum states, $l$, that can be occupied. Figure 2.1.(a) shows the energy level diagram for a isolated atom, the electrons fill up each band in order and with unpaired electrons (in this example in the 3d shell) a magnetic moment is formed. The spin and angular momenta of each electron in the shells combine to give a total spin and angular momentum: $\mathbf{S} = \sum_n \mathbf{s}_n, \mathbf{L} = \sum_n \mathbf{l}_n$. These are both angular momenta and contribute to the net magnetic moment through the total angular momentum, $\mathbf{J} = \mathbf{L} + \mathbf{S}$. According to this an atom will have a corresponding magnetic moment given by

$$\boldsymbol{\mu}_J = \mu_B g_J \mathbf{J} = \mu_B \left( g_L \mathbf{L} + g_S \mathbf{S} \right), \tag{2.1}$$

where $\mu_B = e\hbar/2m_e = 9.274\,16 \times 10^{-24}\,\mathrm{JT}^{-1}$ is the Bohr magneton and $g_J, g_L, g_S$ are the Landé splitting factors (g-factors).

The order in which the orbital state are filled is described empirically by Hund's rules[34, 35]. Hund's rules state that the order electrons occupy atomic orbitals such that

1. the multiplicity, $2S + 1$, is maximised;
2. for a given multiplicity, the total orbital angular, L, momentum is then maximised;
3. if the electron shell is less than half full then the total angular momentum, $J = |L - S|$ but if the shell is more than half full then $J = L + S$.

The first two rules are in essence a description of the minimisation of the Coulomb energy. For the first rule when the spins are aligned the spatial wave-function muse be anti-symmetric, which tends to keep the electrons further apart thus reducing the Coulomb energy. This gives rise to the exchange interaction which is one of the causes for ordering of the spins and is described in detail later on. The second rule is similar, in that by maximising $L$ the electrons are orbiting in the same direction, thus again reducing the Coulomb energy between electrons. The third rule is more complex as this is a statement of the spin-orbit coupling; this is a relativistic effect and in Hund's rules assumes what is known as L-S coupling rather than J-J coupling which is important in heavier nuclei. In L-S coupling the energy difference is proportional to $\mathbf{L} \cdot \mathbf{S}$ and depending on the coefficient will align parallel or anti-parallel. The sign of the coefficient changes when the shell is more than half full and so how $L$ and $S$ combine to form $J$ changes.

These rules give rise to a net magnetic moment for certain atoms which agrees well with the moments measured for localised electrons, such as the rare earth metals, but does not effectively describe the moments of some transition metals where the orbital angular momentum is quenched. Orbital quenching occurs in $3d$ transition metals due to the electrostatic field created by neighbouring atoms. This 'crystal field' is stronger than the spin orbit coupling in these metals and so the orbital momentum is minimised. Therefore for materials like Fe, Co and Ni the atomic magnetic moment is formed primarily by the spin magnetic moment, this leads to the convention of describing the atomic magnetic moments as spins. In this case the atomic magnetic moment is well described by

$$\boldsymbol{\mu} = \mu_s \mathbf{S} \tag{2.2}$$

where $\mu_s = g_S \mu_B$ is the magnitude of the magnetic moment. For rare earth metals the magnetism arises from electrons in the $4f$ shell, which are more localised and screened from the crystal field by the $5s^2 5p^6$ electrons. This means that the assumption that the spin-orbit coupling is higher still holds despite the crystal field and the orbital angular momentum contributes significantly to the net magnetic moment.

In metals the concept of isolated localised atoms does not work; the itinerant electrons play a significant role in their magnetism. The band theory of magnetism helps explain the difference between the experimentally measured values of the atomic magnetic moment and those theoretically predicted from the spin quantum number of the atoms, shown in figure 2.1.(b). Due to this splitting the minority electron band has a higher energy then the majority electron band. Therefore when the density of states is integrated up to the fermi energy then there is net difference between the number of majority and minority electrons. Since each electron has a magnetic moment of 1 $\mu_B$ the magnitude of the atomic moment will be

$$\mu_s = \mu_B \left( N_e^{\mathrm{maj}} - N_e^{\mathrm{min}} \right) \tag{2.3}$$

where $N_e^{\mathrm{maj}}$ and $N_e^{\mathrm{min}}$ are the number of majority and minority electrons obtained by integrating the spin-split projected density of states up to the Fermi energy. Within the atomistic picture the magnetic moments are assumed to act classically (S$\rightarrow \infty$) and are described by a 3D vector. The magnitude of the magnetic moment is assumed to be fixed which allows the moment to be normalised onto the unit sphere using

$$\mathbf{S} = \frac{\boldsymbol{\mu}}{\mu_s}. \tag{2.4}$$

## 2.2 GENERALISED ATOMISTIC HAMILTONIAN

In the last section, the atomistic magnetic moments were presented and now we consider how the they interact. The Hamiltonian here now only considers the spin degrees of freedom and a generalised Hamiltonian is

$$\mathcal{H} = \mathcal{H}_{\text{exch}} + \mathcal{H}_{\text{ani}} + \mathcal{H}_{\text{Zeeman}} + \mathcal{H}_{\text{dipole}} \tag{2.5}$$

The constituent terms in this expression are the exchange, anisotropy, Zeeman and dipole Hamiltonians which are described in more detail in the following.

### 2.2.1 *Exchange Interaction*

The exchange interaction is one of the strongest interactions in magnetism on the atomic scale and one of the most complex. It brings about magnetic ordering and a wide variety of effects depending on details of the interaction. The exchange interaction is a purely quantum mechanical property since it arises from the fermionic nature of the electrons. In general the exchange interaction is complex for systems containing many electrons; typical introductions[34, 35] to the exchange interaction consider a 2 electron system, such as the $H_2$ molecule or the He atom. Here a similar introduction is given. The $H_2$ molecule contains 2 nuclei at some separated with 2 electrons; since the electrons are spin $1/2$ they are fermions and as such require the total wave-function, $\Psi$, to be anti-symmetric under the exchange of the two electrons.

$$\Psi(1,2) = -\Psi(2,1), \tag{2.6}$$

where $1, 2$ indicates the position and spin variables of electrons 1 and 2 respectively. The total wave-function can be separated into a product of the spatial and spin wave-functions. In this case, either the total spatial wave-function, $\Phi$, or the total spin wave-function, $X$, can be anti-symmetric.

$$\Psi(1,2) = \begin{cases} \Phi_{\text{sym}}(1,2)X_{\text{anti}}(1,2) \\ \Phi_{\text{anti}}(1,2)X_{\text{sym}}(1,2) \end{cases} \tag{2.7}$$

The first case is known as the 'Singlet' state since the anti-symmetric spin wave-function has $S = 0$ and consequently the spin magnetic quantum number is $m_s = 0$. The wave-function in this case takes the form:

$$\Psi_{\mathrm{S}}(1,2) = \frac{1}{\sqrt{2}}\left[\phi_a(1)\phi_b(2) + \phi_a(2)\phi_b(1)\right]\left[\chi_\alpha(1)\chi_\beta(2) - \chi_\alpha(2)\chi_\beta(1)\right] \tag{2.8}$$

where $\phi_a(1)$ and $\phi_b(2)$ are the individual atomic wave functions occupied by either electron 1 or 2 on atoms a or b, and $\chi_\alpha$ and $\chi_\beta$ are the spin wave functions that represent either spin up or spin down. The second case is the 'Triplet' case where now S = 1 where the three possible spin states give rise to $m_s = 1, 0, -1$.

$$\Psi_{\mathrm{T}}(1,2) = \frac{1}{\sqrt{2}}\left[\phi_a(1)\phi_b(2) - \phi_a(2)\phi_b(1)\right]\begin{cases}\chi_\alpha(1)\chi_\alpha(2)\\ \chi_\alpha(1)\chi_\beta(2) + \chi_\alpha(2)\chi_\beta(1)\\ \chi_\beta(1)\chi_\beta(2)\end{cases} \tag{2.9}$$

The energy of each of these states can be calculated using an atomic Hamiltonian containing the Coulomb energy terms. The resulting energies are

$$E_{\mathrm{S}} = \mathcal{C} + \mathcal{J} \tag{2.10}$$

$$E_{\mathrm{T}} = \mathcal{C} - \mathcal{J} \tag{2.11}$$

where $\mathcal{C}$ and $\mathcal{J}$ are the Coulomb exchange integrals that are calculated using

$$\mathcal{C} = \int \phi_a^*(1)\phi_b^*(2)\hat{\mathcal{H}}\phi_a(1)\phi_b(2)d\mathbf{r}_1 d\mathbf{r}_2 \tag{2.12}$$

$$\mathcal{J} = \int \phi_a^*(1)\phi_b^*(2)\hat{\mathcal{H}}\phi_a(2)\phi_b(1)d\mathbf{r}_1 d\mathbf{r}_2 \tag{2.13}$$

The difference between the energy of the two states is

$$E_{\mathrm{S}} - E_{\mathrm{T}} = 2\mathcal{J} \tag{2.14}$$

So despite the Hamiltonian not containing any spin dependent terms the final energy of the two states are split depending on the parallel or anti-parallel alignment

of the spin. As Heisenberg showed it is easier to write the Hamiltonian with an explicit spin dependent term that takes the form:

$$\mathcal{H}_{\text{spin}} = -\mathcal{J}_{12}\mathbf{S}_1 \cdot \mathbf{S}_2 \tag{2.15}$$

For the $H_2$ molecule the Heisenberg exchange interaction is isotropic but in condensed matter systems it may not be so. Since the derivation of the exchange interaction is intractable analytically for a system with a large number of electrons the exchange constants are usually computed from *ab-initio* methods such as density functional theory[36, 37]. Consequently, it is convenient to consider a more general exchange interaction that is based off the Heisenberg form. In this case it can be written as the tensor product between two spins;

$$\mathcal{H}_{\text{exch}} = -\sum_{i,j} \mathbf{S}_i \mathbb{J}_{ij} \mathbf{S}_j \tag{2.16}$$

where $i, j$ label different spins. In this representation the exchange constant is tensorial thus as well as depending on distance and direction it may vary for different spin components. A more convenient expression of the exchange interaction is obtained by splitting the tensorial exchange in separate interactions that describe different behaviours. The tensor can be broken into three parts; isotropic, symmetric and anti-symmetric.

$$\mathcal{H}_{\text{exch}} = -\sum_{i,j} \left( J_{ij}^{\text{iso}} \mathbf{S}_i \cdot \mathbf{S}_j + \mathbf{S}_i \mathbb{J}_{ij}^{\text{sym}} \mathbf{S}_j + \mathbf{D}_{ij} \cdot (\mathbf{S}_i \times \mathbf{S}_j) \right) \tag{2.17}$$

The isotropic term is taken as the average of the diagonal elements of the tensor, given by:

$$J_{ij}^{\text{iso}} = \frac{1}{3} \text{Tr} \left( \mathbb{J}_{ij} \right) \tag{2.18}$$

This the dominant cause for the alignment and cooperative behaviour of the spins. Since it is isotropic the spins will align but there is no preferential orientation of the alignment direction. Whilst *ab-initio* calculations have shown the exchange constants can in general be long-ranged and anisotropic, it is reasonable for most materials to consider a nearest neighbour exchange interaction. In this case it is possible to extract the parameters from experimental measurements of the Curie temperature through the following expression

$$J_{ij}^{\text{iso}} = \frac{k_B T_C}{\varepsilon z} \tag{2.19}$$

where the number of neighbours is given by $z$. This expression utilises the empirical relationship between the strength of the exchange and the Curie temperature. The parameter, $\varepsilon$, describes the effect of the crystal structure on the relation and varies for different basic crystals.

The symmetric term is necessary when the diagonal terms in the exchange tensor are not equivalent and is defined as:

$$\mathbb{J}_{ij}^{\text{sym}} = \frac{1}{2}\left(\mathbb{J}_{ij} + \mathbb{J}_{ij}^{T}\right) - J_{ij}^{\text{iso}}\mathbb{I} \tag{2.20}$$

This is the anisotropic part of the exchange interaction and can provide a preferential orientation of the alignment. As described later this anisotropic exchange, also named 'two-ion anisotropy' is present in FePt and contributes a significant part of the overall anisotropy.

The final term in equation 2.17 is the anti-symmetric part of the exchange tensor, which is known as the Dzyaloshinskii-Moriya (DM) interaction [38, 39]. This way of writing the tensor shows that the spins will prefer to align perpendicular to each other and the DM vector, $\mathbf{D}_{ij}$. The DM vector is formed from the off-diagonal components of the exchange tensor:

$$\mathbf{D}_{ij} = \begin{pmatrix} J_{ij}^{yz} \\ J_{ij}^{xz} \\ J_{ij}^{xy} \end{pmatrix} \tag{2.21}$$

This interaction was described by Dzyaloshinskii[38] in an attempt to explain the weak ferromagnetism in Hematite through consideration of the crystal symmetry and a thermodynamic potential of the same form given above. Later it was shown by Moriya[39] that this arises from the spin-orbit coupling. The DM interaction between two spins occurs through a third atom with the super-exchange mechanism; for example in Hematite 2 Fe sites interact via the orbitals of a neighbouring O. In multi-layers it is common to find the DM interaction at interfaces where the symmetry is broken and another atomic species plays a role.[40]

The value of the exchange interaction can introduce different ordering properties in a magnetic system. Without the exchange interaction the magnetic moments do not have any ordering and behave in a manner known as paramagnetism. If the exchange interaction is positive then a parallel alignment of the spins is preferred which is known as ferromagnetism. If the exchange interaction is negative then an anti-parallel alignment is preferred which is known as anti-ferromagnetism. Paramagnets have no net magnetisation unless ordered with an external magnetic

field. Ferromagnets have a spontaneous magnetisation in zero field but collinear anti-ferromagnets, even though are ordered, do not show a magnetisation in zero field as the anti-parallel configuration leaves no net magnetisation.Weak ferromagnetism can be observed some anti-ferromagnets as the presence of another competing interaction, such as the DM interaction in Hematite, can create a canted anti-ferromagnet such that they magnetisation of each sub-lattice does not entirely cancel. A fourth kind exists, where the spins align anti-parallel but if different elements are present with magnetic moments of different sizes then a net magnetisation will be observed but behaves as a anti-ferromagnet, this is known as a ferrimagnetism.

For a ferromagnet the order parameter is simply the magnetisation ($\mathbf{M}$) or the reduced magnetisation ($\mathbf{m}$)

$$\mathbf{m} = \frac{\mathbf{M}}{M_s} = \frac{1}{M_s}\sum_i \mu_{s,i}\mathbf{S}_i \tag{2.22}$$

where $M_s$ is the saturation magnetisation which is usually taken as the sum of saturation magnetic moments in the system in the ground state configuration. At finite temperature there exists a ordered state below a critical temperature, which is known as the Curie temperature $T_C$. Temperature effects bring about disorder within the system so the magnetisation reduces steadily until close to the Curie temperature where a phase transition occurs and the magnetisation sharply drops to zero.

### 2.2.2 *Magneto-Crystalline Anisotropy*

The second term in the Hamiltonian is the anisotropy contribution which describes a preferential axis for the spins to point along. The exchange interaction provides an ordering of the spins within a material but it is the preferential alignment of the magnetisation along a direction that plays a key role in its usefulness for certain applications. In most systems the demagnetising field generated by the magnetisation is minimised when the magnetisation lies along the longest axes causing what is known as shape anisotropy. In thin films this forces the magnetisation to lie in plane. Of particular interest is the magneto-crystalline anisotropy; this is the preference to lie along certain crystallographic directions caused by the spin-orbit interaction[35].

There are different forms the anisotropy can take but the simplest ones to include are the uniaxial and cubic anisotropy given by[41, 42]:

$$\mathcal{H}_{\text{ani}} = -\sum_i k_u (\mathbf{S}_i \cdot \hat{\mathbf{e}}_u)^2 - \sum_i \frac{k_c}{2}(S_{ix}^4 + S_{iy}^4 + S_{iz}^4) \tag{2.23}$$

The axis is given by the unit vector $\hat{\mathbf{e}}_u$ and the constants $k_u$ and $k_c$ are the magnitudes of the interaction. In most systems the z-axis is taken as the anisotropy axis and depending on the sign of $k_u$ it can describe a preference to lie along the axis ($k_u > 0$) known as easy axis or to lie in the perpendicular plane ($k_u < 0$) known as easy plane. On the micro-magnetic scale the anisotropic part of the free energy per unit volume is given by

$$\mathcal{F}_{\text{aniso}}/M_s V = K_u \sin^2(\phi) + K_c \left(\alpha_x^2\alpha_y^2 + \alpha_x^2\alpha_y^2 + \alpha_y^2\alpha_z^2\right) \tag{2.24}$$

Here $K_u$ and $K_c$ are the uniaxial and cubic anisotropy constants with the uniaxial anisotropy along the z direction of the crystal and $\alpha_x, \alpha_y, \alpha_z$ are the directional cosines. In most cases it is satisfactory to only consider the uniaxial anisotropy as, certainly for the materials considered in this thesis, it dominates the magnetic properties. The uniaxial anisotropy provides and energy barrier of $K_u V$ between the two energy minima; it is the size of this energy barrier that provides the stability of the magnetic orientation against temperature.

Callen and Callen[43] derived the temperature dependence of the anisotropy values; for an anisotropy of order $l$ it is related to the temperature dependence of the magnetisation via

$$\frac{K_l(T)}{K_l(0)} = \left(\frac{M(T)}{M(0)}\right)^{l(l+1)/2} \tag{2.25}$$

For uniaxial anisotropy this means that it will follow $M(T)^3$ while cubic anisotropy will follow $M(T)^{10}$, implying that the anisotropy will reduce at a faster rate than the magnetisation which is important for HAMR. An example of this behaviour is shown in figure 2.2; the magnetisation can be approximated by the critical function $M(T)/M(0) = (1 - T/T_C)^\beta$ where $\beta$ is the critical exponent, for this example the mean field value of the exponent is used $\beta = 1/2$. This mean field exponent arises from the Landau model of the free energy, where considering the symmetry of the magnetisation it is formed from an expansion using only even powers of the magnetisation. When considering the convexity of the free energy close to the critical point the coefficients of this expansion have a temperature dependence proportional to $(1 - T/T_C)$, and so from $M = \partial\mathcal{F}/\partial H$ the earlier expression can be found[44].

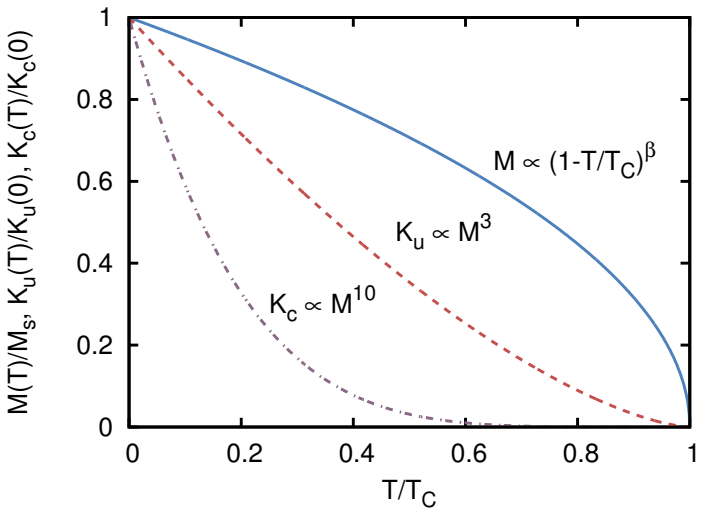


Figure 2.2.: An example of the Callen-Callen theory for the anisotropy temperature dependence. The uniaxial anisotropy scales as $K_u \propto m^3$ while the cubic anisotropy scales as $K_c \propto m^{10}$. The magnetisation is shown as $M(T) = (1 - T/T_C)^\beta$ where $\beta = 1/2$ is the mean field critical exponent.

Since $\beta < 1$, the anisotropy will generally decrease with temperature at a much faster rate than the magnetisation. For the HAMR process this implies that the anisotropy can be reduced significantly faster than the magnetisation which aids the switching process.

### 2.2.3 *Zeeman And Dipolar Interactions*

The third Hamiltonian term is the Zeeman energy; which is the interaction of the spins with an external applied magnetic field.

$$\mathcal{H}_{\text{Zeeman}} = -\mu_s \sum_i \mathbf{S}_i \cdot \mathbf{H}_{\text{app}} \tag{2.26}$$

This term forms the splitting of the up and down spins in an external field. Classically this shows the energy minimum when the spins, and hence the magnetisation, are aligned with the field. In most cases the field is uniform over the system and so we can see that the energy depends on the magnetisation; therefore at high temperatures when the magnetisation is sufficiently reduced it will not couple strongly to the field. This can be an issue for HAMR since the field is applied when the system is demagnetised; the effect of the field will be to bias the system as it cools

thus aligning with the field. In this case there is still a large probability of the grain switching over the energy barrier which can lead to a low remanent magnetisation.

The final term in equation 2.5 is the magnetic dipole-dipole interaction term. This is the long range coupling of two spins via the magneto-static field that are at positions $\mathbf{r}_i$ and $\mathbf{r}_j$ respectively. The interaction term is given by

$$\mathcal{H}_{\text{dipole}} = -\frac{\mu_0 \mu_s^2}{4\pi} \sum_{i,j} \frac{3(\mathbf{S}_i \cdot \hat{\mathbf{r}}_{ij})(\mathbf{S}_j \cdot \hat{\mathbf{r}}_{ij}) - \mathbf{S}_i \cdot \mathbf{S}_j}{r_{ij}^3} \tag{2.27}$$

where $r_{ij} = |\mathbf{r}_{ij}|$ and $\hat{\mathbf{r}}_{ij} = \mathbf{r}_{ij}/r_{ij}$ are the magnitude and unit vector of the separation vector $\mathbf{r}_{ij} = \mathbf{r}_j - \mathbf{r}_i$ and $\mu_0$ is the vacuum permeability. This interaction is valid when the separation between dipoles is much greater than their dipole length; in this case this is true as the magnetic moments are assumed to be point-like and small on the scale of the whole system. This term governs the long range interaction of the spins and can be important over large length scales. However on the length scale considered in the atomistic spin model the magnitude of the interaction is small compared to the ordering created by the exchange interaction. Blundell[34] estimates that the dipole interaction at a separation of r=1Å would correspond to a temperature of 1K. In the HAMR process the temperature is much higher than this and since a large anisotropy is considered this interaction plays very little role in the following simulations and is therefore neglected as it is computationally expensive to include.

## 2.3 MODEL HAMILTONIAN FOR L1$_0$ FEPT

For high density magnetic recording devices iron platinum is of great importance, since in the L1$_0$ phase it has been measured to have large uniaxial anisotropy. In the L1$_0$ phase FePt forms into a face centred tetragonal structure with alternating layers of Fe and Pt forming along [001] axis, which is the anisotropy easy axis. The unit cell is shown in figure 2.3. Since it is a tetragonal cell the [001] axis is smaller than the [100] and [010] axes, this gives a unit cell size $a = 3.86\,\text{Å}$ with $c/a = 0.969$. Whilst there will be significant motion of the atoms within the crystal lattice structure due to thermal effects to simplify the model these are not taken into account. In this case the atoms are fixed at their equilibrium positions.

A Hamiltonian was developed through *ab-initio* calculations performed by Mryasov *et al.*[20] Iron platinum is a more complex material to model as the two species behave in different ways. Fe is a typical ferromagnet and has magnetic moments that

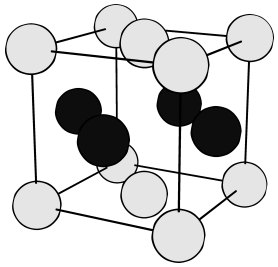

Figure 2.3.: Unit cell for L1$_0$ FePt, white atoms are Fe, dark grey are Pt.

are, to a reasonable degree, constant. It however has a low anisotropy. Pt has a strong spin-orbit coupling but is a non-magnetic material. The alloying of these two elements leads to a high anisotropy material and makes FePt a strong candidate for high density magnetic recording. The origin of this large anisotropy is described in the following.

The *ab-initio* calculations by Mryasov *et al.* used the constrained local spin density approximation (CLSDA) to force a non-collinear arrangement of the Fe and Pt moments. Using this approach it was found that the Fe moments vary little with the onsite field but the Pt moments vary linearly with it. This means when the Fe moments are in a ferromagnetic configuration a small moment is polarised on the Pt atoms and when there is anti-alignment there is no moment, as shown in figure 2.4. Essentially, the Pt spin moment is found to be linearly dependent on the exchange field from the neighbouring Fe moments. This dependence allows the Pt moments to be expressed in terms of a linear susceptibility and so the part of the total Hamiltonian which depends on the Pt moments can be re-written in terms the Fe moments, giving a resultant Hamiltonian including only the Fe degrees of freedom. The new Hamiltonian only includes the Fe spins and incorporates mediated parameters:

$$\mathcal{H} = -\sum_{i,j} \tilde{J}_{ij}\mathbf{S}_i \cdot \mathbf{S}_j - \sum_i d_i^{(0)}\mathbf{S}_{iz}^2 - \sum_{i,j} d_i^{(1)}\mathbf{S}_{iz} \cdot \mathbf{S}_{jz} - \sum_i \mu_i \mathbf{S}_i \cdot \mathbf{B} \tag{2.28}$$

The mediated isotropic exchange ($\tilde{J}_{ij}$), onsite anisotropy ($d_i^{(0)}$) and two-ion anisotropy ($d_{ij}^{(1)}$) parameters are given by the combination of the existing Fe-Fe ($J_{ij}$), Fe-Pt exchange ($J_{i\nu}$), and onsite Fe and Pt terms ($k_{\mathrm{Fe}}^{(0)}, k_{\mathrm{Pt}}^{(0)}$) given by:

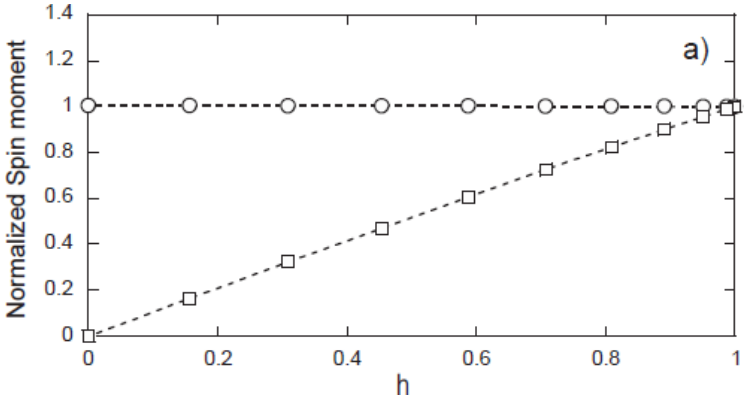


Figure 2.4.: The dependence of the magnetic moment of the Fe (circles) and Pt (squares) atoms on the normalised exchange field, h. The Fe moment is constant where as the Pt moment varies in a linear fashion. This allows the Pt degrees of freedom to be replaced with only the Fe ones. Figure taken from Mryasov *et al.*[20]

$$\tilde{J}_{ij} = J_{ij} + \tilde{I}\left(\frac{\chi_\nu}{M_\nu^0}\right)^2 \sum_\nu J_{i\nu}J_{j\nu} \tag{2.29}$$

$$d_i^{(0)} = k_{\mathrm{Fe}}^{(0)} + k_{\mathrm{Pt}}^{(0)}\left(\frac{\chi_\nu}{M_\nu^0}\right)^2 \sum_\nu J_{i\nu}^2 \tag{2.30}$$

$$d_{ij}^{(1)} = k_{\mathrm{Pt}}^{(0)}\left(\frac{\chi_\nu}{M_\nu^0}\right)^2 \sum_\nu J_{i\nu}J_{j\nu} \tag{2.31}$$

where the parameters $\tilde{I}, \chi_\nu, M_\nu^0$ are the intra-atomic exchange interaction, the Pt local susceptibility and the magnitude of the polarised Pt magnetic moment respectively. The two-ion anisotropy represents an anisotropy of the exchange interaction and is much larger than the onsite uni-axial anisotropy. As Mryasov *et al.* describes the ratio of the the two-ion anisotropy to the onsite anisotropy is what gives the macroscopic anisotropy constant scale with $m^{2.1}$ in FePt as the two-ion term is found to scale as $m^2$. Since the two-ion anisotropy is part of the exchange interaction it also has a long range, implying that surfaces will have a much larger effect on the anisotropy than in other materials.

## 2.4 SIMULATION METHODS

To model the dynamic and static properties of the system described by the Hamiltonian given in the previous section two different simulation methods are employed:

Atomistic Spin Dynamics (ASD) and Monte-Carlo (MC) integration. ASD is a finite difference method of numerically solving the equation of motion for the spins. MC integration is an equilibrium method of sampling the phase space through importance sampling. In the following we give a description of each method. While the MC method is a useful and efficient method for determining static properties, ASD is required for the dynamic calculations to be presented.

### 2.4.1 *Atomistic Spin Dynamics*

One of the corner stones of modelling magnetisation dynamics is the Landau-Lifshitz (LL) equation which describes the motion of a magnetic moment in a field. Many approaches to model the dynamic evolution of the magnetisation utilise this equation or one of its variants. Landau and Lifshitz[45] write the equation of motion for the magnetisation as

$$\frac{\partial \mathbf{M}}{\partial t} = -\gamma \mathbf{M} \times \mathbf{H} - \frac{\lambda}{M^2} \mathbf{M} \times \mathbf{M} \times \mathbf{H} \tag{2.32}$$

where $M = |\mathbf{M}|$ is the magnitude of the magnetisation and $\mathbf{H} = -\partial \mathcal{F} / \partial \mathbf{M}$ is the effective field acting on the magnetisation, with $\mathcal{F}$ as the free energy. This approach is derived in a phenomenological manner and, importantly, that effective field can be calculated from the thermodynamic potential at constant temperature[46]. In this case it is the Helmholtz free energy and in this manner can contain contributions, for example, from the demagnetisation field, anisotropy as well as an external field. In their derivation, Landau and Lifshitz included a phenomenological damping term, controlled by the parameter $\lambda$, that is constructed such that the magnetisation will move to point along the direction of the field.

The first term in the LL equation is the precession of the magnetisation around an applied field and the second term gives the damping towards the field to dissipate energy from the magnetisation. The precession term can be derived in a few different ways; the most illuminating comes from the quantum mechanical approach. Using Ehrenfest's theorem, the equation of motion for the expectation of the spin vector is given by

$$i\hbar \frac{\partial \langle \mathbf{S} \rangle}{\partial t} = \langle [\mathbf{S}, \mathcal{H}] \rangle \tag{2.33}$$

where the $[A, B] = AB - BA$ is the commutator relation for $A$ and $B$. In this equation $i$ is used for the imaginary number. For a spin in a magnetic field the spin Hamiltonian would be the Zeeman energy such that $\mathcal{H} = -g_e \mu_B \mathbf{S} \cdot \mathbf{B}$. Using this

and the spin commutation relation, $[S_a, S_b] = i\hbar\varepsilon_{abc}S_c$ where $\varepsilon_{abc}$ is the Levi-Cevita tensor ( 1 if $a, b, c$ are cyclic or -1 if anti-cyclic), it is found that

$$\frac{\partial\langle\mathbf{S}\rangle}{\partial t} = -\gamma\langle\mathbf{S}\rangle \times \mathbf{B} \tag{2.34}$$

where the gyromagnetic ratio of the electron, $\gamma = \mu_B g/\hbar = 1.760\,859\,708\,\mathrm{rads}^{-1}\mathrm{T}^{-1}$, has been used as the pre-factor. Now moving to a classical description where the magnetisation is $\mathbf{M} = \sum_n \langle\mathbf{S}_n\rangle$ the original precession term in the LL equation is recovered.

The damping term in the LL equation is included as a phenomenological term to account for relativistic effects dissipating energy and angular momentum for the spin system. This term however is not suitable in the high damping limit[47] and so a more general damping term is derived by Gilbert[48]. Gilbert's form of the damping is derived in a Lagrangian form, where the dissipative effects are incorporated through the Rayleigh dissipation functional

$$\mathcal{R} = \frac{\eta}{2}\int \frac{\partial\mathbf{M}(\mathbf{r}, r)}{\partial t} \cdot \frac{\partial\mathbf{M}(\mathbf{r}, r)}{\partial t} d\mathbf{r} \tag{2.35}$$

The scalar constant $\eta$ controls the energy dissipation and could in general be non-uniform but since the matrix damping function $\eta_{ij}(\mathbf{r}, \mathbf{r}')$ is not well known. From this functional the equation of motion can be found, which is given as:

$$\frac{\partial\mathbf{M}}{\partial t} = -\gamma\mathbf{M} \times \left[\mathbf{H} + \eta\frac{\partial\mathbf{M}}{\partial t}\right] \tag{2.36}$$

This equation is usually known as Gilbert's equation; the derivative on the left hand side of the equation can be problematic so it can be useful to reform the equation. In this case it is known as the Landau-Lifshitz-Gilbert (LLG) equation as the damping takes the form as in the LL equation but derived from Gilbert's equation. This can be written for the atomistic spins by using $\mathbf{M} = \mu_s\mathbf{S}$ so that for each spin in the material it has the equation of motion:

$$\frac{\partial\mathbf{S}_i}{\partial t} = -\frac{\gamma}{(1+\lambda^2)\mu_s}\mathbf{S}_i \times (\mathbf{H}_i + \lambda\mathbf{S}_i \times \mathbf{H}_i) \tag{2.37}$$

with the effective field given by $\mathbf{H}_i = -\partial\mathcal{H}/\partial\mathbf{S}_i$. The motion described by the LLG is shown in figure 2.5 for each spin component. The damping is controlled by the parameter, $\lambda$, this represents the coupling of spins to an underlying heat bath to which energy can be transferred to and out of the spin system. The Gilbert damping

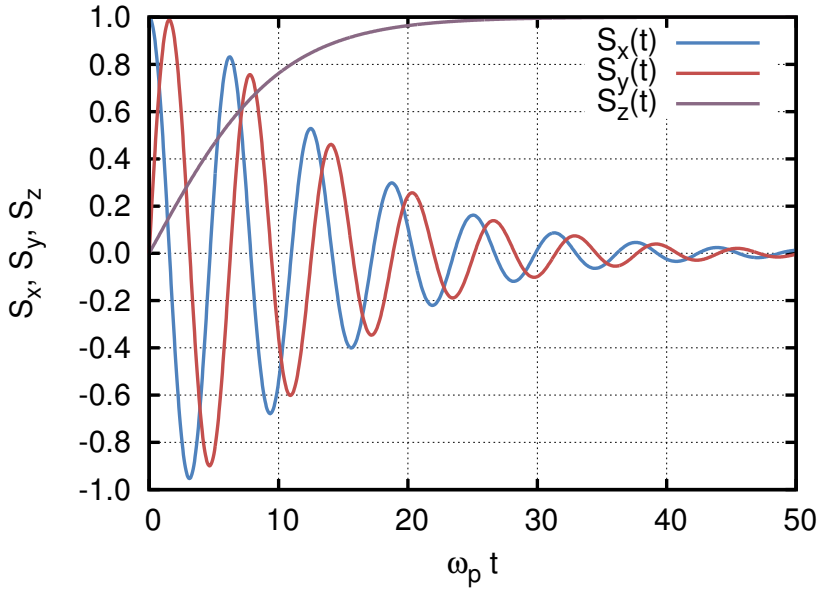


Figure 2.5.: The damped precession of the LLG equation with $\lambda = 0.1$ in an external field of 100T, shown in terms of the precession frequency $\omega_p = \gamma h/\mu_s$.

is measured on a macroscopic scale through experiments such as FMR[49] but this is a different quantity to the damping on the atomistic scale. The atomistic damping is not equal to the Gilbert damping due to spin wave scattering in a ensemble of spins but at 0K they do coincide. To mark this difference the atomistic damping is usually termed the coupling as described later it provides the strength of the coupling of the spins to the underlying thermal bath. For FePt the Gilbert damping has been measured as $\alpha = 0.1$ from various techniques[50, 51] and therefore this value is used for the coupling in the later chapters.

From the LLG equation one can easily pick out the relevant time scales. With no damping the spins will precess about the field with a frequency given by $\omega_p = \gamma h/\mu_s$. For an applied field, $h = \mu_s h_{\text{app}}$, the precession frequency is independent of the magnetic moment and for $h_{\text{app}} = 1\,\text{T}$, $\tau = 2\pi/\omega_p = 36\,\text{ps}$. For the exchange field $h = zJ$ the precession frequency is much higher; for example using the parameters for bcc Fe; $\tau = 13\,\text{fs}$. Therefore in the atomistic model the Nyquist frequency is $\approx 10\,\text{fs}$.

The effective field present in the LLG equation arises from the deterministic internal and external fields which are accounted for by the Hamiltonian. For the system to stay in thermal equilibrium a stochastic fluctuating field is also incorporated into

the effective field. This thermal process couples the spin system to a heat bath for the transfer of energy and angular momentum.

$$\mathbf{H}_i = -\frac{\partial \mathcal{H}}{\partial \mathbf{S}_i} + \boldsymbol{\xi}_i \xi \tag{2.38}$$

The inclusion of this fluctuating thermal term sets the LLG equation as a Langevin equation[52], hence this method is usually described as Langevin Dynamics (LD). From the Brownian approach the fluctuating field is assumed to arise from underlying processes that interact with the spin. The exact origin of these processes is not required but are assumed to lie within the 'white' noise limit. In this limit the time correlation of the noise is assumed to be much smaller than that of the spin motion[52] which allows the thermal noise term to be described by a Gaussian random number. The time evolution of the probability density function is described by the Fokker-Planck equation; by converting the stochastic LLG equation into this form[53] the moments of Gaussian process found to be

$$\langle \xi_{i\alpha}(t) \rangle = 0 \tag{2.39}$$

$$\langle \xi_{i\alpha}(t) \xi_{j\beta}(s) \rangle = \frac{2\mu_s \lambda k_B T}{\gamma} \delta_{ij} \delta_{\alpha\beta} \delta(t-s) \tag{2.40}$$

where $i, j$ refer to spin indices, $\alpha, \beta$ refers to the vector components and $t, s$ refer to time. The second moment describes the magnitude of the fluctuations, which as equation 2.40 shows is related to both the temperature and the atomistic damping parameter. Since the atomistic damping is distinct from the macroscopic Gilbert damping it is sometimes referred to as the coupling term as it represents not only the dissipation of energy and angular momentum from the spin system but the coupling to the thermal bath.

By incorporating thermal noise into the equations of motion the time evolution of the spin system are found through numerical integration of the stochastic LLG (sLLG). This is done by discretising the time domain into steps so that $t = n\Delta t$ and the spin ensemble is updated at each time step using an integration scheme. Kloeden and Platen[54] present a detailed discussion of the integration of stochastic differential equations, including a description of the Heun scheme which is commonly used for spin dynamics[5]. Recently more advanced integration schemes have been presented and so here an alternative method based on the Semi-Implicit scheme[55] is given. First the Heun scheme shall be described to give a comparison of the method.

To begin with the sLLG will be written in terms of a deterministic drift term $\mathbf{f}$ and a multiplicative diffusion tensor $\underline{\mathbf{g}}$, which can be easily determined from equation 2.37. In stochastic calculus the integral of the noise term can be performed in two different manners; these two branches are known as Ito and Stratonovich calculus. Whilst they both can be converted readily, Stratonovich calculus is used here as it is more physically meaningful.[54] In terms of Stratonovich calculus (denoted by the $\circ$ in the following) the differential equation is:

$$d\mathbf{S} = \mathbf{f}(\mathbf{S}, t)dt + \underline{\mathbf{g}}(\mathbf{S}, t) \circ d\mathbf{W} \tag{2.41}$$

Here, $\mathbf{W}$ is a vector Weiner process that arises from the stochastic integral of the noise term. $\mathbf{f}$ and $\mathbf{g}$ are the deterministic drift and multiplicative diffusion functions which are determined from the sLLG equation. With this definition the Heun scheme is given by:

$$\tilde{\mathbf{S}}_{n+1} = \mathbf{S}_n + \mathbf{f}(\mathbf{S}_n, t)\Delta t + \underline{\mathbf{g}}(\mathbf{S}_n, t)\Delta\mathbf{W}_n \tag{2.42}$$

$$\begin{aligned}\mathbf{S}_{n+1} = \mathbf{S}_n &+ \left(\mathbf{f}(\mathbf{S}_n, t) + \mathbf{f}(\mathbf{S}_{n+1}, t + \Delta t)\right)\frac{\Delta t}{2} \\ &+ \left(\underline{\mathbf{g}}(\mathbf{S}_n, t) + \underline{\mathbf{g}}(\tilde{\mathbf{S}}_{n+1}, t + \Delta t)\right)\frac{\Delta\mathbf{W}_n}{2}\end{aligned} \tag{2.43}$$

Where $\mathbf{S}_n$ indicates the spin vector at time step $n$, $\Delta t$ is the size of the time step taken and $\Delta\mathbf{W}_n$ is the discrete differential of the Wiener process which takes the form of a Gaussian random number with a variance of $\sqrt{\Delta t}$. The magnitude of the thermal noise is taken within the diffusion tensor $\underline{\mathbf{g}}$.

The first step is a predictor step that uses a simple Euler method to give an estimate of the variable at the next time point. Whilst this simple update does not give an accurate result it allows an estimation of the gradient at the new time point. The combination of the gradient at the old time step and the estimate at the new time step allows the corrector step to be more accurate. The Heun method has been shown to converge with order 2[54].

The Heun scheme however does not conserve the length of the vector which for the case of the classical atomistic spins is incorrect as the magnitude must remain constant. Therefore for each new position (both predictor and corrector steps) the vector must be renormalised. This change in the magnitude is due to the nature of the scheme, the Heun scheme provides a translation of the variable but for the LLG equation there is only transverse terms and as such only rotation is required. The Semi-Implicit scheme as presented by Mentink *et al.*[55] has been shown to conserve

the spin length and so it is employed here. To describe the Semi-Implicit scheme the sLLG is re-written taken the cross product of the spins outside of the drift and diffusion terms in equation 2.41 so that now two new 'cross product' drift, **a**, and diffusion, **b**, terms are used:

$$d\mathbf{S} = \mathbf{a}\left(\mathbf{S}, t\right) \times \mathbf{S}dt + \mathbf{b}\left(\mathbf{S}, t\right) \times \mathbf{S} \circ d\mathbf{W} \tag{2.44}$$

Now the Semi-Implicit scheme given by Mentink *et al.* is written as:

$$\mathbf{S}'_{n+1} = \mathbf{S}_n + \mathbf{a}(\mathbf{S}_n, t) \times \left(\frac{\mathbf{S}_n + \mathbf{S}'_{n+1}}{2}\right)\Delta t \tag{2.45}$$

$$+ \mathbf{b}\left(\mathbf{S}_n, t\right) \times \left(\frac{\mathbf{S}_n + \mathbf{S}'_{n+1}}{2}\right)\Delta \mathbf{W}_n \tag{2.46}$$

$$\mathbf{S}_{n+1} = \mathbf{S}_n + \mathbf{a}\left(\left(\frac{\mathbf{S}_n + \mathbf{S}'_{n+1}}{2}\right), t\right) \times \left(\frac{\mathbf{S}_n + \mathbf{S}'_{n+1}}{2}\right)\Delta t \tag{2.47}$$

$$+ \mathbf{b}\left(\left(\frac{\mathbf{S}_n + \mathbf{S}'_{n+1}}{2}\right), t\right) \times \left(\frac{\mathbf{S}_n + \mathbf{S}'_{n+1}}{2}\right)\Delta \mathbf{W}_n \tag{2.48}$$

This is an extension of the Implicit Midpoint method presented by D'Aquino *et al.*[56, 57], where the fields are calculated at the midpoint between the current and next time step. In this form a predictor step is used to calculate the fields at the midpoint for the corrector step and each step itself is implicit. So far these equations have been written for a single spin but the extension to the entire spin ensemble is straightforward. In the Implicit Midpoint method, to invert the equations would require solving a 3N by 3N matrix but in this method the update for each spin is independent and so the 3 by 3 matrix can be inverted analytically. By doing this it is found that the Semi-Implicit scheme is described by a Cayley transform[58]. Since the Cayley transform is derived for a deterministic differential equation the drift and diffusion terms are combined into a single vector:

$$\mathbf{A}\left(\mathbf{S}, t\right) = \mathbf{a}\left(\mathbf{S}, t\right) + \mathbf{b}\left(\mathbf{S}, t\right)\Delta \mathbf{W} \tag{2.49}$$

This is termed the 'generator' and should ideally be a constant but since the LLG equation contains the damping term it will depend on **S**. In this case the equation is being treated deterministically and the stochastic field term is taken into the

effective field. The generalised solution to equations of these forms are the Cayley transform[58]:

$$\mathrm{Cay}(\mathbf{A})\mathbf{S} = \mathbf{S} + \frac{\mathbf{A}\times\mathbf{S} + \frac{1}{2}\mathbf{A}\times\mathbf{A}\times\mathbf{S}}{1+\frac{1}{4}|A|^2} \tag{2.50}$$

The benefit of this is that the Cayley transform is a rotational update of the spin vector rather than a translational one. The Semi-Implicit scheme can now be written as:

$$\boldsymbol{S}'_{n+1} = \mathrm{Cay}(\mathbf{A}\left(\mathbf{S}_n, t\right))\,\mathbf{S}_n \tag{2.51}$$

$$\boldsymbol{S}_{n+1} = \mathrm{Cay}\left(\mathbf{A}\left(\frac{\mathbf{S}_n + \mathbf{S}'_{n+1}}{2}, t\right)\right)\mathbf{S}_n \tag{2.52}$$

Now the Semi-Implicit scheme is written explicitly and the spin conservation is naturally included in the model. The testing and comparison of the Semi-Implicit and Heun schemes will follow in the next section after a discussion of the Monte-Carlo methods used.

### 2.4.2 *Monte-Carlo and Constrained Monte-Carlo*

Efficient calculation of thermodynamic properties can be made using Monte-Carlo integration techniques. Langevin dynamics is ergodic as the thermal noise will force the system to explore the full phase space but the timescale for rare events to occur can be unreasonable for simulation purposes. Therefore when only the equilibrium properties are required it can be computationally faster to utilise Monte-Carlo techniques. Binder *et al.*[28] provide an extensive investigation of the properties of spin systems using Metropolis Monte-Carlo.

Metropolis Monte-Carlo (MMC) is a example of an importance sampling method; a configuration of the system is generated and excepted through some criteria and the properties of the accepted configuration are used to compute the ensemble average. The series of configurations that are generated are known as a Markov chain, as they have the property that the new configuration only depends on the current configuration and not any previous configurations. The steps taken to alter the configuration are important; they must allow for ergodicity but must also efficiently explore phase space. To this end a combination of three different trial steps are used[5, 59]; a spin flip, uniform sphere and a small angle change. The Markov chain

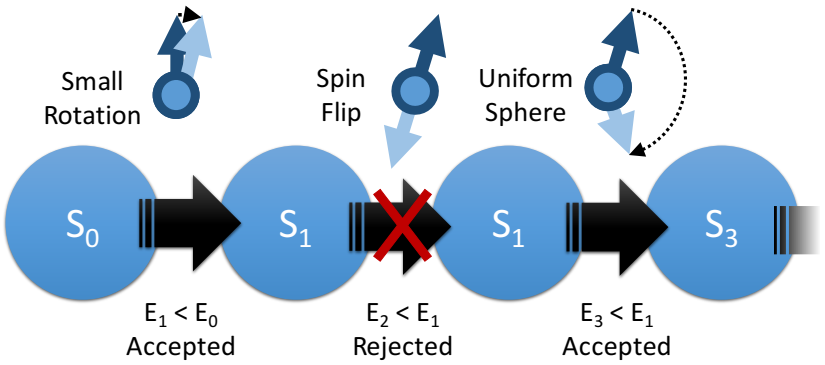


Figure 2.6.: Illustration of the Metropolis Monte-Carlo method with three trial steps. The series of states $S_n$ make a Markov chain where the new state only depends on the current state. In this example the energy of the spin flip state was too high and rejected while the others are excepted.

and the trial steps are illustrated in figure 2.6; mathematically these trial steps are given by:

$$\mathbf{S}_i' = \begin{cases} -\mathbf{S}_i & \text{spin flip} \\ \dfrac{(u,v,w)}{(u^2+v^2+w^2)^{1/2}} & \text{uniform sphere} \\ \dfrac{\mathbf{S}_i+\boldsymbol{\delta}}{|\mathbf{S}_i+\boldsymbol{\delta}|} & \text{small step} \end{cases} \tag{2.53}$$

The first of these step types is the spin flip step in a similar manner to a trial move in the Ising model. This step by itself would not satisfy ergodicity since the system would not be able to access the full phase space available.

The second step is selection of the new spin direction uniformly over the unit sphere. $u, v, w$ are all Gaussian random numbers and the spin vector is normalised which provides uniform sampling without any clustering at the poles. This move allows efficient moves through phase space but in situations such as low temperature when the magnetisation does not vary significantly moves of this type usual have a low probability.

The third step type is a small deviation from the current spin position; where $\boldsymbol{\delta} = \mathbf{S}_i \times (u, v, w)$, again $u, v, w$ are Gaussian random numbers but improved acceptance is taken when the standard deviation of the random numbers is related to the temperature $\sigma^2 \propto \sqrt{T}$[41]. These small steps have a higher probability compared to the uniform steps as the deviations are around the energy minimum of the system

but it will take more of these steps to move through phase space. Ideally the acceptance rate of the MC algorithm should be 50% and so the variance of the steps can be tuned to reach this desired rate.

Following the generation of a trial configuration the MMC method accepts the new configuration into the Markov chain with the probability:

$$\mathcal{P} = \min\left[1, \exp\left(-\frac{\Delta\mathcal{H}}{k_B T}\right)\right] \tag{2.54}$$

If the MMC rejects the new configuration then the current configuration is kept and used to calculate the averages. Since the probability is based on the Boltzmann distribution, the system will move towards the low energy configurations but even with the trail moves above it can easily become stuck in local minima.

To evaluate properties along a specific direction the Constrained MC is used, developed by Asselin *et al.*[41] In this the proposed state is constructed from altering two spins. The first spin, termed the primary spin, follows the same moves as for the Metropolis MC and then a second, compensation spin, is chosen for which the magnetisation direction is left unaltered but with the length allowed to change. The acceptance criterion has to be modified by the change in the geometric Jacobians to preserve ergodicity. The full algorithm is given here for completeness but the derivation of the Jacobian pre-factor in the acceptance probability is given by Asselin *et al.*:

1. A trial spin is randomly selected (primary spin)
2. A new orientation of the spin is calculated according to equation 2.53
3. A second spin is randomly selected (compensation spin)
4. The compensation spin is moved to mirror the transverse motion of the primary spin thus giving no net change in the transverse magnetisation
5. If the compensation spin cannot conserve the magnetisation direction then the step is rejected
6. If the magnetisation switches orientation ($m_z \leftrightarrow -m_z$) then the step is rejected
7. The energy of the new state containing both the moves is calculated
8. The new state is accepted with probability given by:

$$\mathcal{P} = \min\left[1, \left(\frac{M_z'}{M_z}\right)^2 \frac{|S_{jz}|}{|S_{jz}'|} \exp\left(-\frac{\Delta\mathcal{H}}{k_B T}\right)\right] \tag{2.55}$$

## 2.5 MODEL TESTS

The details of the atomistic spin model have now been presented. We proceed now to discuss the testing of the implementation of the model. The model is tested for both equilibrium and dynamic properties which test both the integration scheme and the thermal distribution.

### 2.5.1 *Precession Frequency*

Upon implementation of the semi-implicit scheme it has become evident that the scheme has some dynamic instabilities. In Mentink *et al.*[55] test the scheme for the equilibrium properties and the stability is assumed to be up to 4 steps per precession in this case. However the dynamical properties are only briefly mentioned when the motion of two coupled spins is considered. In this case Mentink *et al.* show that all the schemes introduce error into the precession frequency but this is assumed to be due to the chosen time step being large and the behaviour of this error with time step is not followed.

As the stability of the precession frequency was investigated another version of the semi-implicit scheme was implemented. Lewis *et al.*[58] discuss how a parameter, given the symbol sigma, can affect the stability of the schemes. This parameter controls the addition of a parallel term into the generator which in an exact case should have no effect on the dynamics as it is cancelled out in the cross products. This is investigated also in Bottauscio *et al.*[60] which shows that for certain values of sigma the required time step for stability can increase by orders of magnitude. By inspection of Mentink's semi-implicit scheme we can see that there is an error introduced in the predictor step. The basis of the scheme is the implicit midpoint scheme and its full form gives a cross product at the half timestep $(n + 1/2)$ such that $\mathbf{S}_{n+1/2} \times \mathbf{A}(\mathbf{S}_{n+1/2})$ and in this case any term in $\mathbf{A}$ that is parallel to $\mathbf{S}_{n+1/2}$ will cancel. However in the semi-implicit scheme the midpoint is now predicted to reduce the requirement that the forward time step is known and as such the term is now $\mathbf{S}_{n+1/2} \times \mathbf{A}(\mathbf{S}_n)$. Now any parallel term is along $\mathbf{S}_n$ not $\mathbf{S}_{n+1/2}$ and will not cancel. For the atomistic model with an exchange interaction between the spins, if

they are mostly aligned this will create a component along $\mathbf{S}_n$ which can be of the order of 1000T. Such a strong field as this can easily induce an error in the precession frequency even if the difference between the time steps is very small. Inspired by this it was chosen that the orthogonal generator from Ref.58 would counteract this error. The form of this is:

$$\mathbf{A}_O(\mathbf{S},t) = \mathbf{A}(\mathbf{S},t) - (\mathbf{S}\cdot\mathbf{A}(\mathbf{S},t))\,\mathbf{S} \tag{2.56}$$

This orthogonal generator simply subtracts the parallel component from the calculated generator. If this is substituted into the LLG equation then it is still exact as it only contains transverse terms. However it importantly corrects the discretised case, which as discussed above will incorrectly involve parallel terms into the dynamics.

This variation of the semi-implicit scheme was tested alongside the normal semi-implicit and the Heun schemes. The most important test was that of the precession frequency. If thermal effects are not included the dynamics of a system of spins is analytically solvable giving equations that the simulation results can be compared to. The analytic solutions are given by:

$$M_x(t) = M_s\cos(\omega_p t)\cosh^{-1}(\omega_d t) \tag{2.57}$$

$$M_y(t) = M_s\sin(\omega_p t)\cosh^{-1}(\omega_d t) \tag{2.58}$$

$$M_z(t) = M_s\tanh(\omega_d t) \tag{2.59}$$

This solution gives motion that precesses about and damps towards the applied field at rates given by $\omega_p = \frac{\gamma h}{1+\alpha^2}$ and $\omega_d = \omega_p\alpha$. The precession frequency $\omega_p$ is defined by the input parameters and should be a constant when no thermal effects are considered when the coupling factor is coincident with the Gilbert damping, i.e $\alpha = \lambda$.

Since we are only considering a uniform system these parameters are all constant for different spins and as such all the spins precess at the same frequency. If the spins are aligned initially they will stay aligned and there will be no excitation of the exchange mode even when it is included. It will give a large field term parallel to $\mathbf{S}_n$ that as discussed is crucial to the stability of the semi-implicit scheme. A Fourier transform of the simulation data was used to calculate the precession frequency and

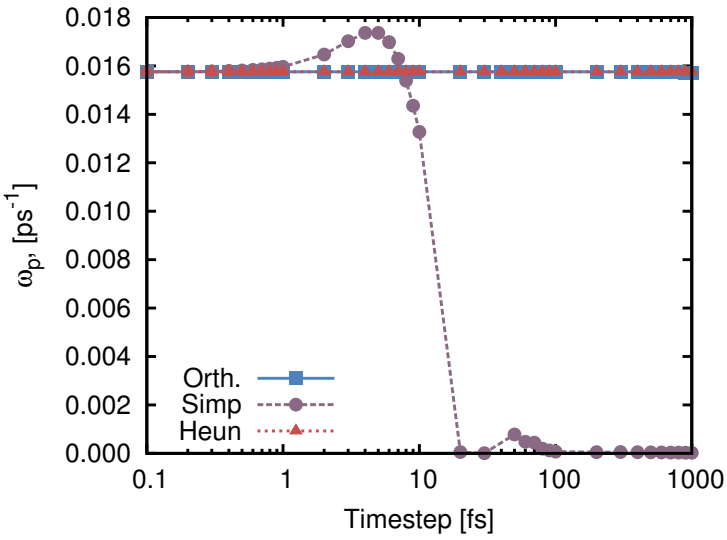


Figure 2.7.: The stability of the three schemes for the precession frequency with no thermal effects. The spins are initially all fully aligned along the x-axis with a constant applied field in the z direction to create the precessional motion. The precession frequency is calculated from the Fourier transform of the system with the minimum frequency being 0.01 GHz.

damping for different time steps to which the analytic equation can be fitted to. For the x component of the magnetisation the Fourier transform is:

$$\mathbb{F}\left(M_x\right)(\omega) = \frac{\pi}{2\alpha\omega_p}\left[\operatorname{sech}\left(\frac{\pi^2}{\alpha\omega_p}\left(\omega - \frac{\omega_p}{2\pi}\right)\right) + \operatorname{sech}\left(\frac{\pi^2}{\alpha\omega_p}\left(\omega + \frac{\omega_p}{2\pi}\right)\right)\right] \tag{2.60}$$

Figure 2.7 shows the precession frequencies calculated from a fit of the analytic Fourier transform to the FFT of the simulated data for different time steps. We are comparing the two variants of the semi-implicit scheme to the commonly used Heun scheme. The figure shows that the normal semi-implicit scheme becomes unstable at very short time steps; for this given system the Nyquist frequency is the precession frequency and so we would expect schemes to be stable for time steps of the order of 10000 fs. The orthogonal variant and the Heun scheme show good stability within this region as expected.

Figure 2.8 shows the damping parameter calculated from the same fitting to the FFT. Again the Heun and orthogonal semi-implicit scheme show good stability within this regime whilst the normal semi-implicit scheme shows a deviation from the input coupling factor at time steps even as low as 1 fs. Above a timestep of 1 fs the damping in the semi-implicit scheme is over-damped and quickly breaks down

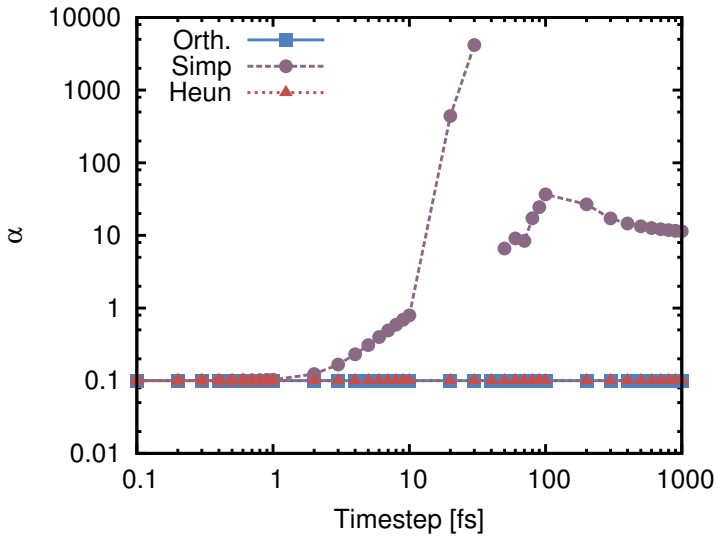


Figure 2.8.: The damping calculated from the FFT data of the precession at 0K. The orthogonal semi-implicit scheme and the Heun scheme both have the correct damping for the range of timesteps shown whilst the normal semi-implicit scheme does not. The semi-implicit scheme has started to diverge from the correct damping before 1 fs.

into incorrect dynamics leading to the sharp jump in the extracted damping; in the figure this is where the line is broken as the extracted damping is off the scale of the plot. This shows that the change made to the semi-implicit scheme improves the scheme under dynamic situations. It is assumed that the orthogonal change does not alter the equilibrium stability of the scheme but further tests to investigate the scheme are important to clearly show its properties.

### 2.5.2 *Boltzmann Distribution*

We now proceed to discuss the thermal stability of the model. The inclusion of the thermal noise term in the stochastic LLG equation is designed to keep the system at a finite temperature. It is therefore important that the thermal noise keeps the system following the Boltzmann distribution. Using the Boltzmann distribution the probability, $P$, of the magnetisation having an polar angles between $(\theta,\phi)$ and $(\theta + d\theta,\phi + d\phi)$ is

$$P(\theta,\phi)\sin(\phi)d\phi d\theta \propto \exp(-\frac{\mathcal{H}(\theta,\phi)}{k_B T})\sin(\phi)d\phi d\theta \tag{2.61}$$

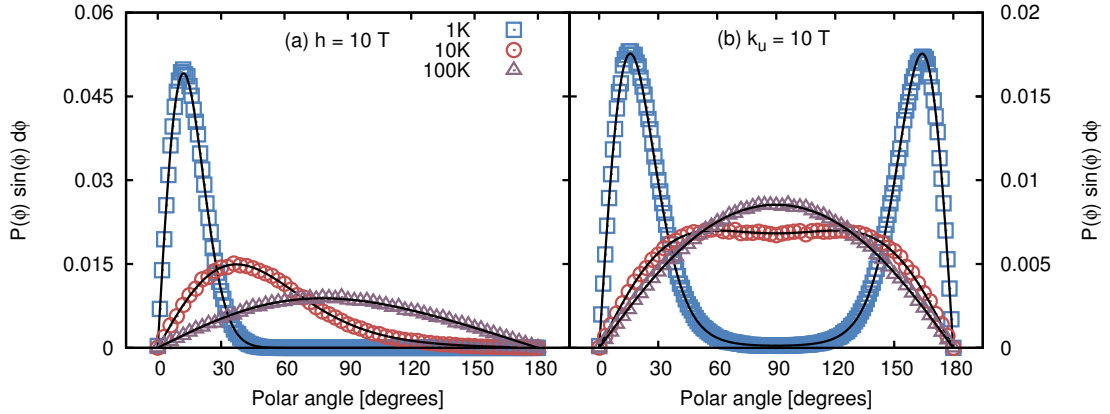


Figure 2.9.: The probability of finding the spin along a certain polar angle ($\phi$) for a paramagnet with (a) an applied field of h = 10T and (b) with an uniaxial anisotropy of 10T. The points show the probability extracted from the LD simulation using a temperature of 1K (blue squares), 10K (red circles) and 100K (purple triangles). The solid lines show the exact Boltzmann distribution given by equation 2.62.

To confirm that the model follow the Boltzmann distribution we consider the case of a simple paramagnet in an applied field with uniaxial anisotropy. Since the atoms do not interact with each other the distribution can be reduced to product of the integral over the individual atoms states. Since the Hamiltonian only depends on $\phi$ the integral over $\theta$ can be performed and the resulting constant neglected. Now the probability is given by

$$P(\phi)\sin(\phi)d\phi = \mathcal{Z}^{-1}\exp\left[\frac{1}{k_B T}(\mu_s h\cos(\phi) + k_u\cos^2(\phi))\right]\sin(\phi)d\phi \qquad (2.62)$$

where $\mathcal{Z}$ is the partition function and is used to normalise the probability. Using the Langevin dynamics technique described the paramagnet was simulated for two cases: (a) no anisotropy but an applied field of $h = 10\,\mathrm{T}$ and (b) no applied field but uniaxial anisotropy field of $k_u/\mu_s = 10\,\mathrm{T}$. The probability of finding a spin at a certain angle to the field is shown in figure 2.9 for the two cases. The points show the histogram compiled from the simulations while the solid lines show the exact Boltzmann distribution given by equation 2.62. The simulation matches the exact distribution for the both the applied field and uniaxial anisotropy for a range of temperatures confirming the correctness of the LD model.

### 2.5.3 *Equilibrium Magnetisation*

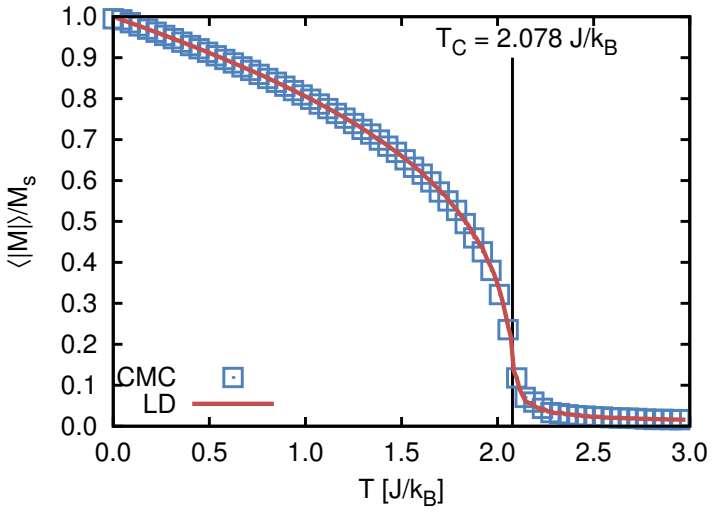


Figure 2.10.: The temperature dependence of the equilibrium magnetisation calculated from the CMC (open squares) and LD (solid line). The Curie temperature is found by fitting and is slightly higher than the expected $T_C = 2.043 J/k_B$ owing to finite size effects.

The stability at elevated temperatures is hard to quantify as there is no exact solutions to compare the results to. As a simple measure of the integration schemes and the CMC the temperature dependence of the equilibrium magnetisation is computed for a simple nearest neighbour system with a bcc crystal structure. For this simple case the Curie temperature the empirical relationship in equation 2.19 can be used to confirm that the exchange interaction and the thermal noise is correct. The averaged magnetisation length is shown in figure 2.10 for both the CMC and the LD methods for 20x20x20 bcc unit cells. The CMC is fixed in $\hat{z}$ direction with 10,000 equilibration steps and 20,000 averaging steps while the LD is equilibrated for 50 ps and averaged for a further 150 ps with a time step $dt = 1 \times 10^{-16}$ ps. Both the CMC and LD agree over the whole temperature but the Curie temperature is found to be slightly higher than the expected value of $T_C = 2.043 J/k_B$[5]. This may arise from the finite size effects but since there is good agreement between the two methods this implies they are both stable.

To further expand on the stability of different semi-implicit scheme versions on the time step the average magnetisation is calculated for variety of step sizes. In the absence of an exact analytic $M(T)$, the expected magnetisation ($M_0(T)$ for each temperature is taken to be that found using the smallest step size and averaged

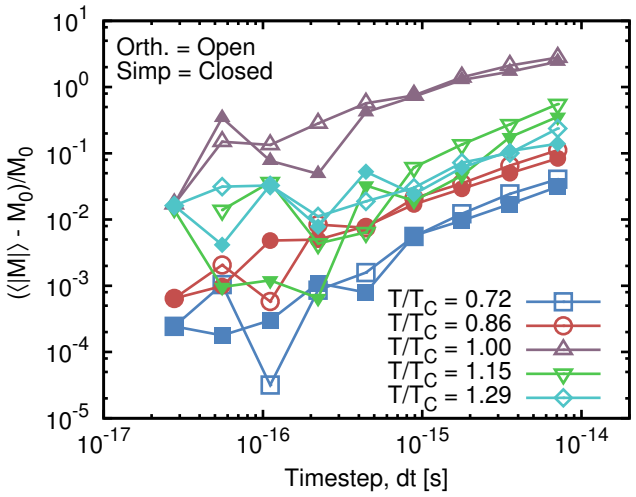


Figure 2.11.: The error between the calculated average equilibrium magnetisation and the expected magnetisation which is taken as the average of the two variants using the smallest time step. The error decreases with time step but close to the Curie temperature the error is larger.

between the different versions. The error between the calculated average and the expected magnetisation is defined as $(\langle M(T, dt)\rangle - M_0(T))/M_0(T)$. This is not exact but gives a certain measure of how the averages depend on the time step and any error in choosing $M_0(T)$ only shifts the axis. Figure 2.11 shows the scaling of the error for both the semi-implicit scheme and the orthogonal variant introduced earlier in the tests. There appears very little difference between the variants especially at small time steps and there is a significant error for time steps greater than $1 \times 10^{-16}$ s. The error at $T_C$ is large even at small time steps which is to be expected at the cusp of a phase transition. Going forward a time step of $1 \times 10^{-16}$ s is selected as this shows minimal error in relation to computational effort and the orthogonal variant is employed as even though it does not improve the semi-implicit scheme but should improve the underlying dynamics as suggested by the precession test.

## 2.6 SUMMARY

To summarise this chapter, the atomistic spin model that will be employed throughout this thesis has been introduced. The spin model formulates the magnetisation dynamics in condensed matter as the dynamics of localised atomic magnetic moments that behave classically as a 3D vector. The main interactions between the atomic moments (spins) are the Heisenberg exchange interaction, uniaxial anisotropy, Zeeman applied field energy and magneto-static dipolar field. These interactions are

parameterised from *ab-initio* calculations where possible to provide a complete description of the system using a microscopic picture.

The specific Hamiltonian for $L1_0$ FePt, which is of interest for high density magnetic recording, has been described. It is formulated using the *ab-initio* calculations of Mryasov *et al.*[20] , who showed that the platinum spin moments are polarised due to the interaction with the neighbouring iron moments. This polarisation is linear with the iron exchange field and so the complete Hamiltonian can be expressed only in terms of the iron moments with mediated exchange and anisotropy terms. It is this Hamiltonian that is used throughout as a model of FePt with the long-ranged interaction due to the Pt mediation.

Two methods of simulating the spin model has been discussed. The first is that of Langevin dynamics, which allows for the time evolution of the spin model through the stochastic Landau-Lifshitz-Gilbert equation (sLLG). Temperature effects are included through a thermal noise term, which is assumed to be in the white noise limit so that the correlation time is negligible compared to that of the spin dynamics. The sLLG is evolved using the semi-implicit integration scheme which during the model tests has been compared to the existing Heun scheme. The semi-implicit scheme has been updated with an orthogonal generator which eliminates some of the error generated from the non-linearity of the damping term in the sLLG. The second method is that of the Monte-Carlo integration; this allows for efficient evaluation of equilibrium properties but also the adaption of the constrained Monte-Carlo method allows for calculation of properties along specified magnetisation directions. As will be shown later this allows for the calculation of the magnetic free energy which is important for developing multi-scale modelling.

The Langevin dynamics has been tested by observing the dependence of the precession frequency on time step and obeying the Boltzmann distribution. The precession frequency was measured for a system with exchange interactions in and applied field. By Fourier transforming the signal the precession frequency and damping is extracted which shows that semi-implicit scheme requires an orthogonal generator to improve stability. Whilst the Heun and orthogonal semi-implicit schemes are both stable, the conservation of the spin length by the semi-implicit scheme is recommends the use of the orthogonal semi-implicit scheme. By comparing the distribution of the spin polar angles to the Boltzmann distribution for both applied field at different temperatures the thermal stability of the Langevin dynamics has been shown.

# 3

# FINITE SIZE EFFECTS ON LINEAR REVERSAL IN FEPT

In Chapter 2 a detailed model of FePt was described whereby the Pt moments are completely described by the Fe moments with mediated parameters. This mediation of the exchange interaction means it is both long range and anisotropic. In this chapter the finite size effects on nanometre grains are investigated using atomistic spin dynamics and constrained Monte Carlo methods. In particular the finite size effects on the linear magnetisation reversal mode are explored at temperature close to the Curie temperature. The chapter begins with an introduction to the linear reversal mechanism and a description of the mono-domain grains using the Landau-Lifshitz-Bloch (LLB) model. This is proceeded by calculations of the equilibrium properties of nanometre grains which allows parametrisation of the LLB. Following this the reversal paths and mean first passage times are calculated. By comparing the switching times to that predicted by the LLB model an estimation of the practical limits of multi-scale modelling can be made.

## 3.1 INTRODUCTION

Iron platinum is a candidate material for high density magnetic recording devices for use with HAMR. The high anisotropy of FePt allows the grain size of media to be taken down to approximately 3 nm before super-paramagnetic behaviour becomes important. On this scale the magnetic properties start to behave in a different manner to that of a bulk system. Small FePt clusters and slabs have been the subject of studies using DFT methods by Chepulskii and Butler[17], and also Cuadrado and Chantrell[16]. These studies have shown that the magnetic moments, exchange interactions and on-site anisotropy are altered by the shape and size of the clusters. As the clusters increase in size the properties become more like that of a bulk system and so to explore the finite size effects in grains not accessible by DFT the interactions calculated for bulk systems are assumed to be valid. As described

previously the exchange interaction for the Fe spins is mediated through the induced Pt spins and extends for approximately 5 unit cells (1.93 nm). In this case in grains that are around 3 nm wide a large number of the atoms in the grain will be 'surface' atoms.

For HAMR not only is the properties of vary small grains important but also how the properties of these small grains differ at temperatures near to the Curie temperature. For the HAMR process to work the grains are heated to close to or above the Curie temperature where the anisotropy has dropped to allow switching using a field of around 1T. Through computational modelling it has become evident that near $T_C$ the magnetisation reverses via a different mechanism to that at low temperature[23, 30]. At low temperatures the magnetisation reversal is characterised by precession and the magnetisation length is constant over the switching process. Close to $T_C$ the reversal does not precess but instead reverses through a linear route where the magnetisation length shrinks and passes through zero before orientating in the opposite direction.

The linear reversal regime is very important in the recording process. In this regime the magnetisation switches not via a precessional route but by a longitudinal contraction of the magnetisation. Along this route the reversal is over the longitudinal barrier leading to a much shorter reversal time. This short reversal time is important for HAMR as it allows for fast switching and reduces the possibility of grains freezing against the field. However current investigations of linear reversal have been restricted to bulk or large nanoparticles. It is the aim of this chapter to investigate how the finite size of grains affect the magnetisation reversal close to the super-paramagnetic limit.

Linear reversal was first highlighted by Kazantseva *et al.*[23] using the Landau-Lifshitz-Bloch (LLB) model derived by Garanin[61]. This is a micro-magnetic model that allows for longitudinal fluctuations in the magnetisation length. The LLB describes the magnetisation dynamics and without thermal noise will follow a path where the free energy is lowest. The reduced free energy derived in the mean field limit[62] is described by

$$\frac{\mathcal{F}}{M_s V} = \begin{cases} \dfrac{m_x^2 + m_y^2}{2\tilde{\chi}_\perp} + \dfrac{\left(m^2 - m_e^2\right)^2}{8 m_e^2 \tilde{\chi}_\parallel} & T < T_c \\ \dfrac{m_x^2 + m_y^2}{2\tilde{\chi}_\perp} + \dfrac{3}{20\tilde{\chi}_\parallel} \dfrac{T_C}{T - T_C} \left( m^2 + \dfrac{5}{3} \dfrac{T - T_C}{T_C} \right)^2 & T > T_c \end{cases} \tag{3.1}$$

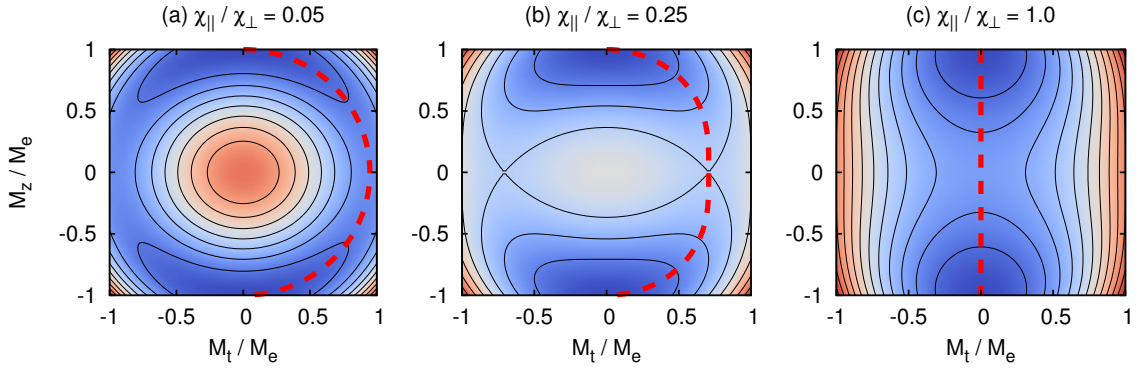


Figure 3.1.: At different temperatures the magnetisation reverses through a different mechanism. At low temperatures (a) the reversal is precessional (circular). As the temperature increases (b) the reversal still precesses but the magnitude decreases in the xy plane (elliptic). At high temperatures close to $T_C$ the reversal is linear with no precession. The colour and contours show the free energy density and the red dashed line shows the reversal path for the specified ratio of susceptibilities.

where $m_e$ is the equilibrium magnetisation and $\tilde{\chi}_{\parallel} = \partial m/\partial h_{\parallel}, \tilde{\chi}_{\perp} = \partial m/\partial h_{\perp}$ are the reduced longitudinal and transverse susceptibilities; all of which depend on temperature. This contains two terms; the first is the longitudinal energy which is keeps the magnetisation at a constant length and the second is the anisotropy energy which is minimised with the magnetisation orientated in the z direction. The longitudinal and transverse susceptibilities describe the strength of each of these terms, and the ratio between them describes the relative strength of the energy contributions. The free energy is mapped in figure 3.1 for increasing susceptibility ratios which correspond to increasing temperature. In (a) the ratio is low and so the longitudinal energy dominates, reversal in this case will be precessional and the magnetisation length will remain constant. (b) shows the case where the reversal will be precessional but the reduction in the longitudinal energy will allow the magnetisation length to reduce to minimise the anisotropy energy, this is known as elliptic reversal. The final case (c) is in the linear reversal regime where the longitudinal energy is weak causing the reversal to pass through a demagnetised state. In each (a),(b) and (c) the reversal path, transverse magnetisation vs $m_z$, is shown to highlight the different reversal paths. Using the free energy the following expression for the orientation dependence of the magnetisation length, $m(\phi)$ for a bulk material is found:

$$m(\phi) = m_e \left(1 - 2\frac{\tilde{\chi}_{\parallel}}{\tilde{\chi}_{\perp}} \sin^2(\phi)\right)^{\frac{1}{2}} \tag{3.2}$$

Equation 3.2 gives an important relationship between the ellipticity parameter and the characteristic parameters of the LLB equation. Specifically, the ratio of the longitudinal and perpendicular susceptibility determines the ellipticity of the reversal path. Equation 3.2 predicts a critical temperature, $T^*$, corresponding to $\tilde{\chi}_{\parallel}(T^*)/\tilde{\chi}_{\perp}(T^*) = 1/2$, at which point the perpendicular magnetisation vanishes. $T^*$ is the critical temperature above which the magnetisation will reverse through the linear switching mechanism. This critical temperature will depend on the strength of the anisotropy and the exact temperature dependence of both the susceptibilities. The linear reversal regime is found close to $T_C$ as it is in this region that the longitudinal susceptibility diverges whilst the transverse remains constant. Whilst the free energy equation is derived in a mean field limit for a coherent macro-spin, a simple first order approach to modelling of finite sized particles is taken by using the parameters calculated for each finite system as the parameters for the free energy.

## 3.2 EQUILIBRIUM PROPERTIES IN FINITE FEPT GRAINS

Following this description we now proceed to calculate the equilibrium properties of FePt grains. By calculating the equilibrium magnetisation and the longitudinal and transverse susceptibilities from the atomistic spin model the free energy can be parameterised for the finite system. A cubic grain of FePt is constructed consisting of a specified number of fct unit cells in each direction. The FePt unit cell is shorter along the [001] direction with a $c/a = 0.969$ so a cubic arrangement of unit cells does not exactly give a cubic grain in real space. An illustration of the grains are shown in figure 3.2, showing three cubic grains of 6, 10 and 14 unit cells. Throughout we focus on grain sizes close to the super-paramagnetic limit, L $\approx 3$ nm.

### 3.2.1 *Equilibrium Magnetisation and Susceptibilities*

The finite size effects on the equilibrium properties of FePt grains can be investigated using the Hamiltonian introduced in Chapter 2 for FePt. In finite grains the long range exchange interaction is significantly truncated for the spins that lie close to the surface. Since the dominant part of the anisotropy comes from the two-ion

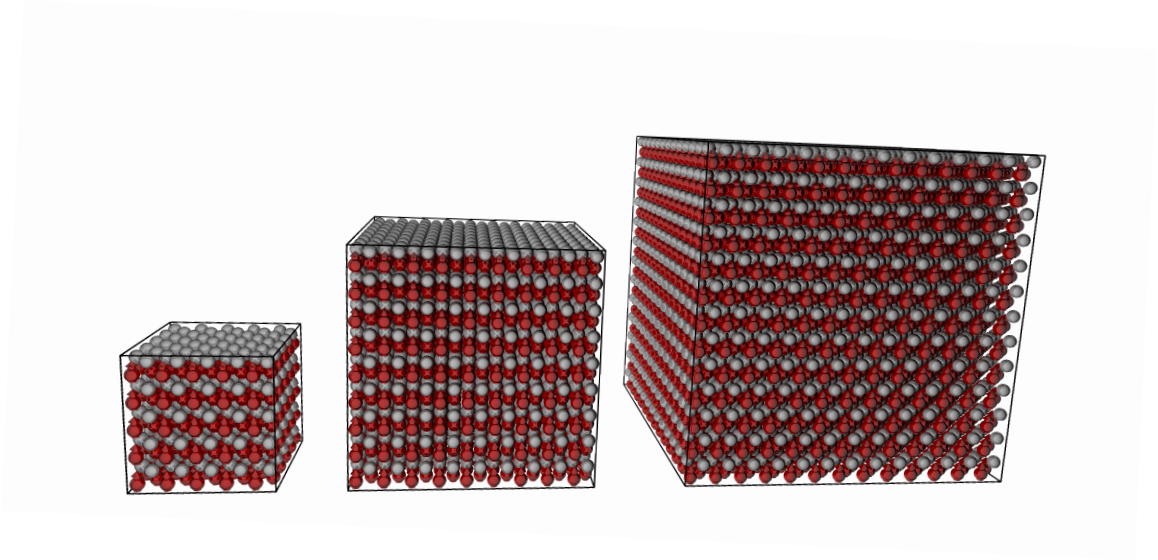

Figure 3.2.: Illustration of 3 different finite size atomistic grains. Red atoms show the Fe spins while silver shows the Pt atoms which are not simulated.

anisotropy term the surface spins will also have a much weaker anisotropy. The loss of neighbours for the exchange interaction means a loss of the magnetic order. Therefore the magnetisation will reduce more with temperature than for bulk systems. This can be observed in the different magnetisation curves in figure 3.3. $T_C$ is also extracted from fitting to the magnetisation curves using the form[63]:

$$m(T, L) = \left(1 - \frac{T}{T_C(L)}\right)^{\beta(L)} \tag{3.3}$$

where $\beta(L)$ is the magnetisation critical exponent that depends on the system size and is included as a fitting parameter. Previously it was described that in the mean field approximation $\beta = 1/2$; Heisenberg ferromagnets typically have $\beta = 0.36$[44] but in FePt, due to the long-ranged anisotropic exchange interaction, it calculated by Hovorka *et al.*[64] to be $\beta = 0.33 \pm 0.10$.

Using the CMC method the angular dependence of the magnetisation length can be found. The free energy predicts that close to $T_C$ the magnetisation length should be smaller when it is orientated in perpendicular to the easy axis. Figure 3.4 shows the angular dependence in the finite grains. There is a clear change in the magnetisation length with angle and the size of this change increases close to $T_C$ and with the size of the grain. The lines show equation 3.2 fitted as a guide to the eye but it is easy to see that the CMC results agree well with the analytic form even for these grain sizes.

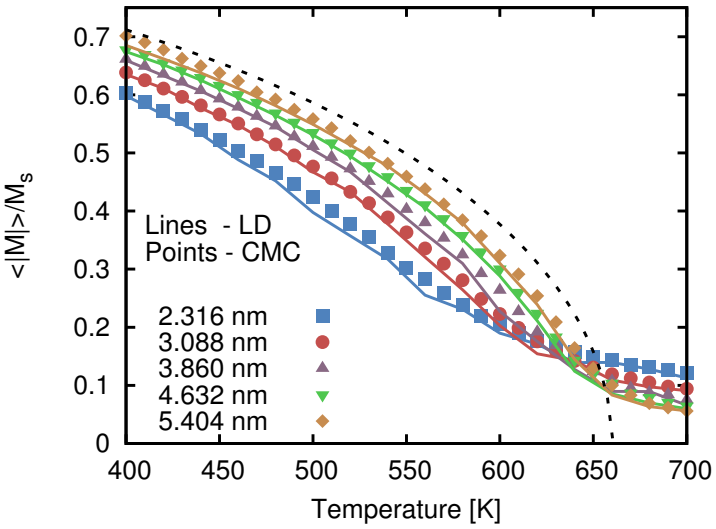


Figure 3.3.: The temperature dependence of the magnetisation for particle sizes of 2.316 nm to 5.404 nm. The dashed black line shows the magnetisation for a bulk system from Ref. 32 for comparison. As the system size decreases the magnetisation below the Curie temperature decreases while above it the magnetisation increases.

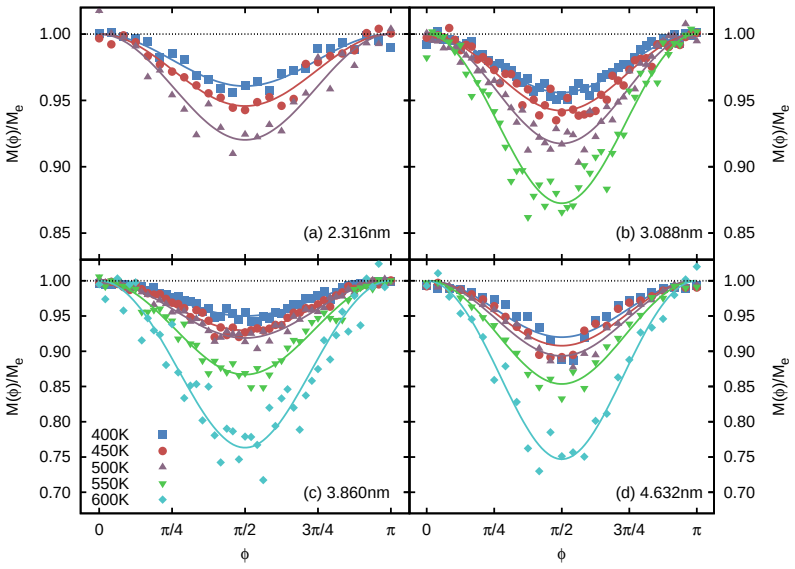


Figure 3.4.: The magnetisation as a function of polar angle calculated using the CMC method for grain sizes (a) 2.316 nm, (b) 3.088 nm, (c) 3.860 nm and (d) 4.632 nm. Different temperatures are shown for each grain size with the points being the CMC results and the solid line equation 3.2 fitted as a guide to the eye.

We now proceed to calculate the longitudinal and transverse susceptibilities that are defined in the LLB free energy. By calculating these from the spin model the critical temperature can be predicted for each grain size. The susceptibilities can be computed directly from the Langevin dynamics simulations, the derivation of this form is given in Appendix A, using

$$\chi_\alpha = \frac{\mu_s N}{k_B T}\left(\langle m_\alpha^2\rangle - \langle m_\alpha\rangle^2\right) \tag{3.4}$$

where $N$ is the number of spins in the system and $\langle m_\alpha\rangle$ denotes the ensemble average of the $\alpha = x, y, z$ component of the reduced magnetisation.

Figure 3.5 shows the longitudinal and transverse susceptibilities calculated from the Langevin Dynamics simulations. The shift in the Curie temperature is clearly visible as the change in the position of the peak in the longitudinal susceptibility in agreement with the magnetisation. For an infinite system $\chi_{||}$ should tend to $\infty$ at the Curie temperature, however as figure 3.5 shows the peaks are finite. As the system reaches the Curie temperature the correlation length diverges but in these finite grains it is limited to the system size thus giving a finite peak in the susceptibility. The noise for the 2.316 nm grain arises from the switching of the magnetisation; at high temperatures the reversal time is much shorter than the simulation time. In this case the average of $m_z$ which is used for calculating the longitudinal susceptibility will tend to zero. This is known as ergodicity breaking[28] but it cannot be easily corrected as of yet. The susceptibilities are fitted in a similar manner to Kazantseva *et al.* where a polynomial is fitted to the susceptibility directly, here the inverse susceptibility is fitted instead which appears to give simple functions:

$$\chi_\alpha^{-1}(x) = \begin{cases} a_0 + a_1 x + a_2 x^2 + a_3 x^3 + a_{\frac{1}{2}} x^{1/2} & x < 0 \\ a_0 + b_1 x + b_2 x^2 + b_4 x^4 & x > 0 \end{cases} \tag{3.5}$$

Where $x = (T - T_C)/T_C$ and $a_n$ and $b_n$ are fitting coefficients. In principle for an infinite system at $T_C$ the susceptibility should be infinite and thus $a_0 = 0$; however for these finite systems the susceptibility does not diverge completely and thus to reach a more accurate fit this term is included.

The ratio of the susceptibilities is shown in figure 3.6, comparing the values calculated from the Langevin dynamics to the fitting functions. The fitting functions agree well except for in the 2.316 nm case, which is due to the switching of the magnetisation. From here the $T^*$ can be readily extracted from the fitted functions, which in the figure can be seen to decrease with system size.

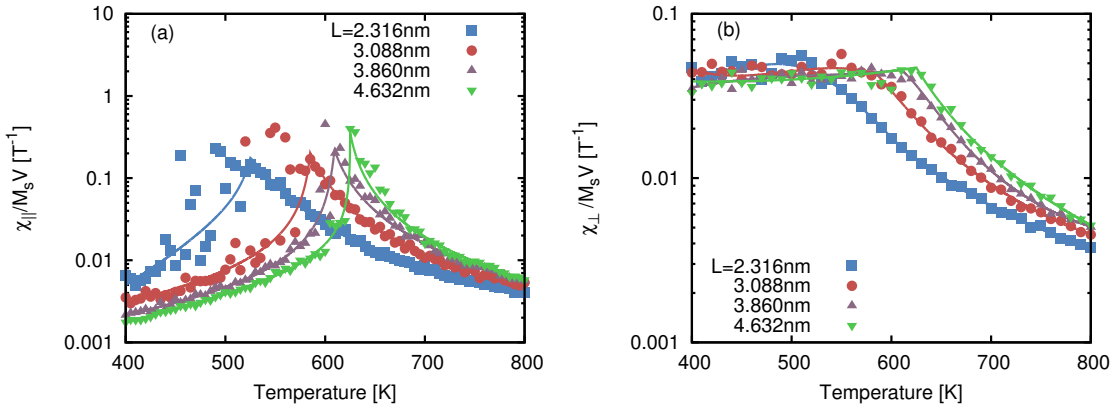


Figure 3.5.: The (a) longitudinal and (b) transverse susceptibilities for each system size. The lines represent polynomial fits to the inverse susceptibilities.

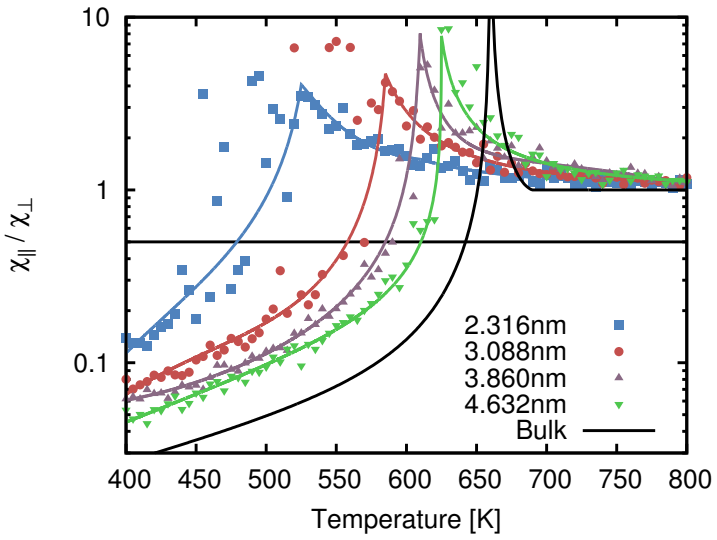


Figure 3.6.: The ratio of the parallel and perpendicular susceptibilities reach a peak at different temperatures consistent with the Curie temperature extracted from the magnetisation. The solid lines show functions that have been fitted the susceptibilities and the horizontal solid line gives $\tilde{\chi}_{\parallel}/\tilde{\chi}_{\perp} = 1/2$ defining the transition to linear reversal.

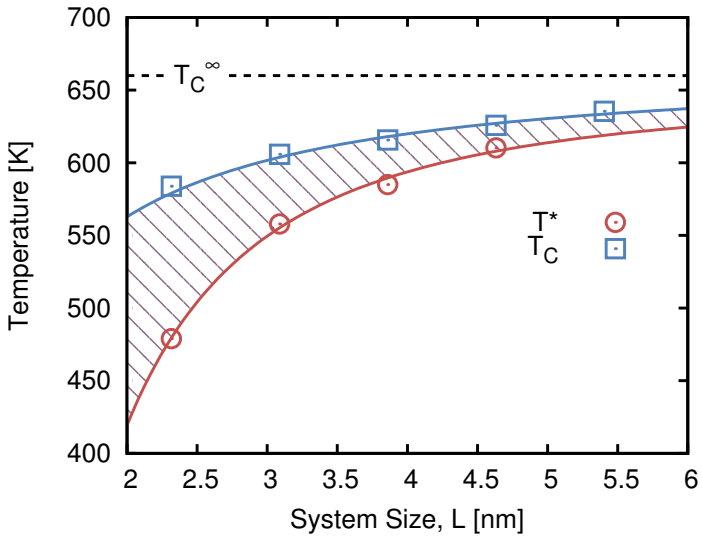


Figure 3.7.: The size dependence of $T_C$ and $T*$ found from fitting to the magnetisation and susceptibility curves respectively. The solid lines show equation 3.6 fitted to the data. The temperature window (indicated by the shaded area) $T* < T < T_C$ appears to widen with decreasing system size.

Figure 3.7 shows the scaling of $T_C$ and $T*$ with the system size as extracted from the fitting. Both $T_C$ and $T*$ drop with size but also the range between them is increasing implying that in the LLB model the linear reversal regime will occur over a larger range. The behaviour of the Curie temperatures can be described well using finite size scaling theory[63, 64]:

$$\frac{T_C^\infty - T_C}{T_C^\infty} = \left(\frac{L}{d_0}\right)^{-1/\nu} \tag{3.6}$$

Here $T_C^\infty$ describes $T_C$ for an infinitely large system, $d_0$ is a system scale constant and $\nu$ is the power scaling constant. These 3 parameters can be used to fit to the extracted Curie and critical temperatures in figure 3.7 and the fitted function agrees very well with the data. From fitting to the Curie temperature results the scaling constant $\nu = 0.86 \pm 0.01$ agrees well with the values computed by Hovorka *et al.*[64] and Lyberatos *et al.*[63].

### 3.2.2 *Free Energy Barriers*

It is the free energy barrier gives the anisotropy barrier that separates the different magnetisation orientations and can be the calculated using the constrained Monte Carlo method. The free energy difference can be calculated using:

$$\Delta F = \int \hat{\mathbf{M}} \times \mathbf{T} \cdot d\hat{\mathbf{M}} \tag{3.7}$$

where the integration is over a reversible path of the magnetisation. The macroscopic torque, $\mathbf{T}$, is shown by Asselin *et al.*[41] to be equal to the ensemble average of the microscopic torques. By calculating the free energy difference along the path by which the magnetisation reverses the anisotropy energy barrier can be calculated. The CMC model is used to simulate the magnetisation at different angles to the z axis. At each constrained angle the average equilibrium magnetisation and net torque is calculated. The integration over the magnetisation can be simplified by moving to polar coordinates and setting the magnetisation as follows

$$\hat{\mathbf{M}} = \Big(\sin(\phi'), 0, \cos(\phi')\Big) \tag{3.8}$$

$$d\hat{\mathbf{M}} = \Big(\cos(\phi), 0, -\sin(\phi')\Big)\, d\phi' \tag{3.9}$$

$$\Delta F = -\int_0^{\phi} T_y d\phi' \tag{3.10}$$

This allows a simple calculation of the free energy directly from the torque. A simple trapezium integration is used therefore it is important that the averages are suitably converged and the angular steps are small.

The free energy and torque are shown in figure 3.8.(a) and (b) for a L=3.86 nm grain at different temperatures. From the definition of the free energy earlier the form of the free energy barrier and torque can be derived.

$$\Delta f = K \sin^2(\phi) \left(1 - \frac{\tilde{\chi}_{\parallel}}{\tilde{\chi}_{\perp}} \sin^2(\phi)\right) \tag{3.11}$$

$$T_y = K \sin(2\phi) \left(1 - 2\frac{\tilde{\chi}_{\parallel}}{\tilde{\chi}_{\perp}} \sin^2(\phi)\right) \tag{3.12}$$

with the anisotropy constant $K = m_e^2/2\tilde{\chi}_{\perp}$ and where the definition of the angular dependence of the magnetisation given in equation 3.2 is used. This crucially shows that the reduction in the magnetisation at high temperatures shows a reduction in the torque and free energy at high temperatures. Theses equations are fitted to the

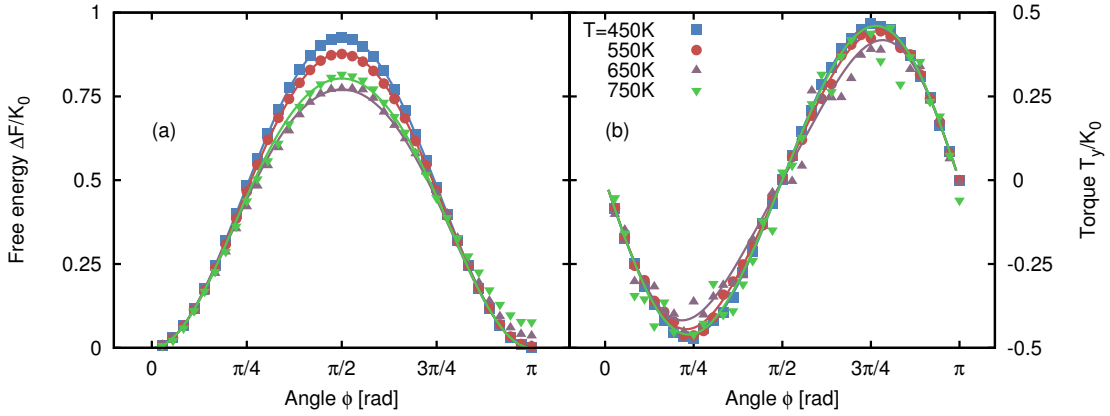


Figure 3.8.: The free energy (a) integrated from the torque (b) for a 3.86 nm grain for T=450K, 550K, 650K and 750K. As the temperature increases the reduction in the magnetisation causes it to reverse over a lower energy barrier.

CMC results in figures 3.8.(a) and (b) which agrees well. It is also important to note that if the torque is fitted with a $\sin(2\phi)$ function to extract the anisotropy constant[65] then there will be a disagreement when the ratio of susceptibilities is large. Here the anisotropy constant (K) is extracted using both the full functions above.

Figure 3.9 shows how the anisotropy constant extracted from the CMC results scales with the magnetisation. Empirically the anisotropy scales as $K(T) \propto M(T)^{2.1}$ and so by plotting the logarithm the exponent can be found. From Callen-Callen theory uniaxial anisotropy scales with a power 3 while the two-ion anisotropy scales with power 2 and so the relative contribution of each to the net anisotropy gives the non-integer power of 2.1 for FePt. As Lyberatos *et al.*[63] discuss, in finite size grains the truncation of the two-ion anisotropy close to the surfaces reduces its contribution to the net anisotropy and so one would expect the exponent to trend towards 3 as the system size decreases.

The exponent is extracted from the linear fit to the anisotropy as shown by the lines in figure 3.9. However it can be seen by comparing the fitted lines to the data in figure 3.9.(a) that there is a significant disagreement at higher temperatures ( $\log(M(T)) \to -\infty$). To improve the fit it is limited to the data $\log(M) < -0.5$ which is shown in the figure. The fitting can be improved upon by using a quadratic function instead; this is shown in figure 3.9.(b). For all the grain sizes the fitting is much more accurate and can be taken over the full data set.

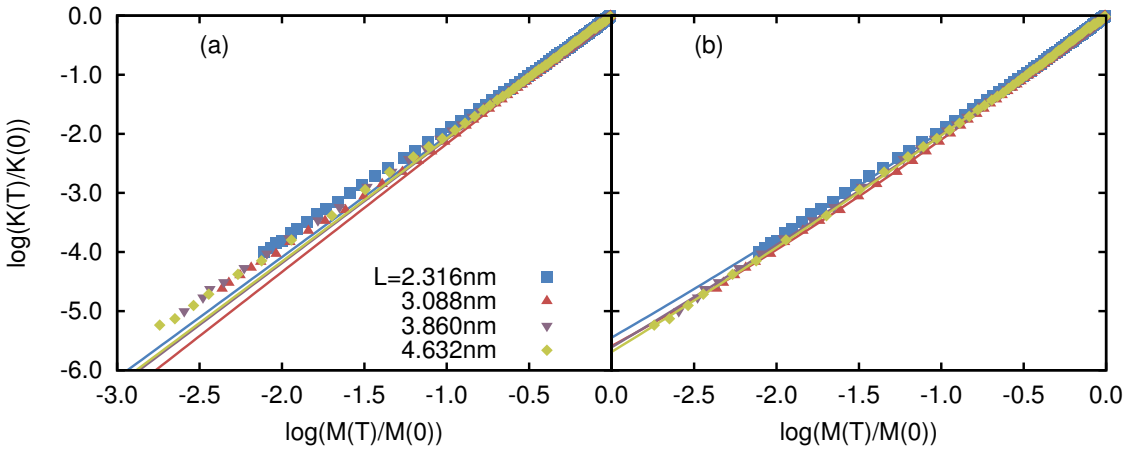


Figure 3.9.: The scaling of the anisotropy with magnetisation. In (a) a linear function is fitted to the lower temperature part while in (b) a quadratic function is fitted. At low temperatures the relation is linear but at higher temperatures it becomes non-linear and the quadratic function fits well over the whole range.

The extracted exponents are shown in figure 3.10 from the linear fitting and quadratic fitting. The results are close to the experimental value of 2.1, especially at larger system sizes but the two smallest deviate significantly. In the case of the 3.088 nm grain the large increase in the exponent is likely due to the reduction in the two-ion contribution to the total anisotropy as previously discussed. However the exponent for the 2.632 nm grain is reduced compared to the experimental result. This is likely to be due to this grain size being at the limit of the theory and behaves in a significantly different manner to the larger sizes.

From the temperature dependence of the anisotropy the zero temperature value can be extracted from the fitting procedure. Figure 3.11 shows how the anisotropy constant scales with system size. Since the majority of the anisotropy is from the two-ion exchange which is reduced for atoms close to the surfaces, as the ratio of surface atoms to bulk atoms increases the net anisotropy per volume decreases.

## 3.3 REVERSAL DYNAMICS

In the previous section the equilibrium properties of the FePt grains were evaluated with the intention of applying these to the LLB formalism. In this section the reversal dynamics are modelled; this can only be done using the Langevin dynamics approach and so the CMC model is not utilised.

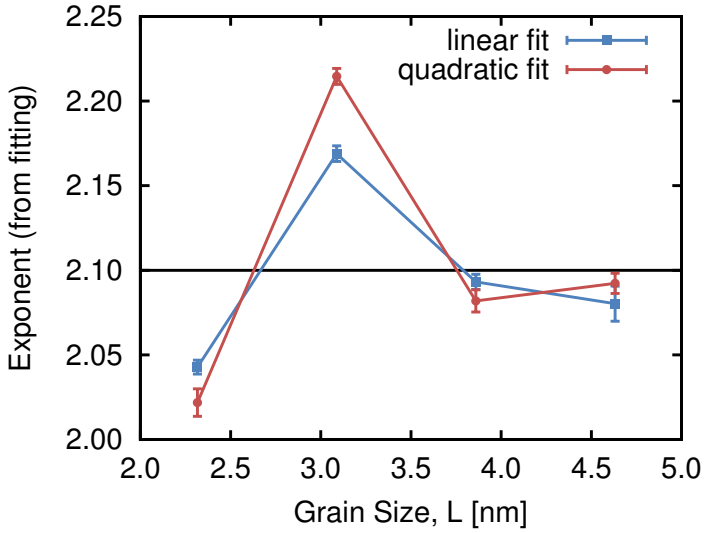


Figure 3.10.: The exponents extracted from fitting to log(K) vs log(M) for the data shown in figure 3.9.

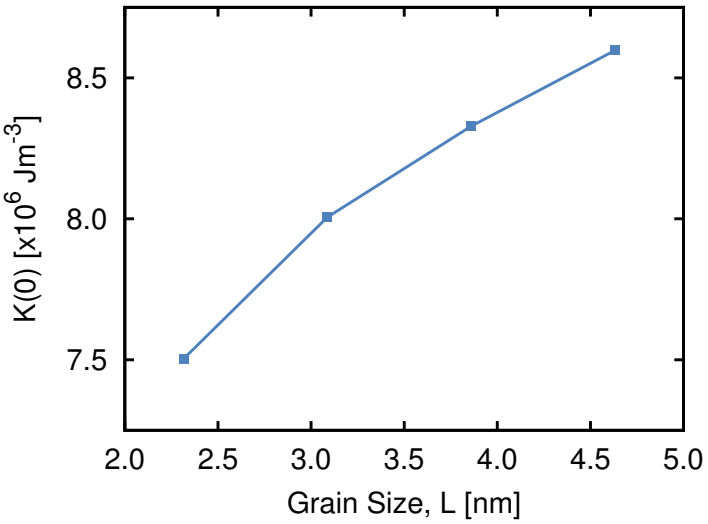


Figure 3.11.: The magnitude of the anisotropy at 0K extracted from fitting. As the grain size decreases the contribution from the two-ion anisotropy decreases reducing the net anisotropy.

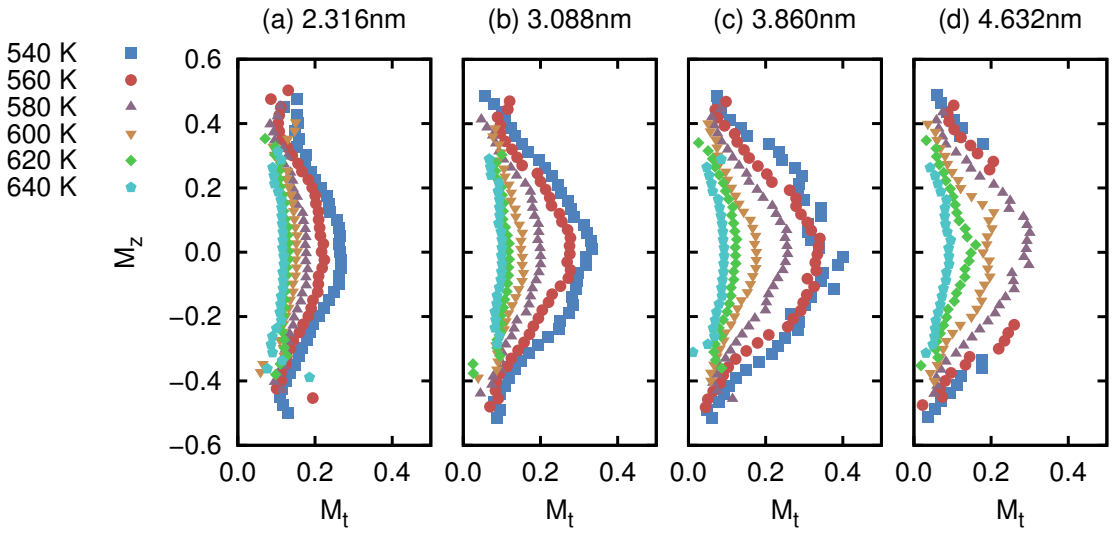


Figure 3.12.: The reversal paths of (a) 2.316 nm, (b) 3.088 nm, (c) 3.860 nm and (d) 4.632 nm systems using a reversing field of 1T. The reversal paths are calculated at different temperatures slightly below the Curie temperature. For the larger system sizes the lower temperatures have not reversed with in the simulation time limit but as the system size decreases at the same temperature the system now reverses within the given time.

### 3.3.1 *Reversal Paths*

To observe the linear reversal mechanism we first compute the path by which the magnetisation reverses. The simulations are performed to a maximum run time of 400 ps and the trajectory of the magnetisation is stored. The reversal path is found by averaging the transverse magnetisation at intervals along $m_z$.

Figure 3.12.(a)-(d) shows the reversal paths for system size 2.314 nm to 4.632 nm using a 1 T field to investigate the temperature dependence of the reversal path. In the 4.632 nm particle the magnetisation does not reverse within the simulation time limit of 400 ps for 540 K and 560 K but then there is a sharp transition to linear reversal, characterised by vanishing transverse magnetisation, at 640K. The smaller systems reverse at lower temperatures but there is a less critical transition to the linear reversal path.

To further investigate the effect of the system size on the transition to the linear regime, we calculate the ellipticity of the reversal paths, defined as

$$e = 1 - \left(\frac{M_t^{\max}}{M_z^{\max}}\right)^2 \tag{3.13}$$

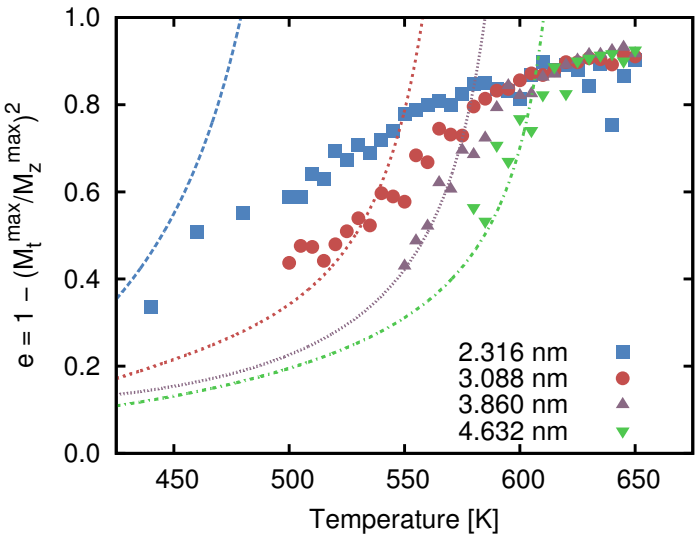


Figure 3.13.: The ellipticity extracted from the reversal paths from figures 3.12(a)-(d) using equation 3.13. The dashed lines show the ellipticity that is expected by the LLB model using the finite size susceptibilities shown in figure 3.6.

The ellipticity is shown in figure 3.13 for the reversal paths shown in fig. 3.12.(a)-(d). As discussed previously the transition to the linear regime (where $e \approx 1$) occurs within a smaller temperature window for the larger systems. Also since the Curie temperature decreases for smaller system sizes the window is centred at lower temperatures. The lines shown in fig 3.12.(e) show the ellipticity from the LLB model which is $e_{\mathrm{LLB}} = 2\tilde{\chi}_{\parallel}(T)/\tilde{\chi}_{\perp}(T)$, this shows that the LLB model reasonably predicts the ellipticity but significant deviations occur for the smaller particles.

### 3.3.2 *Reversal Times*

In terms of HAMR, the temperature dependence of the relaxation time is an important factor. It has been shown by Evans *et* al. [8] that the achievable recording density in HAMR is set by the equilibrium magnetisation at the temperature at which the magnetisation freezes. Consequently, it is vital to the HAMR process for the magnetisation to be as close as possible to the equilibrium value at a given temperature, emphasising the importance of the linear reversal mechanism and its associated fast switching time governed by longitudinal rather than transverse relaxation.

As a measure of the relaxation time we calculate the minimal pulse duration[30]; this is the time taken for $m_z$ to first pass the $m_z = 0$ plane starting from an initial

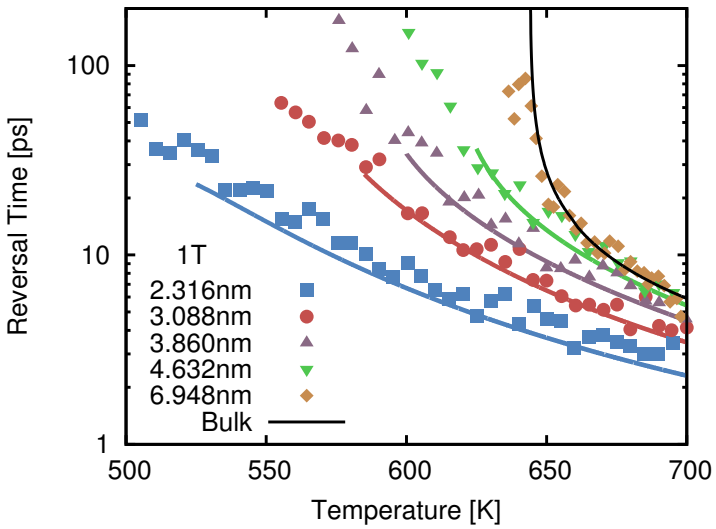


Figure 3.14.: The reversal time in a constant 1 Tesla reversing field. The solid lines show the analytic minimum pulse duration which is derived in reference [23] the parameters for which are calculated from our atomistic simulations for the finite systems while the black line is for bulk.

fully magnetised state. Figure 3.14 shows the minimal pulse duration calculated with a 1 T reversing field relevant to the HAMR process. The results show that there is a significant reduction in the relaxation time in small grains which arises from a convolution of two factors, the decrease of intrinsic properties and the transition from circular to linear reversal. The intrinsic parameters $K$ and $M_s$ both decrease with temperature and depend strongly on the system size. Since a large part of the anisotropy arises from the 2-ion interaction there is a strong decrease with grain size and thus the relaxation time predictable from the Arrhenius-Néel law.[7] In the elliptical and linear regimes the free energy barrier is reduced significantly relative to the coherent reversal mechanism, leading to a further reduction of switching time with temperature over and above that predicted by the Arrhenius-Néel law. We note that both factors are essentially thermodynamic and emerge naturally from the atomistic model.

These results are compared to the expression for the minimum pulse duration derived from the LLB equation by Kazantseva *et al.*[23]

$$t_0^1 = \frac{a}{3m_t^2+b}\left[\ln\left(\left(\frac{(m_t+2)^2+3m_t^2+4b}{4(m_t^2+b)}\right)^{\frac{1}{2}}\left|\frac{m_t}{1-m_t}\right|\right)\right] + \frac{3m_t}{(3m_t^2+4b)^{\frac{1}{2}}}\left[\arctan\left(\frac{m_t+2}{(3m_t^2+4b)^{\frac{1}{2}}}\right) - \arctan\left(\frac{m_t}{(3m_t^2+4b)^{\frac{1}{2}}}\right)\right] \tag{3.14}$$

Where the parameter $m_t$ is the final value of the magnetisation, and the parameters $a$ and $b$ are given by:

$$a = \begin{cases} -2m_e^2\dfrac{\tilde{\chi}_\parallel}{\gamma\alpha_\parallel} & T < T_C \\ -\dfrac{5\mu_0}{3J_0\gamma\alpha_\parallel} & T = T_C \\ -\dfrac{5(T-T_c)\tilde{\chi}_\parallel}{3T_c\gamma\alpha_\parallel} & T > T_C \end{cases} \tag{3.15}$$

$$b = \begin{cases} -m_e^2 & T < T_C \\ 0 & T = T_C \\ -\dfrac{5(T-T_c)}{3T_c} & T > T_C \end{cases} \tag{3.16}$$

The minimum pulse duration depends on the equilibrium magnetisation and susceptibilities so using the values already presented it can be computed for each specific grain size, which are shown as solid lines in figure 3.14. $J_0$ and $\alpha_{||}$ are constants arising from the LLB equation and details can be found in Ref. [23]. There is a good agreement but since the free energy assumes an infinite system the problems arise at size dependent $T_C$ so only the section above is shown. The analytic expression with finite input parameters shows qualitative agreement with the atomistic reversal times showing that for moderate system sizes the LLB equation is applicable using parameters determined for the specific system size. The reversal times for the 6.948 nm particle are similar to the bulk LLB curve. For the smallest system sizes the validity is questionable since it is far from the bulk regime in which the LLB is derived. However, for the sizes in excess of 3.5 nm potentially usable as HAMR media, the parameterisation seems a practical proposition.

## 3.4 CONCLUSION

In this chapter the atomistic spin model was used to investigate the finite size effects in nanometre FePt grains pertinent to the HAMR process. Using Langevin dynamics and CMC the equilibrium properties were calculated. The temperature dependence of the magnetisation and susceptibilities show the the Curie temperature drops consistent with surface effects. The CMC was used to calculate the free energy barrier and the macroscopic anisotropy. For different grain sizes the anisotropy scales different with the magnetisation, deviating from the $M^{2.1}$ behaviour seen experimentally.

The equilibrium properties were used to parameterise the Landau-Lifshitz-Bloch model which can be used in comparison to the atomistic calculations to deduce the feasibility of multi-scale modelling on this scale. The finite size effects on the linear reversal process were investigated through the reversal paths and times. The reversal paths show that the reversal becomes linear at lower temperatures compared to the Curie temperatures in smaller system sizes. The ellipticity compares qualitatively with that expected from the LLB model; it shows that there is a bigger deviation for grain sizes of ≈3.5nm so the limit of the multi-scale modelling is down to this size.

From the results shown in this chapter there are important implications for HAMR. Any grain distribution in the HAMR media will lead to significant distribution in the reversal times as the Curie temperature, anisotropy and reversal mechanism are different over the range of grain sizes simulated. Whilst 3 nm would be the super-paramagnetic limit estimated from the bulk anisotropy the actual limit is likely to slightly larger than this as the loss of the two-ion anisotropy at the surfaces will reduce net anisotropy significantly.

# 4

# SWITCHING PROPERTIES IN GRANULAR MEDIA

The previous chapter investigated how the magnetic properties and dynamics change as the grain size is decreased down to the super-paramagnetic limit. The grains were investigated separate from their surroundings but in magnetic recording media the grains form a large ensemble and interactions between grains are important. The focus of this chapter is the coupling of neighbouring grains together through the inter-layer that is designed to reduce the coupling of grains. First the motivation and details of the atomistic model are described, followed by the calculation of the effective inter-granular exchange for various grain inter-layer density, temperature and grain separation.

## 4.1 INTRODUCTION

As described earlier, storage of binary data on magnetic recording devices utilises magnetic grains as bits of data. Since the stored data is read back from the stray fields produced by the grains, to have a good output signal the data bits need to incorporate many grains. Greater areal densities can be achieved through both the reduction in grain size and also the reduction of the number of grains in each bit. The recording media is grown through deposition techniques and as such the media is granular in structure. To stop the media growing into a continuous film a non-magnetic inter-layer is introduced at the grain boundaries with the aim to decouple the grains from each other. During the deposition process the grains start at nucleation sites and grow until they are almost touching and a high deposition temperature can force the material used as the inter-layer to form at the boundaries of grains[14]. A great deal of effort has been performed to minimise the dispersion of the grain sizes and properties but cannot be removed entirely. This disordered grain structure has an adverse effect on the signal-to-noise ratio (SNR) as it makes the bit boundaries uneven and wider. An example of granular media is shown in

figure 4.1 for FePtAgC and FePtC. Ag and C are included to act as the boundary layer but typically other spacers are used such as oxides ($SiO_2$, $TiO_2$). The grains show a distinct Voronoi-like structure with the spacer separating each grain.

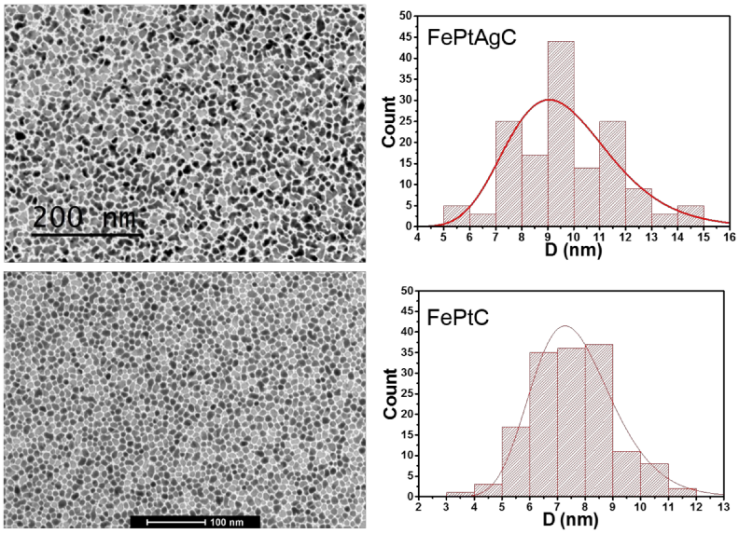


Figure 4.1.: A sample of the grain structure in FePtAgC and FePtC media. Reproduced from Lambert *et al.*[26]

If the inter-layer is thin enough then it is possible for the grains to couple due to the underlying exchange interaction of the atomic spins[66]. This can be removed by increasing the grain separation but this would reduce the packing density of the grains which decreases the areal density and it has been observed that as the grain size decreases the inter-layer thickness also decreases[67] which would increase the coupling. The coupling of the grains together causes problems at the bit boundaries where anti-parallel domains are competing and increases the correlations within the bit. Whilst it is in general undesirable the inter-granular exchange does provide some benefits for recording media as it helps stabilise the grains against stray fields[68] and reduce thermal errors within the bits.

## 4.2 ATOMISTIC MODEL OF INTER-GRANULAR EXCHANGE COUPLING

The model of inter-granular exchange presented here follows on from the work of Evans *et al.*[25], which will be discussed here. The origin of the coupling of neighbouring grains is assumed to occur due to magnetic atoms which are present in the inter-layer material. This happens due to thermal diffusion of the atoms and also arises from the growth process. Different inter-layer materials may support higher

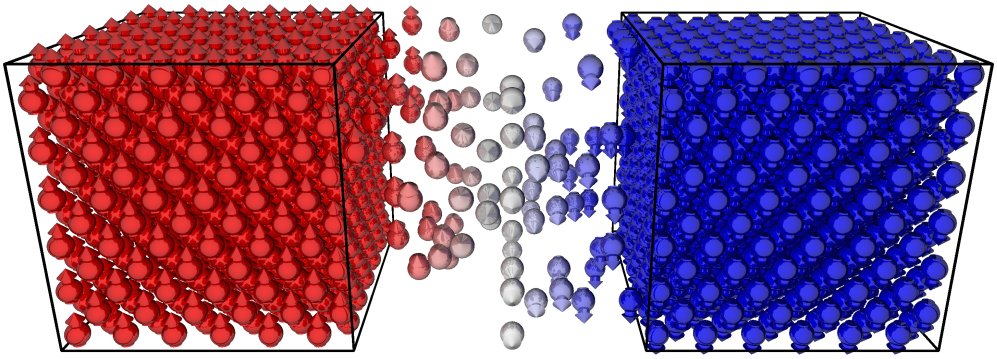

Figure 4.2.: Schematic of the inter-granular exchange coupling due to the chain formation of diffuse magnetic atoms within the oxide inter-layer, here a density of 30% is shown. The colour represents the spin orientation; red $S_z = 1$, white $S_z = 0$ and blue $S_z = -1$

levels of diffusion or longer range interactions between the magnetic atoms. This can be easily represented within the atomistic formalism described so far. In essence the magnetic impurities form a connection that directly connects the grains together despite their separation. This is schematically shown in figure 4.2 for a chain of impurities linking 2 macro-spins. Since the magnetic impurities have diffused within the inter-layer their positions are assumed to be random and therefore will form clusters spanning from one grain boundary to the next, especially when the density is above the percolation limit.

A granular system based on Co with hexagonal grains has been simulated to represent the common grain structure found in magnetic recording media. A hybrid constrained/unconstrained Monte-Carlo algorithm has previously been implemented into the Vampire code[5, 41] which allows us to fix the magnetisation orientation for the grains whilst the spins within the inter-layer are unconstrained and follow the usual Metropolis Monte-Carlo algorithm. A visualisation of the system employed is shown in figure 4.3. Each grain has a side length of 2.5nm giving the diameter from corner to opposite corner of 5nm. The system height was set at 5nm but with periodic boundaries in the z direction to remove any surface effects on the top and bottom planes. In figure 4.3 the inter-layer thickness is set at 2nm but different inter-layer thicknesses are obtained by moving the surrounding grains further away from the central grain.

Since FePt contains long-range interactions and large anisotropy, which would make extracting the inter-granular exchange complicated, a simplified model based on Co is used. The parameters used are $\mu_s = 1.44\mu_B$ and $J_{ij} = 5.6 \times 10^{-21}$J which

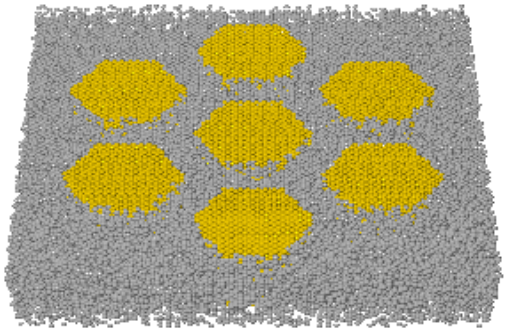

Figure 4.3.: The physical system is setup to represent a hexagonal grain with 6 neighbouring grains. Each grain diameter is 5nm and 5nm tall with periodic boundaries in the z direction. The inter-layer thickness is set at 2nm in this example.

corresponds to $T_C \approx 1280$K. The lattice structure is set as a fcc lattice with the unit cell size $a = 0.354nm$. Due to the hexagonal shapes it is hard to set the inter-layer thickness to be a specific number of monolayers, i.e for the diagonal neighbouring grains, therefore the inter-layer thickness has been specified in nm which is then set within the code.

## 4.3 MICRO-MAGNETIC REPRESENTATION OF INTER-GRANULAR EXCHANGE

On an atomistic scale, the inter-granular exchange is an extension of the direct exchange interaction between the spins. Therefore the inter-granular exchange is described on the micro-magnetic scale where the magnetisation of each grain can be represented by one (or a small group of) macro-spins. Whilst the inter-granular exchange considered here is through the segregant with a low density of magnetic atoms, usual micro-magnetics considers the exchange stiffness[69]. In the long length scale limit the exchange stiffness is given by

$$E_{\text{exch}}^{\text{cont}} = A \int_V (\nabla m_x)^2 + (\nabla m_y)^2 + (\nabla m_z)^2 \, dV, \tag{4.1}$$

where $A$ is the exchange stiffness constant. In this representation the magnetisation is considered to be continuous and thus a gradient can be calculated. For simulation of granular media the grains are considered distinct from their neighbours and thus a gradient is not ideal. In this case the exchange stiffness can be expressed

as the discrete approximation of the gradient and more alike the underlying exchange interaction that it represents. The form in this case is given by:

$$E_{\text{exch}}^{\text{disc}} = \frac{A}{m_e^2 M_s^0} \sum_{i,j} (\mathbf{m}_j - \mathbf{m}_i)^2 \tag{4.2}$$

In both cases an approximate relation for the free energy difference as a function of angle between the two macro-spins can be derived. For the micro-magnetic exchange stiffness if a 1d chain of spins stretching between two macro-spins at an angle $\psi$ to each other is considered. Using a simple formalism where with no anisotropy the spins will spread out over domain wall and can be described by the simple form $M_x(x) = Msin(\psi x/L), M_y(x) = 0, M_z(x) = Mcos(\psi x/L)$. This leaves the energy formed by this domain wall:

$$E_{\text{exch}}^{\text{cont}} \propto \psi^2 \therefore T_y \propto \psi \tag{4.3}$$

In the discrete version of the same simple system the (macro)spins within the chain are separated by an angle $\Delta\phi = \psi/N$, such that $\mathbf{m}_i \cdot \mathbf{m}_{i+1} = m_e^2 \cos(\Delta\phi)$. This leaves the free energy taking the form:

$$E_{\text{exch}}^{\text{disc}} \propto \cos(\psi/N) \therefore T_y \propto sin(\psi/N) \tag{4.4}$$

If the limit of a long domain wall is taken such that $\Delta\phi \to 0$ then the Taylor series of the cosine can be used. In this case $\mathcal{E}_{\text{exch}}^{\text{disc}} \propto \psi^2$ and so the two forms agree with each other. Whilst they do agree within limits it does highlight that it is possible for the inter-granular exchange to take different forms depending on which regime it falls in; at small separations with only a few atomic layers between the grains then one would expect the discrete form as it is dominated by the atomic exchange interaction where as at large separations there is sufficient number of layers to allow the domain wall to take small angular deviations at each layer. Also the simple treatment assumed that the magnetisation stays constant throughout the domain wall but this may not be the case if the system exhibits strong anisotropy[70]. The system under consideration here does not include any anisotropy as this complicates the calculation of the inter-granular exchange and without anisotropy the domain wall width is as large as the structure allows.

With this understanding we proceed to calculate the free energy difference for a system with inter-granular exchange. In the simulations, the surrounding grains are constrained to be fixed in the $+z$ direction and the central grain is constrained at

different polar angles ranging from 0° to 180° in steps of 5°, with $\theta = 0°$ ($m_y = 0.0$). With this setup the torque should have no components in the x or z direction and so the magnitude of the torque is taken, $\tau = |\boldsymbol{\tau}| = \tau_y$. The Monte-Carlo simulations are performed using 10000 steps for equilibration and 20000 steps to gather averages of the properties for each separate constrained angle. With the torque vs polar angle curve outputted from the simulations a linear function is fitted to the curve, focusing on $0 < \phi < 45°$ on which the linear relation is most appropriate.

To extract the strength of the effective inter-granular exchange interaction from the CMC model we proceed using the method described by Evans *et al.* [25], which is repeated here for completeness. To determine the exchange interaction the free energy difference is required which can be computed from the integration of the macroscopic torque, $\tau$. As shown earlier at small angles a linear relation of the torque with polar angle, $\phi$, holds and using this ansatz the integral to recover the free energy difference can be readily solved.

$$\tau = \left(\frac{\partial \tau}{\partial \phi}\right)\phi \tag{4.5}$$

$$\Delta\mathcal{F} = \int_0^{\pi} \tau d\phi \tag{4.6}$$

$$= \int_0^{\pi} \left(\frac{\partial \tau}{\partial \phi}\right)\phi d\phi \tag{4.7}$$

$$= \frac{\pi^2}{2}\left(\frac{\partial \tau}{\partial \phi}\right) \tag{4.8}$$

This can then be equated to the functional form given of the inter-granular exchange coupling. Since we are focusing on granular media it is more convenient to express the inter-granular exchange between two grains $\mathbf{m}_i$ and $\mathbf{m}_j$ as

$$\mathcal{F}_{\text{exch}} = -\frac{\mathcal{J}_{\text{eff}}}{m_e^2}\mathbf{m}_i \cdot \mathbf{m}_j \tag{4.9}$$

Here $\mathcal{J}_{\text{eff}}$ is the effective inter-granular exchange constant that we wish to extract from the atomistic simulations. Using this form the free energy difference between the parallel and anti-parallel is

$$\begin{aligned}\Delta\mathcal{F} &= \mathcal{F}(\pi) - \mathcal{F}(0) \\ &= -\frac{\mathcal{J}_{\text{eff}}}{m_e^2}\left(|m_i||m_j|\cos(\pi) - |m_i||m_j|\cos(0)\right) \\ &= 2\mathcal{J}_{\text{eff}}\end{aligned} \tag{4.10}$$

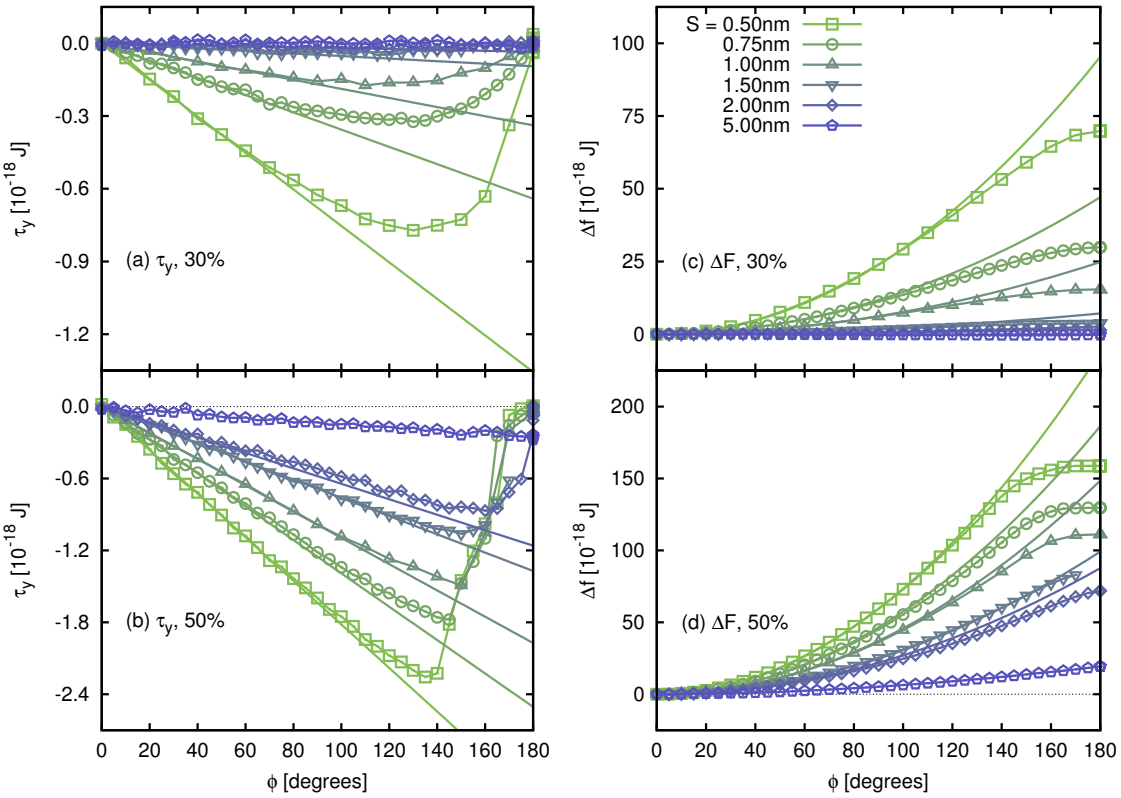


Figure 4.4.: The torque acting on the central grain as a function of the constraint angle for impurity densities of (a) 30% and (b) 50%, and the free energy difference calculated from the torque for again (c) 30% and (d) 50%. The points are from the CMC calculations and the lines show a linear fit to the torque and quadratic fit to the free energy, fitted to the $0 < \phi < 45°$ region.

It is assumed that the magnetisation is constant in the different configurations. Equating these two forms gives a relation between the gradient of the torque and effective exchange constant.

$$\begin{aligned} \Delta F = 2\mathcal{J}_{\text{eff}} &= \frac{\pi^2}{2}\left(\frac{\partial \tau}{\partial \phi}\right) \\ \mathcal{J}_{\text{eff}} &= \frac{\pi^2}{4}\left(\frac{\partial \tau}{\partial \phi}\right) \end{aligned} \tag{4.11}$$

Therefore to obtain the effective exchange interaction from the atomistic simulations the torque is calculated from the ensemble average of the net microscopic torques for different constrained polar angles. The effective exchange interaction is

normalised by the contact area of the grains which contains all 6 of the faces so that the $\mathcal{J}_{\text{eff}}$ presented should be for a single interaction.

The torque and free energy difference calculated for the central grain is shown in figure 4.4. Two densities are shown; (a) and (c) show 30% while (b) and (d) show 50% density, both at 300K for a range of grain separations (S). The solid lines on the graph show a fit; for the torque this is a linear term while for the free energy it is quadratic representing the continuous inter-granular exchange form discussed previously. For the 50% density the torque (4.4.(b)) appears to have a strong linear dependence on the constraint angle up until a certain point when the torque appears to disappear. This is also shown in the free energy (4.4.(d)), as the quadratic fit agrees well for small angle deviations. The 30% density shows a bigger deviation and appears less like the continuous inter-granular exchange form. However it also does not agree with the discrete form either, as the torque would be a sine dependence which this is not. At larger grain separations the continuous form agrees almost exactly, which would be expected as there is a longer range for a domain wall to spread over and minimise the angle between each spin within the chain.

## 4.4 CALCULATIONS OF THE EFFECTIVE INTER-GRANULAR EXCHANGE

The effective inter-granular exchange that is extracted using the method that has been set out depends on a large variety of parameters. The parameters of interest are the density of the magnetic impurities in the inter-layer, the temperature and the separation of the grains.

### 4.4.1 *Dependence On Interlayer Density*

We begin with how the effective inter-granular exchange depends on the density of the magnetic impurities. Figure 4.5 shows the inter-granular exchange for different inter-layer densities with different separations at 300K. There is a strong variation with the density as expected since any clusters formed in the inter-layer will achieve a more effective connection between the grains. Within site percolation theory the percolation threshold for a 3D fcc lattice with 12 nearest neighbours is $p_c = 0.198$. This threshold is the smallest density (or probability of site occupation) at which on an infinite lattice an infinite cluster may appear. Below this density clusters are unlikely to form spanning from one edge to another and thus the inter-granular exchange will be limited. As figure 4.5 shows, at small separations there is still

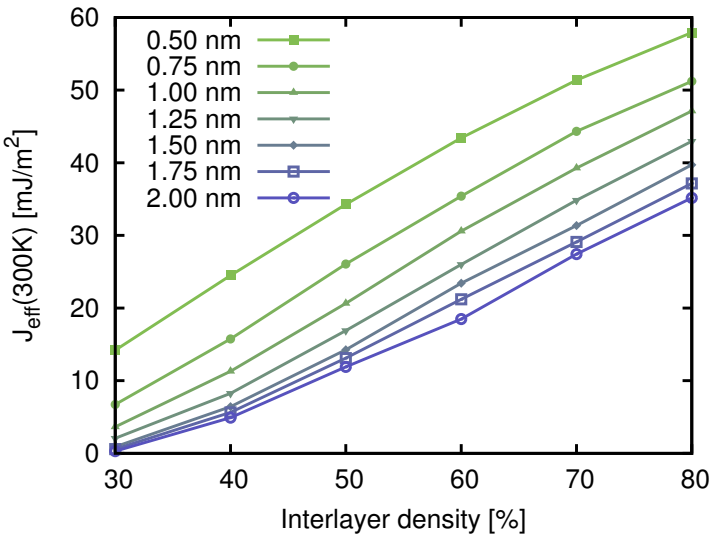


Figure 4.5.: The effective inter-granular exchange strength for different inter-layer thickness and density at 300K.

strong inter-granular exchange even at low densities. This is expected as only a few atomic layers are between the atoms and thus a much higher probability of clusters spanning from each grain. At the larger separations since the densities are above the percolation threshold the inter-granular exchange coupling can extend for larger separations.

### 4.4.2 *Dependence On Temperature*

The temperature dependence of the inter-granular exchange will be important for the HAMR process as while there may exist a larger grain coupling at low temperatures it may be sufficiently weakened at higher temperatures. The temperature dependence of the exchange stiffness has been investigated by Atxitia *et al.*[71], where it is found to scale as $m^{1.76}$ for FePt and $m^{1.745}$ for a generic fcc system. This is the case for a continuous media where the 'grains' are touching and so would represent the zero inter-layer limit of the system considered here. Experimentally the temperature dependence of the inter-granular exchange was measured by Huang and Kryder[72] who found that the coupling energy density drops linearly with temperature which agrees with temperature dependence found by Evans *et al.*[25].

Figures 4.6 and 4.7 show the temperature dependence of the coupling for a inter-layer thickness of 0.5nm and 0.75nm respectively. From the previous bi-layer results it was seen that there is a linear relationship with temperature but here a non-linear

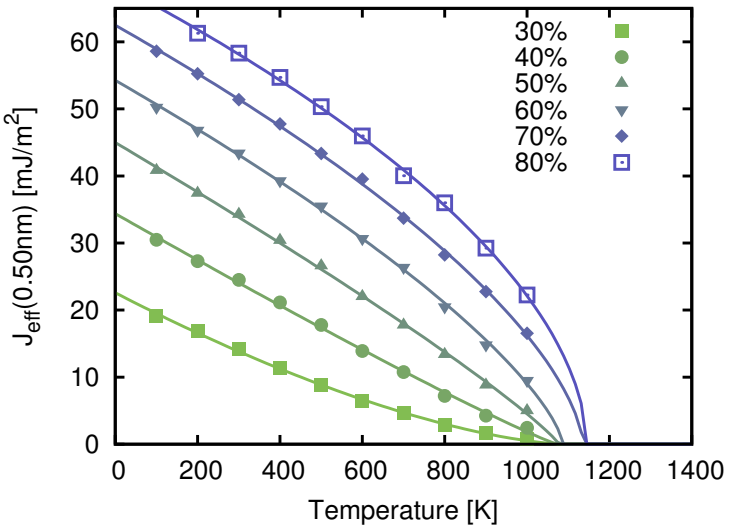


Figure 4.6.: The temperature dependence of the inter-granular exchange at a separation distance of S = 0.5nm. The solid lines show fitted lines to the data points.

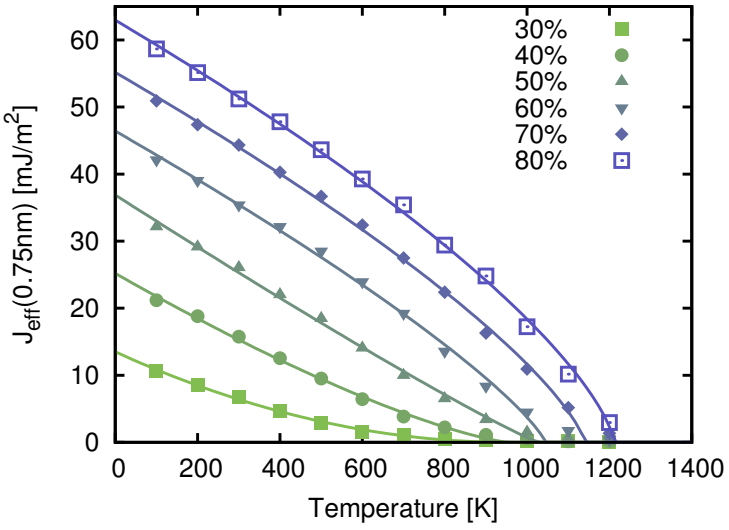


Figure 4.7.: The temperature dependence of the inter-granular exchange at a separation distance of S = 0.75nm. The solid lines show fitted lines to the data points.

behaviour is shown over the wider range of inter-layer densities. The following equation has been fitted to the data, shown as solid lines in figures 4.6 and 4.7:

$$J_{\text{eff}}(T,d) = A(d)\left(1 - \frac{T}{T_C^*(d)}\right)^{\beta(d)} \tag{4.12}$$

With $A(d)$, $T_C^*(d)$ and $\beta(d)$ used as fitting parameters at each density. This models the exchange interaction well and as the density tends to 100% this can be understood as relating to the magnetisation of the inter-layer which is commonly modelled with a similar expression[5]. In these results it is clear that, as to be expected, there is no effective inter-granular exchange above the Curie temperature which relates directly to the HAMR process. At higher densities there is significant change in the exchange close to the Curie temperature which is not present in the smaller densities. After the fitting it appears that the fitting exponent $\beta(d)$ behaves as power law as function of the density. The lines shown in figure 4.8 show a fitted power law to the $\beta(d)$ exponents. This shows that at some density the exponent drops below 1 and thus the temperature dependence becomes more critical close to $T_C$.

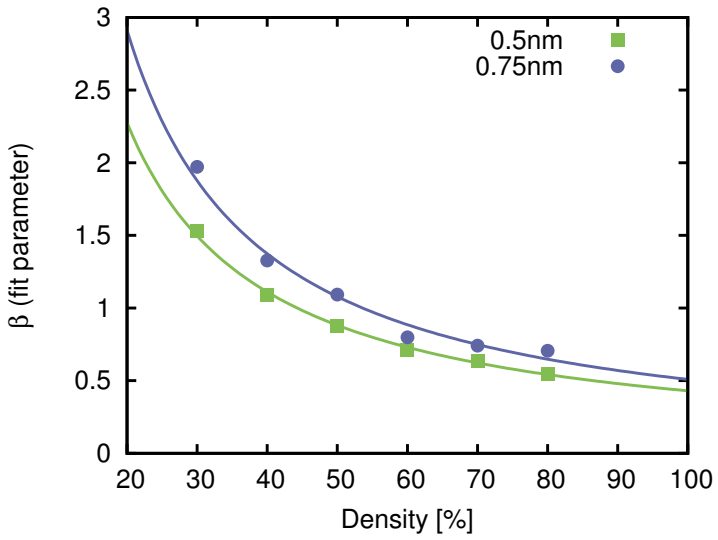


Figure 4.8.: The variation of the fit parameter $\beta(d)$ with the density for a separation of 0.5nm and 0.75nm. There is a apparent power law behaviour with the density, shown by the solid lines.

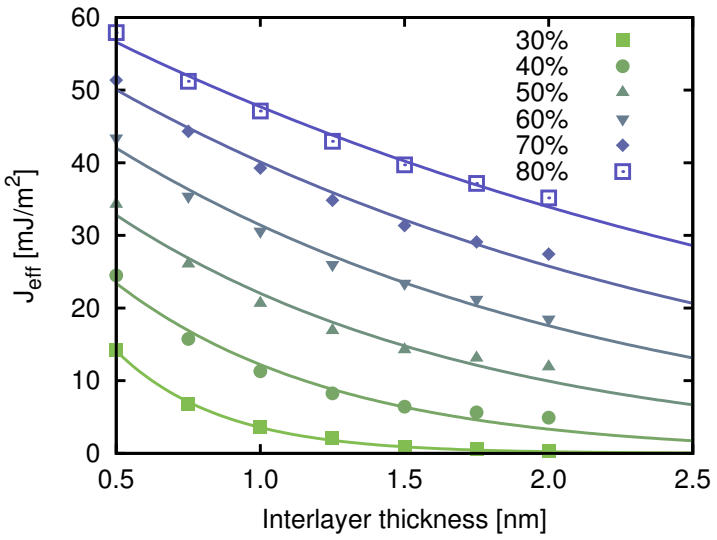


Figure 4.9.: The effective inter-granular exchange strength drops off exponentially with increasing grain separation. Lines show a fitted exponential function to the data points.

### 4.4.3 *Dependence On Grain Separation*

The dependence of the inter-granular exchange on the grain separation is shown in figure 4.9. As in the previous bi-layer simulations[25] and in experimental measurements by Sokalski *et al.*[24] the exchange drops in an exponential manner. The strength of the interaction is comparable to Sokalski *et al.* for inter-layer densities of ≈20%. Since the inter-granular exchange depends strongly on the connections formed by the magnetic impurities this may change significantly if longer range interactions or if the inter-layer structure is different.

## 4.5 CONCLUSION

To conclude, a Co granular system has been simulated using a hybrid constrained/unconstrained Monte-Carlo algorithm that has been previously implemented in the Vampire code[5]. The effective inter-granular exchange has been calculated for a central grain with 6 surrounding neighbours that have a fixed orientation while the central grain is rotated. The effective exchange interaction is shown to increase strongly with inter-layer density above a certain threshold density. The temperature dependence is seen to behave non-linearly with temperature with the exponent strongly dependent on density. With increasing inter-layer thickness the effective

exchange interaction drops exponentially and for low inter-layer densities can be negligible at separations of more than a few nm.

The temperature dependence of the inter-granular exchange interaction has important implications for HAMR, as it shows that above $T_C$ the interaction will have no effect on the magnetisation switching process. In the density regime which would be expected experimentally the temperature dependence decreases faster than the magnetisation implying that even below $T_C$ it may have reduced sufficiently so as not be a hinderance to reversal. Since the inter-granular exchange will reform as the system cools it will help reduce the freezing of grains in the wrong orientation, which can be a big problem for HAMR.

# 5

# ULTRAFAST SWITCHING IN FEPT USING CIRCULARLY POLARISED LIGHT

The previous chapters were concerned with the magnetisation switching of granular FePt relevant to the HAMR process. Now we now turn to a more recent proposition of ultrafast switching using femtosecond lasers. The chapter begins with a brief introduction to the field of ultrafast magnetisation dynamics and the modelling of the heating driven by a femtosecond laser pulse within the atomistic model. We then investigate the required parameters for ultrafast switching in FePt based on the Inverse Faraday Effect (IFE) showing the required field magnitudes and lifetimes. Finally a model for the induced magnetisation in a granular system is considered through the thermal reversal of the grains and a difference in the absorbed energy due to the magnetisation orientations.

## 5.1 INTRODUCTION

The topic of ultrafast magnetisation dynamics is at the forefront of research since it was initially discovered by Beaurepaire *et al.* in 1996[73]. Beaurepaire *et al.* showed that by exciting Ni with a femtosecond laser that the magnetisation changes on a sub-picosecond timescale, much faster than ever assumed possible. What Beaurepaire observed was a demagnetisation that took only a few hundred femtoseconds followed by the magnetisation recovering on a longer timescale of a few picoseconds. 20 years later the understanding of the microscopic processes occurring on this timescale are much better understood but there still remain phenomena that have not been fully explained. The most significant is the phenomenon of All Optical Switching (AOS) whereby the magnetisation can be switched without any external applied field to break the symmetry. This promises to be an important technological advancement as magnetic recording may be possible without the inductive write heads currently required.

## 5.1 INTRODUCTION

Currently all optical switching has appeared to be confined to ferrimagnets with theory and experiments showing that the differential relaxation times and angular momentum transfer of the multiple sub-lattice in these types of materials provide the driving force for switching. It was originally shown by Stanciu *et al.*[74] that the magnetisation in GdFeCo excited by a femtosecond laser pulse will switch depending on the helicity of the light; known as Helicity Dependent All Optical Switching (HD-AOS). In this experiment the laser was swept over multiple domains and it was observed that the helicity of light determined the final state of the magnetisation. Later theory[75] and experiments[29] showed that GdFeCo exhibits helicity independent switching whereby a linearly polarised laser pulse will switch the magnetisation. The driving mechanism from the laser is only the heating caused by it has no angular momentum can be transferred into the magnetic system from the light, thus giving the name Thermally Induced Magnetisation Switching (TIMS). In this case the magnetisation will reverse deterministically from its initial state, therefore the final state will always be switched relative to the initial state.

Therefore while the underlying mechanism is TIMS the observed experimental evidence for helicity dependent switching in GdFeCo relies on the magnetic system absorbing more or less energy from a particular circular polarisation of the laser light. Further experiments on rare earth - transition metal (RE-TM) ferrimagnets and synthetic ferrimagnetic multilayers have expanded the range of materials that exhibit the phenomenon. However it is confined to materials that exhibit a ferrimagnetic structure with two or more sub-lattices interacting anti-ferromagnetically. Recently experiments have shown that all optical helicity dependent switching can occur in ferromagnets. Lambert *et al.*[26] have used different helicities to switch the magnetisation in Co/Pt multilayers and also $L1_0$ FePt granular thin films. The mixing of the ultrafast timescales of all optical switching and the material properties of FePt are of great importance for technological applications.

The thermal induced switching in GdFeCo is driven by the ferrimagnetic coupling of the two RE-TM sub-lattices. This does not occur in FePt as the Pt is polarised and ferromagnetically coupled to the Fe[20]. The Inverse Faraday Effect (IFE) is predicted to generate a magnetic field inside a magnetic material due to the circularly polarised laser pulse.[76] The exact properties of such a field are unknown so here we investigate the required field magnitude and duration required to cause all optical switching in FePt. The IFE was used by Vahaplar *et al.*[77] as an early model for the switching in GdFeCo. Computational work modelled the field generated by the IFE as 20 T field with varying duration. Whilst this showed that a switching

window opens for a peak electron temperatures of between 800K and 1300K for field durations approximately greater than 0.3 ps. Whilst this does go someway to explaining HD-AOS it is based on parameters for an Fe-like material which has a much weaker anisotropy the FePt. As described in the following section the Pt alloying alters the parameters that are used to model the temperature dynamics meaning a higher peak temperature can be reached. This and the difference in the anisotropy mean that the origin of HD-AOS in FePt media is still not well understood and remains an important question.

## 5.2 MODELLING THE LASER HEATING

The incident laser pulse creates a strong non-equilibrium within the sample and as such the electron, phonon and spin sub-systems are treated separately. The spins are treated using the atomistic spin model but the electron and phonon thermal reservoirs are treated phenomenologically using the two temperature model.[78–80] The temporal evolution of the electron, $T_e$, and lattice temperatures, $T_l$, are governed by the following equations[81]:

$$C_e \frac{\partial T_e}{\partial t} = -G_{el}(T_e - T_l) + P(t) - C_e \frac{T_e - T_{\text{room}}}{\tau_{ph}} \tag{5.1}$$

$$C_l \frac{\partial T_l}{\partial t} = G_{el}(T_e - T_l) \tag{5.2}$$

$$P(t) = I_0 F \exp\left(-\left(\frac{t - t_0}{\tau_l}\right)^2\right) \tag{5.3}$$

Where $C_e = \gamma_e T_e$ and $C_l$ are the electron and lattice specific heats. $G_{el}$ is the electron-lattice coupling factor which governs the transfer of energy between the sub-systems. $P(t)$ is the laser power which takes the form of a Gaussian pulse centred at $t_0$ with a pulse width of $\tau_l$ as specified. The fluence, $F$, is incorporated with a proportionality constant, $I_0$. The final term in equation 5.1 represents the cooling of the electron temperature back to room temperature over a timescale $\tau_{ph} = 340$ ps. The parameters for FePt used here are presented by Mendil *et al.*[81], which are calculated to agree with experimental results. Mendil *et al.* describes that because of the Pt alloying the density of states close to the Fermi energy in FePt is smaller than for materials like Fe. This gives the electrons a much smaller specific heat capacity which under the action of the laser pulse drives the electron temperature

| **Parameter** | **FePt** | **Fe-like** | **Unit** |
|---|---|---|---|
| $\gamma_e$ | 110 | 1700 | $\mathrm{J\,m^{-3}\,K^{-2}}$ |
| $I_0$ | $5.0 \times 10^{16}$ | $3.0 \times 10^{17}$ | $\mathrm{cm^{-1}\,s^{-1}}$ |
| $G_{el}$ | $1.5 \times 10^{17}$ | $1.8 \times 10^{18}$ | $\mathrm{W\,m^{-3}\,K^{-1}}$ |
| $C_l$ | $3.7 \times 10^{5}$ | $3.3 \times 10^{6}$ | $\mathrm{J\,m^{-3}K^{-1}}$ |

Table 5.1.: Parameters used in two temperature model for $L1_0$ FePt and a Fe-like material with a high density of states at the Fermi energy taken from reference 81.

to a higher peak value. The parameters given by Mendil *et al.* for $L1_0$ FePt and a Fe-like material are summarised in table 5.1.

The interactions within the two temperature model are shown schematically in figure 5.1. The laser is assumed to couple directly to the electrons and excite them to higher energy states above the Fermi energy. From these high energy states the electrons scatter and thermalise towards an equilibrium distribution. Since the electrons are excited on a very short timescale there is a period where the electrons cannot be described by an electron temperature arising from the Fermi-Dirac distribution. However the electrons thermalise rapidly and it is therefore assumed that the two temperature model is still valid. As the electrons thermalise they interact with phonons and so energy is transferred into the lattice. The spin system is coupled to the electron temperature through the thermal noise term in the Langevin dynamics. The strength of this is controlled by the atomistic coupling parameter, $\lambda$, which phenomenologically represents the underlying electron-spin interactions. Spin-Phonon interactions are possible but are not incorporated here. In materials with large spin-orbit coupling, such as rare-earths, it is possible to couple the magnetic moments to the lattice via a second thermal noise term[33, 82].

The two temperature model described by equations 5.1 and 5.2 is coupled into the atomistic spin dynamics through the thermal noise term:

$$\langle \xi_{i\alpha}(t)\xi_{j\beta}(s)\rangle = \frac{2\mu_s\lambda k_B T_e(t)}{\gamma}\delta_{ij}\delta_{\alpha\beta}\delta(t-s) \tag{5.4}$$

During the simulation the electron and lattice temperatures are updated following a Euler integration step to provide the temperatures at each point in time. The spin temperature ($T_s$) can be calculated directly from the atomistic configuration using the formula given by Ma *et al.*[83]:

$$T_s = \frac{\sum_i |\mathbf{S}_i \times \mathbf{H}_i|^2}{2k_B \sum_i \mathbf{S}_i \cdot \mathbf{H}_i} \tag{5.5}$$

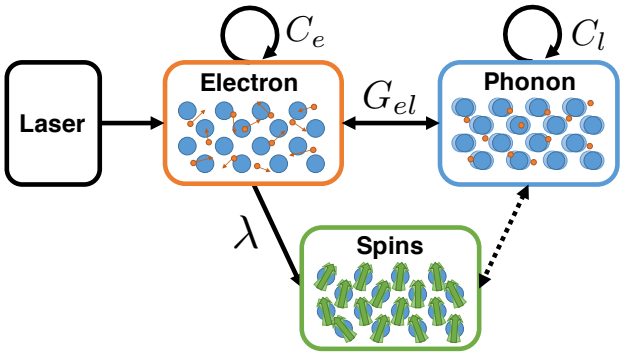


Figure 5.1.: Schematic of the interactions within the two temperature model. The laser adds energy directly into the electron system which then transfers energy into the phonon and spin system. Spin-Phonon interactions are possible but are neglected at this stage.

This expression allows the interaction of the spin system and the two temperature model to be observed. As noted earlier the spin-electron coupling depends on $\lambda$ and this is shown in figure 5.2.(a) for $\lambda$ =0.01, 0.05 and 0.1. $T_e$ and $T_l$ are determined using equations 5.1 and 5.2 using the parameter set for FePt in table 5.1 and therefore do not vary for different $\lambda$. Ma *et al.*[84] consider a feedback mechanism such that $T_e$ and $T_l$ do depend on the instantaneous $T_s$, thus effectively representing a three temperature model, but this is not necessary for the current investigation. As figure 5.2.(a) shows for lower $\lambda$ the peak $T_s$ is lower and the time lag between them is longer. This arises because $\lambda$ controls the strength of the thermal noise term in the sLLG and so the thermal disorder is smaller. The effect on the magnetisation is shown in figure 5.2.(b); since the lower $\lambda$ leads to a lower peak spin temperature the observed demagnetisation is smaller and the demagnetisation time is also longer in agreement with experimental observations[85].

The dynamic response of the magnetisation to the laser pulse is shown in figure 5.3 for a range of fluences. The higher fluences drive the electron temperature to a higher peak value causing a larger demagnetisation of the system. The demagnetisation time is very short due to the higher damping of FePt whilst the remagnetisation time occurs over a few picoseconds. The remagnetisation time is dominated by the ordering of the spins through the exchange field but the formation of spin clusters slows the recovery as the clusters orientate in different directions. At high fluence the system becomes fully demagnetised for a few hundred picoseconds and any field will switch the magnetisation easily at this point.

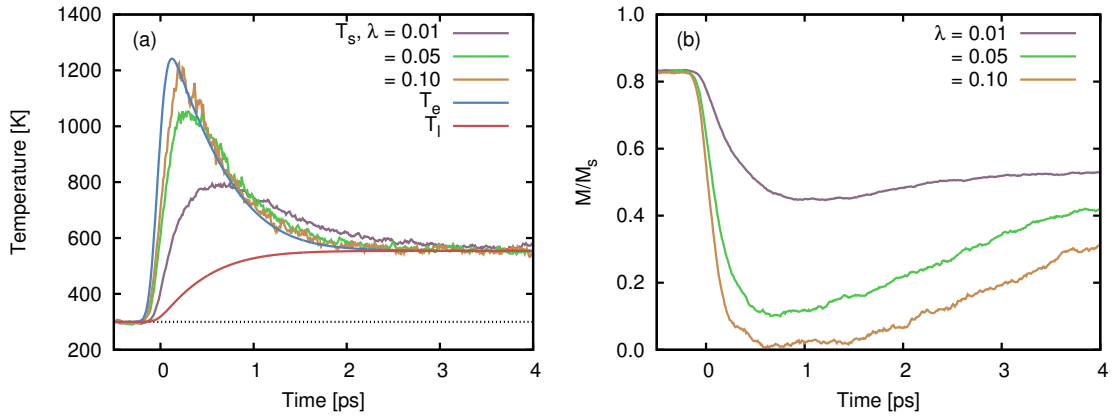


Figure 5.2.: The time evolution of (a) the electron, phonon and spin temperatures, and (b) the magnetisation after a 100 fs laser pulse with a fluence of 12 mJ/cm$^2$ with different damping constants. The lower damping leads to a lower peak spin temperature and causes a smaller demagnetisation with a longer demagnetisation time.

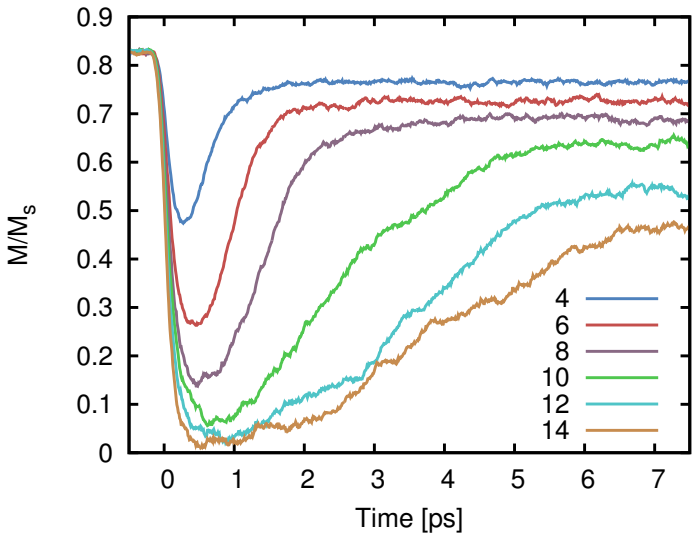


Figure 5.3.: The dynamic response of the magnetisation to laser pulse of different fluence.

## 5.3 THE INVERSE FARADAY EFFECT

In magneto-optics the Faraday effect gives a change in the laser polarisation due to the magnetisation of the sample it is passing through. Following from this it is therefore possible that the inverse relation is possible and the polarisation of the light can act on the magnetisation of the sample; this is known as the inverse Faraday effect (IFE). Early theoretical work on the IFE was presented by Pitaevskii[86] and later observed experimentally by Van der Ziel *et al.*[87] and others. Theoretically the IFE can be described starting from a general thermodynamic potential that incorporates the energy of light-matter interaction[88]:

$$\mathcal{F} = \varepsilon_0 \varepsilon_{ij} \mathcal{E}_i(\omega) \mathcal{E}_j^*(\omega) \tag{5.6}$$

Here $\mathcal{E}_i(\omega)$ is the $i$ component of the electric field at a frequency $\omega$ and $*$ denotes the complex conjugate. $\varepsilon_0$ is the vacuum dielectric constant and $\varepsilon_{ij}$ is the dielectric tensor inside the material. To satisfy symmetry relations the symmetric, $\varepsilon_{jj}^{(\mathrm{s})}$, and anti-symmetric,$\varepsilon_{ij}^{(\mathrm{a})}$, parts depend on the even and odd powers of magnetisation respectively. Therefore they can be expressed as a series expansion in the following manner;

$$\varepsilon_{ij}^{(\mathrm{a})} = \alpha_{ijk} M_k + \beta_{ijk} M_k^3 + \ldots, \tag{5.7}$$

$$\varepsilon_{jj}^{(\mathrm{s})} = \varepsilon_{jj}^{(0)} + \gamma_{ijk} M_k^2 + \ldots, \tag{5.8}$$

where $\alpha_{ijk}$, $\beta_{ijk}$ and $\gamma_{ijk}$ are coefficients and $\varepsilon_{jj}^{(0)}$ is the dielectric tensor without any magnetisation. If we only consider the term linear with the magnetisation the effective field can be easily found,

$$H_k = -\frac{\partial \mathcal{F}}{\partial M_k} = -\varepsilon_0 \alpha_{ijk} \mathcal{E}_i(\omega) \mathcal{E}_j^*(\omega). \tag{5.9}$$

In an isotropic medium, $\alpha_{ijk}$ forms an anti-symmetric tensor with only single scalar constant $\alpha$, so the IFE field takes the form

$$\mathbf{H}_{\mathrm{IFE}} = -\varepsilon_0 \alpha \left[ \boldsymbol{\mathcal{E}}(\omega) \times \boldsymbol{\mathcal{E}}^*(\omega) \right] \tag{5.10}$$

For circularly polarised light the cross product of the electric field vector and its complex conjugate will result in a vector pointing along the direction of propagation. In particular with the incident wave perpendicular to a thin film this will be $\pm\hat{\mathbf{n}}$,

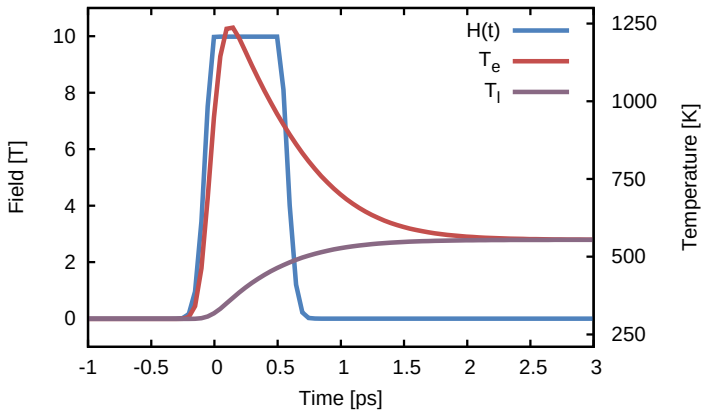


Figure 5.4.: Temporal profile of inverse Faraday effect modelled using a flat Gaussian with a lifetime of 500 fs and the electron and lattice temperatures simulated for a fluence of $F = 12\,\mathrm{mJ/cm^2}$.

where $\hat{\mathbf{n}}$ is the film normal, the sign of which depends on whether it is right (+) or left (-) handed polarisation. While this derivation predicts that a field will be induced due to the dependence of the dielectric tensor on the magnetisation the magnitude of the field depends on the parameter $\alpha$ which is unspecified here.

An alternative description of the IFE is given by Hertel[76], who derives an expression for the magnetisation induced by the inverse Faraday effect within a collisionless electron plasma. In this picture the electric field drives the electron motion which forms a magnetisation which can be related to a generated field through the susceptibility; $M_{\mathrm{IFE}} = \chi H_{\mathrm{IFE}}$. This simple theory was further expanded by Yoshino *et al.*[89] where the magnetic flux density generated by the inverse Faraday effect is related to the optical properties of the material. Using optical constants measured by Cen *et al.*[90] the inverse Faraday field can be estimated but it is in the order of mT. A more detailed model is derived quantum mechanically by Battiatio *et al.*[91] which requires *ab-initio* calculations to parameterise.

Here we proceed by exploring the required magnitude and lifetime of any possible inverse Faraday effect. As stated earlier the IFE field points parallel or anti-parallel to the wave propagation and thus normal to the thin film. For our orientation the film normal is orientated along the z-axis. Thus the IFE field for a given polarisation ($\sigma_\pm$) takes the form

$$\mathbf{H}_{\mathrm{IFE}}(t, \sigma_\pm) = \pm h_{\mathrm{IFE}} f(t) \hat{\mathbf{z}} \tag{5.11}$$

$h_{\mathrm{IFE}}$ is the magnitude of the field and $f(t)$ is the temporal shape of the field. Two temporal shapes of the IFE field are used; first a square shaped field which starts at the peak of the laser power and continues for the desired time. Second is a flat

Gaussian, which is similar to the square field but with Gaussian sides of the same FWHM of the laser. An example of the field with a flat Gaussian shape is shown for a magnitude of 10T and lifetime of 500 fs in figure 5.4. It is shown alongside the electron and lattice temperatures to show the timescale of the field relative to the relaxation of the thermal reservoir.

## 5.4 SWITCHING WITH THE INVERSE FARADAY EFFECT

The field strength and duration are varied to map the possible parameter space for which there is a high probability of switching. The probability of switching is investigated by observing the percentage of samples that are unswitched 10 ps after the application of the laser and opto-magnetic field pulse. To generate a statistical sample the simulation is repeated 25 times with different initial random seeds to generate different trajectories.

The percentage of unswitched grains is shown in figure 5.5 and 5.6 for varying opto-magnetic field strengths and duration for fluences of 8 $\mathrm{mJ/cm^2}$ and 10 $\mathrm{mJ/cm^2}$. The results show that there is a clear boundary beyond which the grains will switch with a high probability. By comparing the different fluences we see that the transition into the switching regime is sharper in the lower fluence. This is likely due to thermal activation since in the higher fluence the peak temperature is higher and thus the magnetisation will experience larger thermal fluctuations and a reduced anisotropy barrier. From these results the assumption of a field generated by the inverse Faraday effect must either occur for a duration near to a picosecond or generate field strengths of many Tesla. Certainly if the switching is to be deterministic both cases would be required.

Using the Landau-Lifshitz-Bloch model Kazantseva *et al.*[23] derived a expression for the relaxation time required for the magnetisation to switch at a constant temperature. This expression, the minimum pulse duration, allows us to predict for a given opto-magnetic field strength a required field duration. The solid lines in figure 5.6 show calculated minimum pulse duration parameterised for the FePt system. Whilst a direct comparison is not exact, since the temperature is not constant, if an effective temperature estimated from the average spin temperature over the field duration is considered there is good agreement. For this fluence an effective temperature of 900K (c.f. figure 5.9.(e)) shows the approximate boundary for the switching regime.

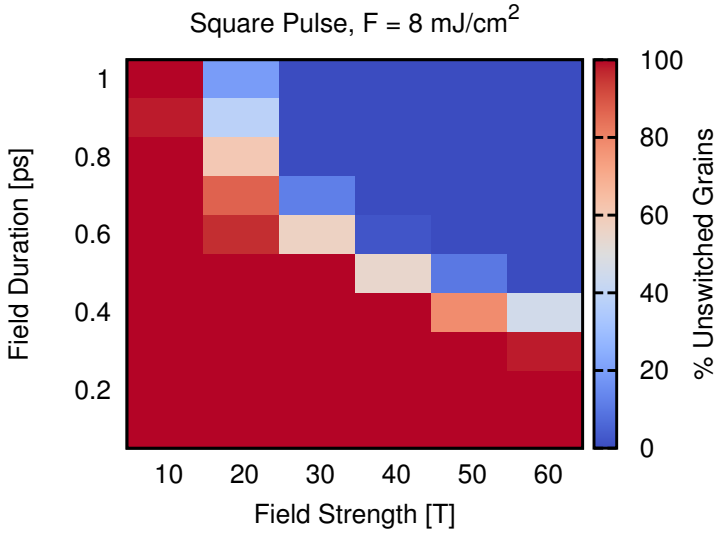


Figure 5.5.: Ratio of unswitched grains for different square field pulse duration and strengths for a laser fluence of F = 8 mJ/cm$^2$.

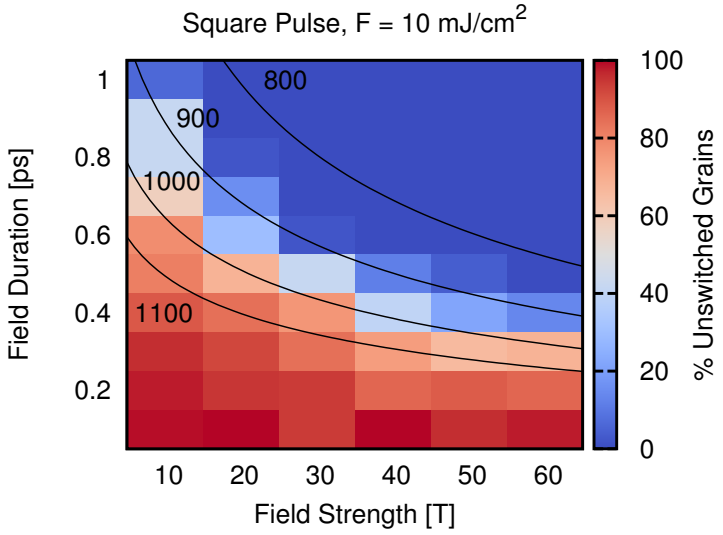


Figure 5.6.: Ratio of unswitched grains for different square field pulse duration and strengths for a laser fluence of F = 10 mJ/cm$^2$. The solid lines show the minimum pulse duration as calculated from the Landau-Lifshitz-Bloch equation at the specified temperatures.

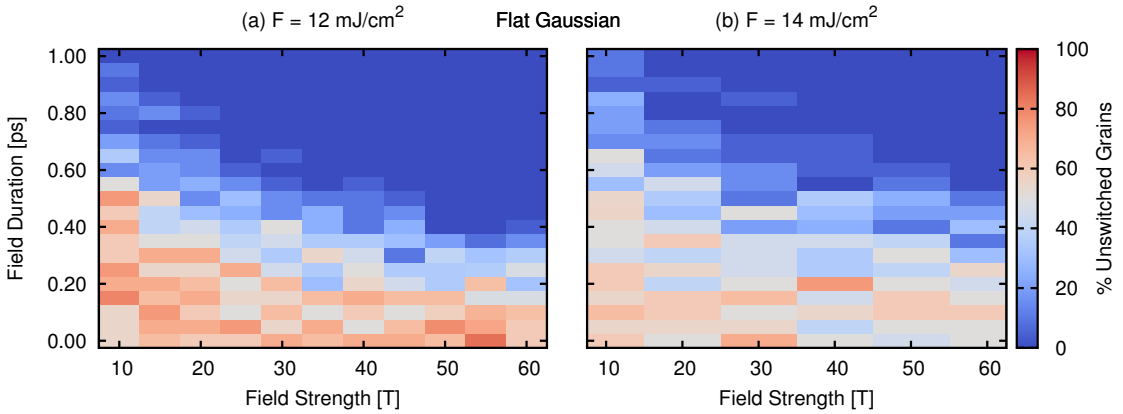


Figure 5.7.: Percentage of unswitched grains at (a) F = 12 mJ/cm$^2$ and (b) F = 14 mJ/cm$^2$ for a inverse Faraday field modelled by a flat Gaussian for varying strengths and duration. The sides of the field are Gaussian shaped with a width of $\tau_l = 100$ fs.

Figure 5.7 shows the percentage for unswitched grains for fluences of (a) 12 mJ/cm$^2$ and (b) 14 mJ/cm$^2$ now using a flat topped Gaussian to represent the IFE field. The flat Gaussian represents the smooth rise and decay of the laser pulse; the same Gaussian width of the laser pulse is used (100fs) but it is extended by a fixed duration. This does not alter the results significantly as it seems to just create a slightly longer effective duration compared to the square pulse. Since the fluence is higher here we see that the regions which were unswitched at lower fluence are now tending to a random switching of the magnetisation. The heating is the dominant factor as the field is too short or weak to largely bias the switching and so the percentage unswitched is tending to 50%. Even at these higher fluences the almost deterministic switching region is similar to those of lower fluences. This is mainly due to the extra field required to overcome the higher thermal noise and to limit thermal activation against the field.

The mean first passage of the magnetisation is shown in figure 5.8 for a fluence of F = 12 mJ/cm$^2$. Clearly when the field duration is longer than the average time to switch for that given field strength then the mean first passage time does not change. The dashed line shows where the mean first passage time equals the field duration, and to one side of this the data points do not vary significantly. At lower field durations there appears to be a certain chance that switching is aided by thermal effects. At very short field duration it appears that the switching is random and due to the demagnetisation.

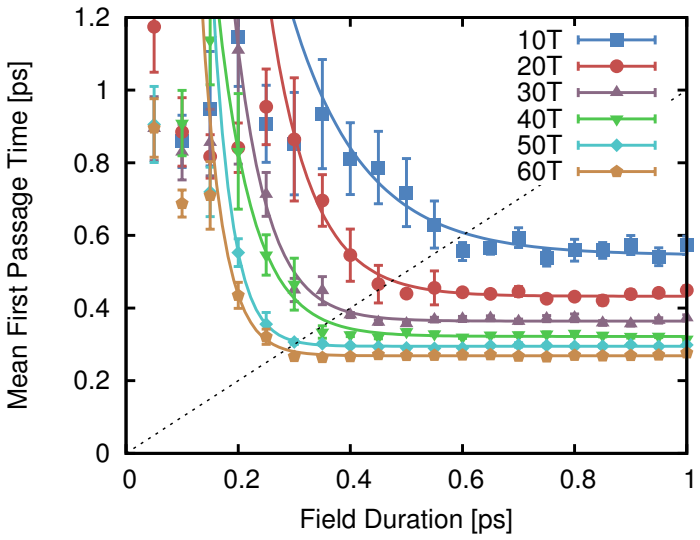


Figure 5.8.: The mean first passage times for different field durations and strengths. The solid lines are exponential fits to guide the eye and the dashed line shows where the mean first passage time is equal to the pulse duration. The mean first passage time saturates as the field duration increases as beyond this point the magnetisation has already switched.

## 5.5 ACCESSING THE LINEAR REVERSAL MODE

Whilst the inverse Faraday effect is assumed to create a field which is the dominant cause for the switching the laser heating is also highly important. At higher temperatures the switching mechanism is through the linear reversal mode described previously. In this regime the magnetisation switched with a collapse of the magnetic order before reforming in the switched direction. Therefore the timescale is on the order of the longitudinal relaxation time which is much faster than the transverse relaxation time characterising precessional switching.

Figure 5.9 shows the switching mechanism at different fluences with a 30 T opto-magnetic field with a duration of 1 ps. Fig. 5.9.(a) shows the switching at a low fluence (6 mJ/cm$^2$); the switching occurs due to the large field chosen but because the peak temperature is low and the system does not spend sufficient time above the Curie temperature the switching proceeds by precessional reversal shown by large transverse magnetisation components. The corresponding temperature profile is shown in (d). This shows that the system temperature only peaks briefly above the Curie temperature before reaching a low final temperature thus corresponding to the precessional reversal.

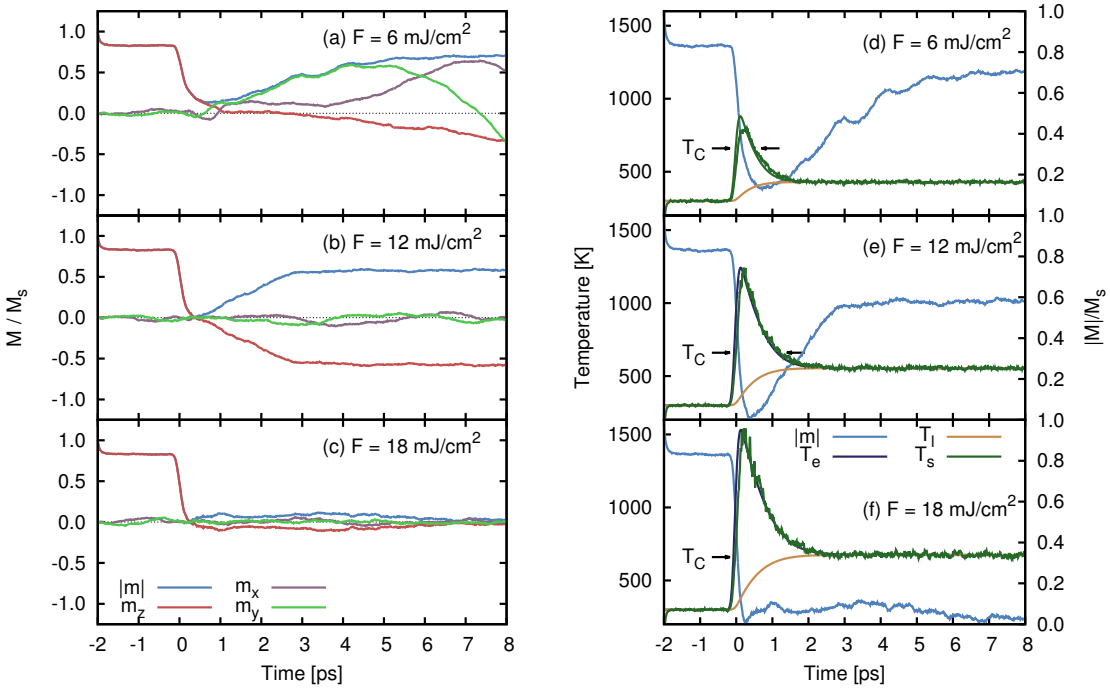


Figure 5.9.: The switching dynamics at different fluences with an field of 30T for 1ps. (a)-(c) show the switching dynamics at different fluences while (d)-(f) show how the temperature evolves with time. In (d)-(f) the arrows indicate where the system passes the Curie temperature.

Since the damping of FePt is assumed to be relatively large ($\lambda = 0.1$) there is only a short delay between the electron and spin temperatures. At a higher fluence, fig. 5.9.(b) the switching has no transverse component and occurs within a few hundred femtoseconds after excitation. The corresponding temperature profile, fig. 5.9.(e), shows that the system is above the Curie temperature for a significant time and within the linear reversal regime. However when the fluence is too high, fig. 5.9.(c) and (f), the final temperature is above the Curie temperature and so while the magnetisation switches initially it remains in a demagnetised state.

## 5.6 MAGNETIC CIRCULAR DICHROISM MODEL OF SWITCHING

From the previous results the required opto-magnetic field generated through the IFE would need to have a considerable magnitude and duration to cause switching. This is in part due to the large anisotropy of $L1_0$ FePt and also due to the heating process caused by the laser. An alternative explanation for the induced magnetisation in granular FePt measured by Lambert *et al.* is that the switching occurs by

thermal activation due to the high temperatures caused by the laser. By itself this would only lead to a demagnetised sample but if one orientation of the magnetisation was to absorb more energy from the laser then it would have a higher probability of thermally switching compared to the other orientation. In a large ensemble of grains this would lead to more grains with their magnetisation along the orientation that absorbs less energy from the laser and thus a net magnetisation.

The differential absorption of energy with circularly polarised light due to the magnetisation is known as Magnetic Circular Dichroism (MCD) and is extensively used with X-rays to probe the magnetic properties of materials. The role of MCD in the helicity dependent switching in GdFeCo was examined by Khorsand *et al.*[92] where it was found that the earlier HD-AOS could be explained by the combination of the MCD and TIMS. The TIMS provides the switching mechanism and the helicity dependence is determined by the MCD effect. As for the ferromagnetic materials of interest here, there is no underlying TIMS to causes switching and so only the thermal activation is a possible route to HD-AOS.

### 5.6.1 *Thermal Switching Of Grains During Laser Heating*

Since this model of HD-AOS relies on the random nature of thermal switching, the induced magnetisation will require a large ensemble of grains to be observed. In this case it will be hard to simulate directly using the atomistic spin dynamics due to the size limitations of model. Therefore to construct a description of the process and to analyse what level of induced magnetisation is possible using the MCD effect a different approach is required. In $L1_0$ FePt the magnetisation orientation can be considered binary; either up ($+\hat{\mathbf{n}}$) or down ($-\hat{\mathbf{n}}$) which we orientate along the z-axis. So the ensemble can be modelled as the probability of each grain occupying one of these 2 states and the time evolution of these probabilities is governed by the Master equation. For a system of N states the evolution of the probability of occupying state $i$, $p_i$, is given by

$$\frac{\partial p_i}{\partial t} = \sum_{j=1}^{N} \mathcal{W}_{ij} p_j. \tag{5.12}$$

$\mathcal{W}_{ij}$ is the transition matrix which is formed from the transition rates $\tau_{ij}^{-1}$ of moving from state $i$ to $j$. To proceed the transition rate of a single grain moving from an up to down (or vice-versa) is required; this can be calculated using the atomistic spin model which then provides a detailed model of the switching. Since the switching

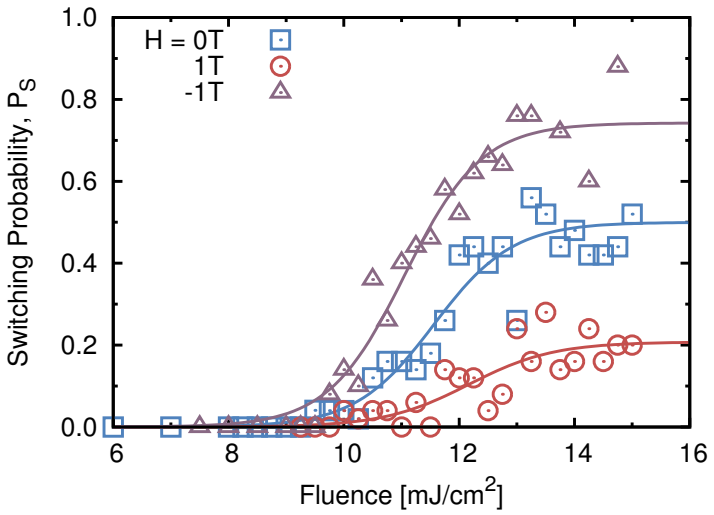


Figure 5.10.: The probability of a single grain switching without the inverse Faraday effect. Even without a field the grain thermally switches when the fluence is high enough to demagnetise the grain. Above F = 16 mJ/cm$^{-2}$ the system is above the Curie temperature and will cool over a longer timescale. The switching is also calculated for a constant field of 1T either aligned or anti-aligned with the grain direction. The lines show a fit to the data.

is through a highly demagnetised state the inter-grain interactions can be ignored. The transition rate is calculated by performing multiple independent simulations for a range of laser fluences and finding the ratio that have switched 10 ps after the laser pulse. This considers a single switching event over the course of a single laser pulse. The combination of this transition probability and the laser repeat frequency, $f_l$, gives the transition rate ($\tau^{-1}$),

$$\tau^{-1}(F) = f_l P_s(F) \tag{5.13}$$

Figure 5.10 shows the probability of a grain switching during the laser heating process. Below 8 mJ/cm$^2$ there is no thermal activation as the system does not demagnetise significantly. Above 8 mJ/cm$^2$ there is a possibility for the grains to end in the reversed direction and the probability increases strongly with fluence until about 16 mJ/cm$^2$ where the heating would leave the system above the Curie temperature. At this point the grains would be evenly distributed between up and down and so the probability of switching would be 1/2. The effect of an applied field that is constant over the whole laser pulse can be seen to raise or lower the

| H | 0 | 1 | -1 | [T] |
|---|---|---|---|---|
| $P_\infty$ | 0.50 | 0.21 | 0.74 | |
| $F_0$ | 11.56 | 11.06 | 12.17 | [mJ/cm$^2$] |
| $\Delta F$ | 1.37 | 1.33 | 1.47 | [mJ/cm$^2$] |

Table 5.2.: Fitting parameters for probability of switching as a function of fluence for zero field and ±1T. All parameters have a dependence on the field but most important is the variation of $P_\infty$.

switching probability whether it is anti-parallel or parallel to the initial direction respectively. The probability does not tend to 1 for H = -1T as the thermal effects can also cause back switching against the field which is a important problem for HAMR[93]. To provide a functional form to the data in figure 5.10 the following equation is fitted:

$$P_\mathrm{s}(F) = \frac{P_\infty}{2}\left(1 + \tanh((F - F_0)/\Delta F)\right) \tag{5.14}$$

The fitting parameters are given in table 5.2; showing that all three parameters depend on the field. The variation of $P_\infty$ is most important. Calculating a switching for more fields would give a compete description but a linear interpolation of the values is used to give an estimate of the field effects.

### 5.6.2 *Two Sate Master Equation Model*

Using the probability of switching calculated from the atomistic spin dynamics the Master equation can now be constructed to estimate the induced magnetisation due the magnetic circular dichroism. To make a distinction between the probability of occupying a state and the probability of switching the notation, $n_\pm$ is used here. These are the probability of the grain having a magnetisation that is orientated such that it absorbs more or less energy through the MCD effect; $n_+$ or $n_-$ respectively. This can be easily seen ratio of grains in either state in relation to the total number of grains. Each state has a magnetisation of $m_z = \pm m_e$, where $m_e$ is the equilibrium magnetisation for a given temperature. Therefore the net reduced magnetisation of the ensemble will be

$$m = n_- - n_+. \tag{5.15}$$

This is the magnetisation along the orientation of the state that absorbs less energy. From this the two state Master equation can be constructed as follows:

$$\frac{\partial n_+}{\partial t} = -n_+\tau_+^{-1} + n_-\tau_-^{-1} \tag{5.16}$$

$$\frac{\partial n_-}{\partial t} = -n_-\tau_-^{-1} + n_+\tau_+^{-1} \tag{5.17}$$

where $\tau_\pm^{-1}$ are the transition rates of the grain switching from the high (+) or low (−) absorption states to the opposite state. The fitted function gives the probability of switching over the range of fluences. To incorporate the effect of magnetic circular dichroism the transition rates are assumed to have an effective fluence with is larger or smaller by a specified ratio for each of the two states.

$$\tau_\pm^{-1}(F) = f_l P\left(F\delta_\pm\right) \tag{5.18}$$

The attempt frequency, $f_l$, is set by the laser repeat rate which in experiments is 1 kHz. The difference in the absorbed fluence due to the different magnetisation orientation is modelled using the factor $\delta_\pm = 1 \pm \Delta/2$. $\Delta$ is the MCD ratio which is assumed to be a few percent. The equilibrium values are found by finding the stationary state, $\partial n_-/\partial t = \partial n_+/\partial t = 0$, which gives the criteria

$$\frac{n_-^\infty}{n_+^\infty} = \frac{\tau_-}{\tau_+}. \tag{5.19}$$

From this the equilibrium induced magnetisation in the low absorption direction, $m^\infty = n_-^\infty - n_+^\infty$, can be derived by making use of the total probability must be normalised, $n_+ + n_- = 1$. This gives the expression;

$$m^\infty = \frac{\tau_- - \tau_+}{\tau_+ + \tau_-}. \tag{5.20}$$

Solving equations 5.16 and 5.17 the time dependence of the induced magnetisation is given by

$$m(t) = m^\infty - (m^\infty - m(0))e^{-\frac{t}{\tau}}, \tag{5.21}$$

with the magnetisation relaxation time is given by

$$\frac{1}{\tau} = \frac{1}{\tau_+} + \frac{1}{\tau_-}. \tag{5.22}$$

The transition times $\tau_\pm$ and the magnetisation relaxation time $\tau$ are shown in figure 5.11.(a) for an example MCD $\Delta = 5\%$; normalised by the repeat rate of the laser such that they are expressed as a number of pulses. At low fluence the

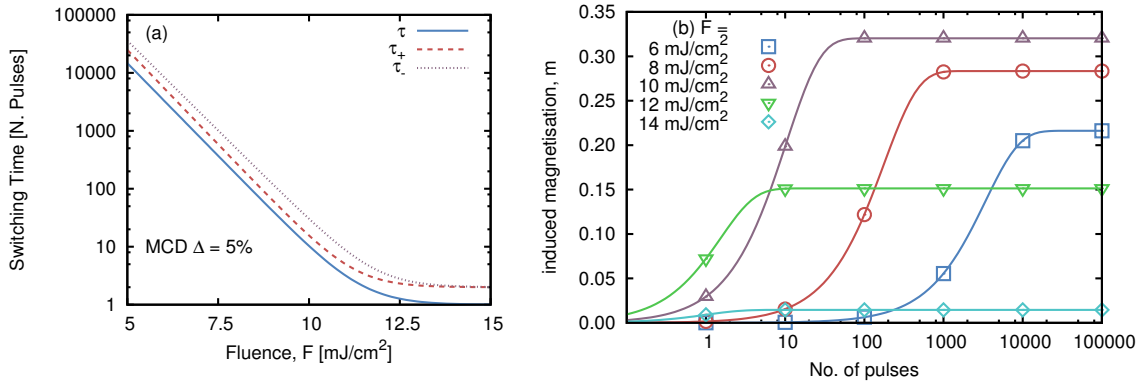


Figure 5.11.: (a) The switching times; $\tau$, $\tau_+$ and $\tau_-$ as a function of fluence with a MCD of 5% expressed as number of laser pulses. $\tau$ is independent of the MCD ratio and drops rapidly with fluence. (b) The induced magnetisation with the number of laser pulses for different fluences. At low fluence the switching time is large and so many laser pulses are required to reach the final induced magnetisation. At higher fluences the induced magnetisation saturates within a few pulses but since thermal effects are higher the induced magnetisation is lower.

transition times are very large and unlikely to lead to a induced magnetisation on a typical experimental timescale. As the fluence increases the transition times decrease rapidly so that only a few laser pulses are needed to reach equilibrium. The magnetisation switching time does not depend on the MCD ratio but for $\tau_\pm$ a larger MCD ratio widens the difference between the two times. Figure 5.11.(b) shows the time evolution of the induced magnetisation with a MCD $\Delta = 5\%$ for a number of fluences. As shown in (a) the low fluences take a large number of laser pulses to reach the equilibrium value. However whilst high fluences saturate quickly the value of $m^\infty$ is smaller.

The magnetisation induced by the MCD is shown in figure 5.12.(a) for a range of MCD. The solid lines show the induced magnetisation after 100 laser pulses and the dashed lines after 10,000. Whilst this simple model is unlikely to give quantitive results it does show that even a small MCD will give rise to a measurable induced magnetisation over a series of laser pulses. The maximum induced magnetisation is close to where the steepest gradient of the switching probability but due to the thermal randomisation at high fluences it is not centred on the steepest part. The induced magnetisation in figure 5.12 is defined as in the orientation of the low absorption state and since the values are positive this implies that the system will move towards the low absorption orientation. Khorsand *et al.* measure a MCD of 1.5% for GdFeCo and also demonstrate that it can be increased by tailoring the

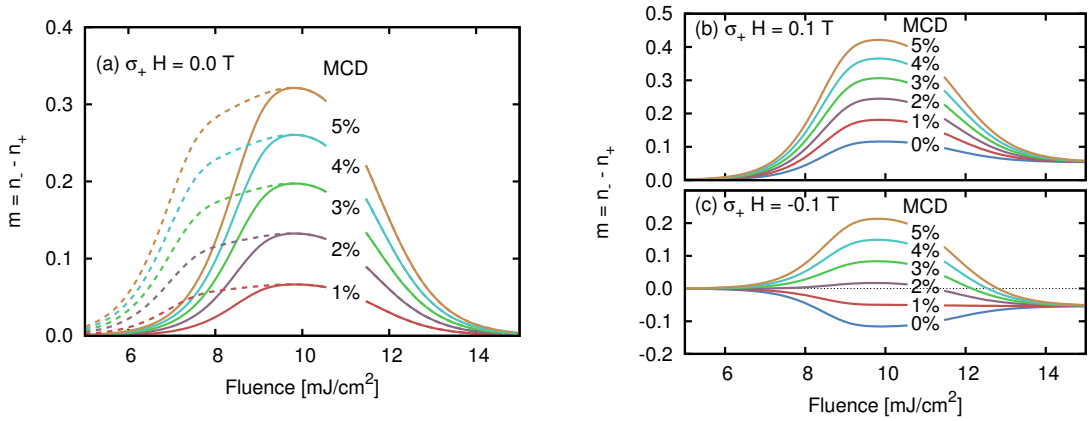


Figure 5.12.: Induced magnetisation after 100 laser pulses (solid lines) and 10,000 laser pulses (dashed lines). (a) shows the case where the field is oriented in the direction of the low absorption state while (b) shows it in the direction of the high absorption state. The field is incorporated through a linear interpolation of the switching probability parameters.

structure of the multilayer sample increasing up to 3%. The MCD ratio can be estimated from the polar Kerr rotation which using the measurements of Sato *et al.*[94] would give $\Delta \approx 0.85\%$ for a 800 nm wavelength. This value would predict an induced magnetisation of only $m \approx 0.05$ which is smaller than that observed experimentally. Whilst this may be due to the simplicity of the model used here, the MCD ratio may well be higher depending on film structure.

The effect of an applied field is to bias the thermal switching as shown in figure 5.10. The experiments show that a 700 Oe field can counter the all-optical switching. Using a linear interpolation of the fitting parameters given earlier the effect of a 0.1T field is considered. In order to compare to the experiments we now consider that the polarisation vector for right circularised light is $-\hat{\mathbf{z}}$ and that grains with their magnetisation in this direction absorbs more energy. The effect of the field is shown in figure 5.12.(b) and (c) for the field parallel and anti-parallel to the polarisation vector respectively. As (b) shows the field and the MCD switching cooperate so the field increases the induced magnetisation. In (c) the field counteracts the effect of the MCD switching, reducing the induced magnetisation. For this case the field reduces the induced magnetisation to approximately 0 for for an MCD of $\approx 1.7\%$. Earlier the MCD in FePt was estimated at $\Delta \approx 0.85\%$, despite the factor of 2 difference this does give an indication that the model describes the effects well. This agrees with the experimental results, showing that a small field can eliminate the effects of the thermal MCD switching.

## 5.7 CONCLUSION

The required parameter space for switching in FePt by a field generated through the inverse Faraday effect has been investigated using an atomistic model. To cause almost deterministic switching any field created would need to be either upwards of 30 T or have a duration of nearly a picosecond. Such a field may be physically unreasonable but may be possible if driven by the exchange field which can be larger still. Higher fluences access the linear reversal regime but higher thermal noise causes the switching to become more or less random with only a slight bias towards the field.

A further explanation of the experiment results of Lambert *et al.* is using magnetic circular dichroism. Due to the helicity of the light the different magnetisation orientation leads to a difference in the energy absorbed from the laser. The probability of a grain changing orientation was calculated showing that there is a clear dependence on the final state on the laser fluence. Using a simple model based on a two-state Master equation the induced magnetisation due to the MCD was found to agree qualitatively well with the magnetisation found in the experiments. Whilst this supports the picture that the differential absorption leads to a net magnetisation a more detailed model incorporating the effects of surrounding grains on the switching probability would allow for a quantitive evaluation of the MCD. Within this approach an MCD of 3% would explain what is observed experimentally. Estimates for the MCD in $L1_0$ FePt would indicate $\Delta \approx 0.85\%$, which would predict a smaller induced magnetisation but is close to the MCD value which counters the induced switching in a field. This may be due to the simplicity of the model or the actual MCD ratio of the FePt samples used by Lambert *et al.* is larger. It may also indicate that whilst the IFE does not cause switching it may enhance the induced magnetisation when combined with this MCD model of the switching.

# 6

# COUPLED SPIN-LATTICE DYNAMICS IN FE

So far the atomistic spin model introduced in Chapter 2 has been used to model the magnetic properties of granular media. The energy transfer channels have been simulated phenomenologically using Langevin dynamics and the two temperature model. Here an advanced approach is employed to incorporate the lattice dynamics alongside the spin dynamics to provide a coupling mechanism between the two subsystems. First the motivation for development of such a model is discussed before describing the details and testing of the model. The model is then used to calculate the magnon and phonon dispersion relation for both infinite and thin film structures. The inclusion of an anisotropic coupling term is discussed showing that strong spin-lattice coupling can excite magnons at the Brillouin zone boundary before they decay to the gamma point.

## 6.1 INTRODUCTION

Typical atomistic dynamics includes thermal effects and damping through phenomenological terms as described in Chapter 2. It is assumed that the spin system transfers energy and angular momentum to and from the electronic and lattice systems. Whilst the underlying mechanisms for these processes are highly complex the phenomenological treatment allows the effects to be introduced into the spin dynamics easily. The coupling of the spin system to the lattice can be done in a more exact way by considering the dynamics of the lattice alongside the spin dynamics. In this way the dynamical lattice will act as a thermal reservoir for the spin system and provides a channel for energy to dissipate out of the spin system.

The development of molecular dynamics (MD) and spin dynamics (SD) as computational tools have allowed for detailed investigation of the microscopic dynamics of condensed matter systems. Interest in coupling spin and molecular dynamics has expanded in recent years. Several groups have developed such models to investi-

gate a variety of dynamical effects where the coupling is important. It was shown by Karakurt *et al.*[95], using a first order coupling term, that the interaction of the spins and lattice can induce a magnetic damping effect which arises from finite boundaries. However, the physics of such a coupling term is not clear as it results in a net acceleration on the lattice.

Further developments have been made extensively by Ma *et al.*[27], who incorporated advanced magnetic inter-atomic potentials and *ab-initio* calculations to model bcc iron. Ma *et al.* have also shown that by coupling the instantaneous temperatures of the spin and lattice systems to the three temperature model[73] the electron temperature can be effectively simulated[84]. In the work by Ma *et al.* the only energy transfer channel between the spins and lattice is through the dependence of the exchange on the distance between atoms. This does not allow for transfer of angular momentum and so another coupling term is highlighted by Beaujouan *et al.*[96] Later in this chapter this coupling term is employed to to demonstrate the utilisation of the lattice as a thermal reservoir and that magnons can be excited without direct thermal noise.

In the context of heat assisted magnetic recording the simulation of the lattice dynamics in FePt would provide valuable insights. However due to the nature of the polarised Pt moments any motion by the Fe moments would cause a fluctuation of the Pt moment beyond the derivation of the Hamiltonian derived in Ch 2. This would require longitudinal spin fluctuations[97] to be incorporated which would increase the complexity of the model. Here a more simplified approach is taken to focus on the dynamic effects of the coupling of the spins to the lattice and so a simple model for bcc Fe, which is well parametrised in the literature, is utilised.

## 6.2 MODEL DETAILS

To model the coupled spin and lattice system the starting point is the Hamiltonian containing contributions from all the degrees of freedom.

$$\begin{aligned}\mathcal{H}\left(\mathbf{r},\mathbf{v},\mathbf{S}\right) = &-\sum_{i,j} J(\mathbf{r}_i-\mathbf{r}_j)\,\mathbf{S}_i\cdot\mathbf{S}_j - \mu_s\sum_i \mathbf{S}_i\cdot\mathbf{H}_{\text{app}} \\ &+\sum_i \frac{m_i\mathbf{v}_i^2}{2} + \frac{1}{2}\sum_{i,j} U(|\mathbf{r}_i-\mathbf{r}_j|)\end{aligned} \tag{6.1}$$

| | | bcc Fe | Unit |
|---|---|---|---|
| Morse Potential[98] | D | 0.4174 | eV |
| | $\alpha$ | 1.3885 | Å |
| | $r_0$ | 2.845 | Å |
| Exchange[27] | $J_0$ | 0.90490177 | eV |
| | $r_c$ | 3.75 | Å |
| System[5, 102] | $\mu_s$ | 2.22 | $\mu_B$ |
| | m | 55.845 | u |
| | a | 2.8635 | Å |

Table 6.1.: Parameters for the Morse potential, exchange interaction and other system constants used for bcc Fe. References are given for where the parameters are taken from.

The first two terms form the magnetic Hamiltonian which drives the spin dynamics. The third term is the kinetic energy of the lattice and the final term is the lattice inter-atomic potential energy, which is written here as a pairwise interaction. $\mu_s$ and $m_i$ are the saturation magnetic moment and atomic mass which are system constants, the values are given in table 6.1. The potential used here for bcc Fe is the Morse potential[98], described by:

$$U(r_{ij}) = D\left[e^{-2\alpha_0(r_{ij}-r_0)} - 2e^{-\alpha_0(r_{ij}-r_0)}\right] \tag{6.2}$$

This potential incorporates attractive and repulsive parts, which is quadratic close to the energy minimum but with added anharmonicity further away. D and $r_0$ represent the depth and position of the energy minimum and $\alpha_0$ controls the width, these parameters are given in table 6.1. These parameters give a lattice constant $a_0 = 2.8635$ Å[98] which is close to the experimental $a_{\text{exp}} = 2.870$ Å[99, 100]. More accurate inter-atomic potentials for metals utilise many body effects, in particular Derlet and Dudarev[101] derived a many body inter-atomic potential for Fe that incorporates magnetic effects. These potentials greatly increase the accuracy of the lattice properties but here the focus is on the magnetic properties of the system and so the Morse potential should be suitable.

Since the atoms will not remain in their equilibrium positions the exchange interaction must depend on the separation of the atoms and therefore provides the simplest coupling term between the spins and lattice. In principle, how the exchange varies with atomic separation is highly complex; especially for metals like Fe where long range exchange interactions like RKKY exchange may occur[37]. The form of

the exchange used here is given by Ma *et al.*[27] for ferromagnetic bcc Fe. This is an isotropic exchange interaction that only depends on the magnitude of the atomic separation and has no directional dependence.

$$J(r_{ij}) = \begin{cases} J_0 \left(1 - \frac{r_{ij}}{r_c}\right)^3 & r_{ij} < r_c \\ 0 & r_{ij} > r_c \end{cases} \tag{6.3}$$

The equations of motion for the coupled system combine the Landau-Lifshitz-Gilbert (LLG) equation with Newton's equations for the lattice.

$$\frac{\partial \mathbf{r}_i}{\partial t} = \mathbf{v}_i \tag{6.4}$$

$$\frac{\partial \mathbf{v}_i}{\partial t} = \frac{\mathbf{F}_i}{m_i} \tag{6.5}$$

$$\frac{\partial \mathbf{S}_i}{\partial t} = -\frac{\gamma}{(1+\lambda^2)\mu_s} \mathbf{S}_i \times (\mathbf{H}_i + \lambda \mathbf{S}_i \times \mathbf{H}_i) \tag{6.6}$$

The spin damping, $\lambda$, is included here for clarity but for conservative dynamics this can be removed by using $\lambda = 0$. The $\mathbf{F}$ and $\mathbf{H}$ are the local force and effective field respectively and are given by:

$$\mathbf{H}_i = -\frac{\partial \mathcal{H}}{\partial \mathbf{S}_i} \tag{6.7}$$

$$\mathbf{F}_i = -\frac{\partial \mathcal{H}}{\partial \mathbf{r}_i} \tag{6.8}$$

Since this system now contains 3 sub-systems that each interact the numerical simulation requires careful treatment. Both Ma *et al.* and Beaujouan *et al.* use a Suzuki-Trotter decomposition method[103] to integrate the coupled equations of motion. This method is a symplectic integrator which has been used for spin liquids[104, 105] and has been shown to be accurate with larger time steps than other integration techniques[106]. To begin with the state vector of the system which combines the lattice and spin degrees of freedom is given by:

$$\mathbf{X}(t) = \begin{pmatrix} \{\mathbf{r}_i(t)\} \\ \{\mathbf{v}_i(t)\} \\ \{\mathbf{S}_i(t)\} \end{pmatrix} \tag{6.9}$$

Using this notation the coupled differential equations are written in Liouville form where the Liouville operator is the sum of the operators for each sub-system. The

position, velocity and spin Liouville operators themselves are the equations of motion for the position, velocity and spin given earlier.

$$\frac{\partial \mathbf{X}}{\partial t} = \hat{L}\mathbf{X}(t) = \left(\hat{L}_r + \hat{L}_v + \hat{L}_s\right)\mathbf{X}(t) \tag{6.10}$$

$$\hat{L}_r = \sum_i \mathbf{v}_i \cdot \frac{\partial}{\partial \mathbf{r}_i} \tag{6.11}$$

$$\hat{L}_v = \sum_i \frac{\mathbf{F}_i}{m_i} \cdot \frac{\partial}{\partial \mathbf{v}_i} \tag{6.12}$$

$$\hat{L}_s = \sum_i (\mathbf{a}_i \times \mathbf{S}_i) \cdot \frac{\partial}{\partial \mathbf{S}_i} \tag{6.13}$$

Where the axial vector $\mathbf{A}_i$ in the spin Liouville operator is equivalent to the cross product drift function presented in Chapter 2:

$$\mathbf{a}_i = \frac{\gamma}{(1+\lambda^2)\mu_s}\left(\mathbf{H}_i + \lambda \mathbf{S}_i \times \mathbf{H}_i\right) \tag{6.14}$$

Despite the complicated nature of the Liouville operators the formal general solution is the exponential update. Due to the complexity the exponential cannot be evaluated directly but instead the Suzuki-Trotter decomposition approximates this as the exponential update for each separate Liouville operator as the following

$$\mathbf{X}(t+\Delta t) = e^{\left(\hat{L}_r + \hat{L}_v + \hat{L}_s\right)\Delta t}\mathbf{X}(t) \tag{6.15}$$

$$= e^{\hat{L}_v \Delta t/2} e^{\hat{L}_r \Delta t/2} e^{\hat{L}_s \Delta t} e^{\hat{L}_r \Delta t/2} e^{\hat{L}_v \Delta t/2}\mathbf{X}(t) + \mathcal{O}(\Delta t^3) \tag{6.16}$$

These exponentials are algorithmic functions that update the extend variable; these updates are given below. For the position and velocity they follow a simple first order update but for the spins the Cayley transform is applied which is a norm conserving rotation about the given axial vector.

$$e^{\hat{L}_v \Delta t}\mathbf{v}_i = \mathbf{v}_i + \frac{\Delta t}{m_i}\mathbf{F}_i \tag{6.17}$$

$$e^{\hat{L}_r \Delta t}\mathbf{r}_i = \mathbf{r}_i + \Delta t \mathbf{v}_i \tag{6.18}$$

$$e^{\hat{L}_s \Delta t}\mathbf{S}_i = \frac{\mathbf{S}_i + \Delta t \mathbf{a}_i \times \mathbf{S}_i + \frac{\Delta t^2}{2}\left((\mathbf{a}_i \cdot \mathbf{S}_i)\mathbf{a}_i - \frac{1}{2}a_i^2 \mathbf{S}_i\right)}{1 + \frac{1}{4}\Delta t^2 a_i^2} \tag{6.19}$$

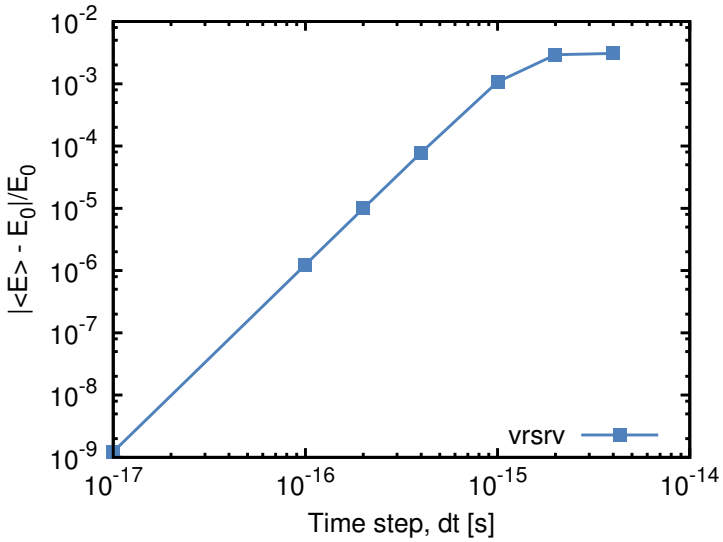


Figure 6.1.: The mean error in the total energy for different time steps calculated at 10K in an applied field of 10 T. The update order is vrsrv, with the semi-implicit scheme used for the spin update.

Without the spins the position and velocity updates are then identifiable as the velocity ( or position) Verlet integration scheme; where the velocity and position are updated in an alternating manner with a half timestep between them. For the coupled system the order of updates shown in equation 6.16 is just one possibility and the subscripts can be re-ordered to give the same approximation. To simplify the notation the order that the updates are performed in is described by the subscript of each of the Liouville operators; i.e $e^{\hat{L}_v \Delta t}$ is given as v. Therefore the update specified in equation 6.16 is noted as vrsrv. After each update the forces and fields need updating depending on the new system state, therefore the ordering of the operators can affect the computational cost for each time step. Whilst the other updates allow for a minimisation in the computation of the forces[27], the vrsrv allows the spin update to be replaced with the semi-implicit scheme which is also uses the Cayley transform. Since the semi-implicit scheme uses a predictor step this improves the accuracy of the spin update which is the critical update of the system. Since the spin time scale is shorter than the positions and velocities the vrsrv also allow for the spin update to be repeated multiple times before the positions are re-updated[107]. Whilst this has not been implemented in this work it represents a useful addition for later development.

The integration scheme is tested by measuring the total energy, which since there is no dissipative effects should remain constant. The system is initialised with the velocities in random directions with a magnitude given by $v_{\text{therm}} = \sqrt{(}6k_BT/m)$

and the spins are aligned in the z direction. The initial temperature is set at 10 K and a 10 T field is applied to the spins. Figure 6.1 shows the relative error in the mean total energy calculated for different time steps. As the time step reaches 1 fs the error becomes significant; this arises from the spin integration since the spins begin to damp towards the field even without the damping term ($\lambda = 0$). The natural timescale of the atomic motion is slower than that of the spin precession and so it is this that limits the integration scheme. As observed in figure 6.1 the error for a time step of 0.1 fs is small and the time step is not too small to be computationally inefficient. This time step is used throughout unless otherwise mentioned.

Consistent with the atomistic spin dynamics, the system is kept at a constant temperature through the Langevin thermostat. Conventional molecular dynamics incorporate a thermal noise and damping terms into the velocities, here this is extended to incorporate thermal noise and damping in the spin system as well. Since the sub-systems are coupled a single thermostat would be possible. If the only the velocities are thermostatted this would allow the lattice to act as a thermal reservoir for the spins. However in practice the whole system is kept at an equilibrium temperature more efficiently when both the spins and velocities are thermostatted. In this case the fields and spins are altered as follows

$$\mathbf{H}_i = -\frac{\partial \mathcal{H}}{\partial \mathbf{S}_i} + \boldsymbol{\xi}_i \tag{6.20}$$

$$\mathbf{F}_i = -\frac{\partial \mathcal{H}}{\partial \mathbf{r}_i} - \eta m_i \mathbf{v}_i + \boldsymbol{\Gamma}_i \tag{6.21}$$

where $\boldsymbol{\xi}_i$ and $\boldsymbol{\Gamma}_i$ are the fluctuating thermal fields acting on the spins and velocities respectively. The dissipation in the lattice is controlled by the friction, $\eta$, which has units of $s^{-1}$. The strength of the fluctuation term for the lattice can be found by converting the stochastic differential equations into a Fokker-Planck equation for which a stationary solution can be found. The solution results in the following moments of the Gaussian noise[27].

$$\langle \Gamma_{i\alpha}(t) \rangle = \langle \xi_{i\alpha}(t) \rangle = 0 \tag{6.22}$$

$$\langle \Gamma_{i\alpha}(t) \Gamma_{j\beta}(t') \rangle = \frac{2\eta k_B T}{m_i} \delta_{ij} \delta_{\alpha\beta} \delta(t - t') \tag{6.23}$$

$$\langle \xi_{i\alpha}(t) \xi_{j\beta}(t') \rangle = \frac{2\lambda \mu_s k_B T}{\gamma} \delta_{ij} \delta_{\alpha\beta} \delta(t - t') \tag{6.24}$$

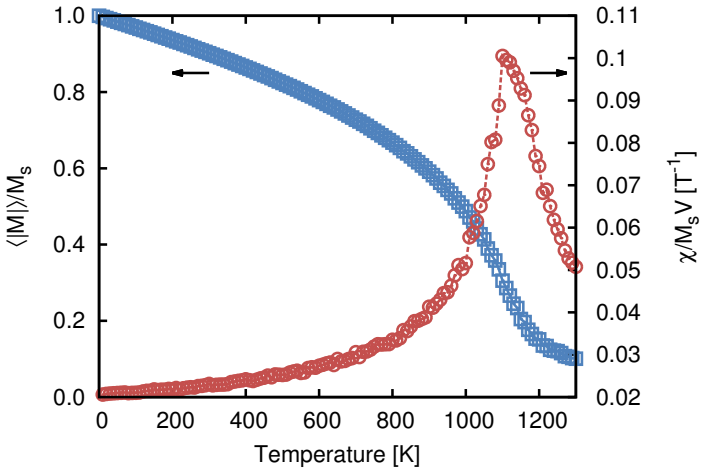


Figure 6.2.: The temperature dependence of the magnetisation and susceptibility showing the Curie temperature is $T_C \approx 1100$K.

where $i, j$ are atoms numbers, $\alpha, \beta = x, y, z$. Despite the coupling the variance of the thermal noise does not change from the separate spin or molecular dynamics.

## 6.3 EQUILIBRIUM PROPERTIES

Now that the model has been detailed we begin by investigating the equilibrium properties of the coupled system. First the equilibrium magnetisation and susceptibility are calculated using the thermal noise term for both the spin and lattice systems which is shown in figure 6.2. The damping terms are set to be $\lambda = 1.0$ and $\eta = 0.6\text{ps}^{-1}$ which brings the system in thermal equilibrium. Both the magnetisation and susceptibility show $T_C \approx 1050$ K which agrees well with the values calculated by Ma *et al.*[27] and Körman *et al.*[108] In this case because both the spin and lattice damping are high the system stays close to equilibrium. The atoms are close to their equilibrium positions and so the exchange does not vary much from the values if the atoms were fixed at the lattice sites.

We now move on to calculate the magnon and phonon dispersion relations at equilibrium in a bulk system. These excitations are created at finite temperature through the thermal noise term but since damping terms are incorporated into the equations of motion they will dissipate. Therefore to calculate the dispersions the temperature is set at 10 K and the damping constants are set low to $\lambda = 0.01$ and $\eta = 0.01\text{ps}^{-1}$ so the excitations will exist over a longer timescale. The phonon dispersion were calculated using the velocity auto-correlation function and

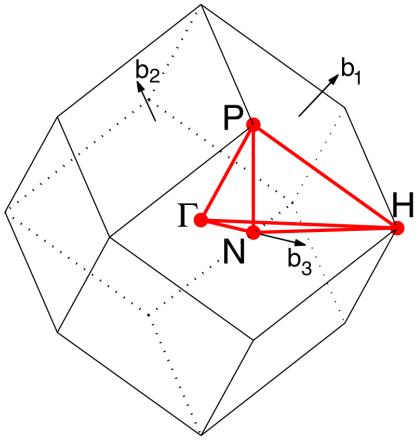


Figure 6.3.: Schematic of the bcc Brillouin zone, adapted from reference 111. The path taken is N-Γ-H-P-Γ.

is shown in figure 6.4. The velocity auto-correlation function in Fourier space is defined[109, 110] as:

$$A^p(\mathbf{k},\omega) = \int_0^T \langle v^p_{\mathbf{k}}(0) v^p_{\mathbf{k}}(t)\rangle e^{-i\omega t} dt \tag{6.25}$$

where $p = x, y, z$ and $v^p_{\mathbf{k}}(t)$ is the spatial Fourier transform of the velocities and $T$ is the total time over which the sampling is taking place which sets the minimum frequency that is observable. The evaluation of the spatial Fourier transform cannot be undertaken using a fast Fourier transform as the positions do not lie on an exact discrete grid. Therefore it is calculated using a sum over the atoms in the system.

$$v^p_{\mathbf{k}}(t) = \sum_i v^p_i e^{-i\mathbf{k}\cdot\mathbf{r}_i} \tag{6.26}$$

This sum is performed over a discrete set of k vectors. The symmetry directions in the bcc Brillouin zone are shown in figure 6.3; the path taken through the Brillouin zone is N-Γ-H-P-Γ with the k vector discretisation given by $dk = 2\pi/L$ where L is the size of the system.

The peaks of the velocity auto-correlation function are shown in figure 6.4 for a system of 32x32x32 unit cells. The calculated phonon dispersion is compared to experimental values of Minkiewicz *et al.*[112] The calculated values agree with the experimental values for some k vectors and show some of the key features but otherwise does not match. The agreement at low k vectors may arise from small amplitude oscillations around the equilibrium positions where the Morse potential

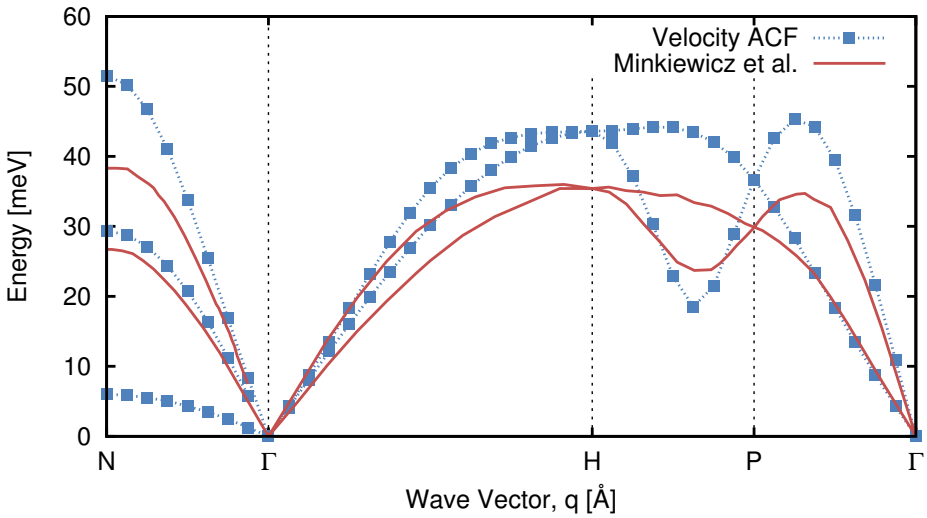


Figure 6.4.: The peaks in the velocity autocorrelation function showing the phonon distribution calculated at 10K with $\eta = 0.6\,\mathrm{ps}^{-1}$. Experimental results of Minkiewicz *et al.*[112] are shown as solid lines for comparison.

will behave quadratically. Despite the difference the energy scale is correct which is important for the simple approach here.

The magnon dispersion can be calculated using the dynamical spin structure factor[75, 113]

$$\mathcal{S}^{\alpha\beta}(\mathbf{k},\omega) = \sum_{\mathbf{r},\mathbf{r}'} e^{i\mathbf{k}\cdot(\mathbf{r}-\mathbf{r}')} \int e^{i\omega t} C^{\alpha\beta}(\mathbf{r}-\mathbf{r}',t)dt \tag{6.27}$$

The equal time spin-spin correlation function is defined as

$$C^{\alpha\beta}(\mathbf{r}-\mathbf{r}',t) = \langle S^{\alpha}(\mathbf{r},t)S^{\beta}(\mathbf{r}',0)\rangle - \langle S^{\alpha}(\mathbf{r},t)\rangle\langle S^{\beta}(\mathbf{r}',0)\rangle \tag{6.28}$$

Its calculation is detailed in Ref. 75 but relies on the translational invariance of the system and uses a fast Fourier transform. Therefore the approach used above for the velocity auto-correlation function is applied to the spins as well, which is similar to the manner employed in Refs. 114 and 115. The magnon dispersion is shown in figure 6.5 at 10K using a low damping of $\lambda = 0.01$. The solid lines show the phonon dispersion from figure 6.4 which is at as much lower energy (frequency) than the ferromagnetic magnon branch. Since there is a large difference in the energy scales there will be little coupling between the modes at high k vectors. At low k vectors the behaviour of the magnons and phonons are different; from linear spin wave theory the magnon energies will be $\propto k^2$ whilst the phonons will be $\propto k$ indicating

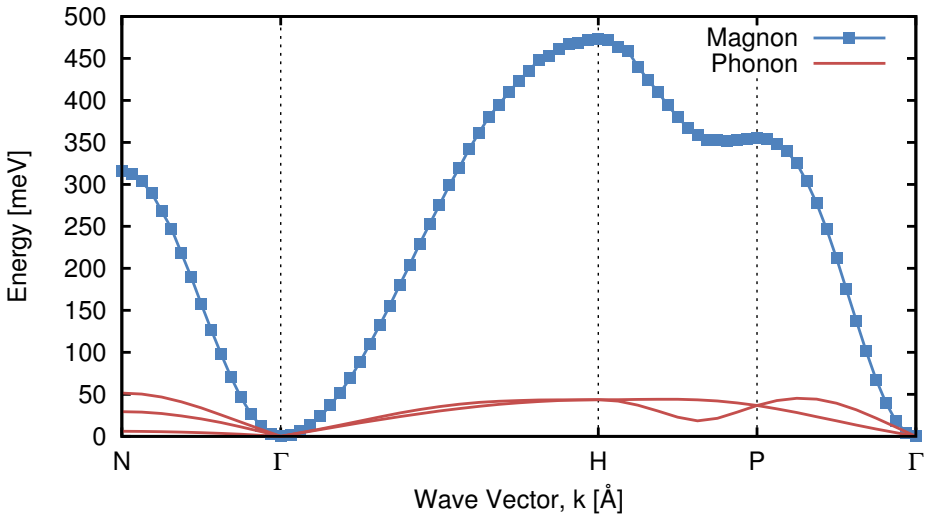


Figure 6.5.: The magnon dispersion at T=10K with $\lambda = 0.01$. The solid red lines show the phonon dispersion which occurs at much lower energies than the phonon.

that they will cross. Figure 6.6 shows the region close to Gamma point from figure 6.5. Here the magnon and phonon bands cross and have similar energies which may allow for exchange of energy between them. Since they are at low k vectors a much larger system would be required to observe any detailed effects of the dispersions which becomes computationally difficult.

## 6.4 INDUCED SPIN DAMPING DUE TO LATTICE COUPLING

The coupling of the spins to the lattice is a dominant effect in the dissipation of energy from the spin system. To dissipate energy from the spin system angular momentum needs to be transferred to the lattice. Control of the damping in a material can be important for future recording devices since high damping materials will switch faster with an applied field. Generally the damping relates strongly to the spin-orbit coupling so materials with rare earth elements can be engineered to have high damping[82]. The distance dependence of the exchange is meant to form a coupling between the spin and lattice systems. However since the exchange interaction is isotropic and pairwise there is no net effect on the magnetisation dynamics. This can be seen by considering the spin equation of motion without damping for a pair of spins. The equation of motion for the magnetisation $\partial \mathbf{M}/\partial t = \mathbf{S}_i \times J_{ij}\mathbf{S}_j + \mathbf{S}_j \times J_{ji}\mathbf{S}_i$. Since $J_{ij} = J_{ji}$ the terms will cancel and the magnetisation is conserved. Therefore a separate coupling term is included into the Hamiltonian

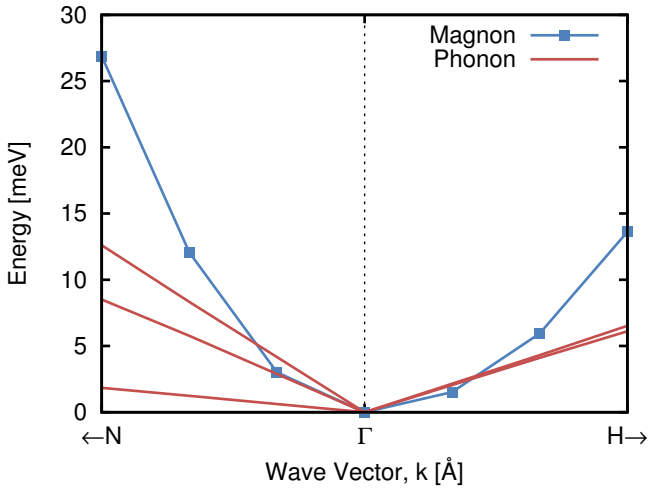


Figure 6.6.: The small k vector region of figure 6.5. At small k vectors the magnon dispersion follows $\propto k^2$ while the phonon dispersion follows $\propto k$.

for which the spins and lattice can transfer energy and angular momentum. This term is introduced by Beaujouan *et al.*[96] and as described by other literature[116] as arising from the spin-orbit interaction.

$$\mathcal{H}_c = -\sum_{i,j} K(r_{ij}) \left( (\mathbf{S}_i \cdot \hat{\mathbf{r}}_{ij})(\mathbf{S}_j \cdot \hat{\mathbf{r}}_{ij}) - \frac{1}{3}\mathbf{S}_i \cdot \mathbf{S}_j \right) \tag{6.29}$$

Since this term has the same form as the dipole interaction term (equation 2.27) it is termed the "pseudo-dipole" coupling term. The difference arises in the pre-factor, $K(r_{ij})$; in the dipole interaction it decays slowly as $1/r^3$ whereas the pseudo-dipole coupling term should decay very sharply with separation in a similar manner to the exchange. In this case to simplify the model the pre-factor is assumed to take the same form as for the exchange but scaled, thus $K(r_{ij}) = (K_0/J0)J(r_{ij})$.

To investigate the effect of the coupling term the magnetisation dynamics in a field is calculated for different values of $K_0$. A small damping, $\lambda = 0.01$, is included so that the spins are in an thermalised state and so any change in the damping is clearly observable. Figure 6.7 shows $M_y(t)/|M(t)|$ as a function of time for $K_0 = 0$, 0.1 and 0.5 with a 10 T field in the y direction. The values are normalised by $|M(t)|$ as the different coupling changes the equilibrium magnetisation and each curve would reach a slightly different value. The magnetisation curves show a change in the damping, with the large coupling reducing the damping rate. The damping is extracted by fitting $m_y(t) = \tanh(\omega_p \lambda t)$ where $\omega_p$ is the precession time which is extracted from the x and z components. The extracted damping values are shown in the inset of figure 6.7 and a decrease in the damping is observed for strong coupling.

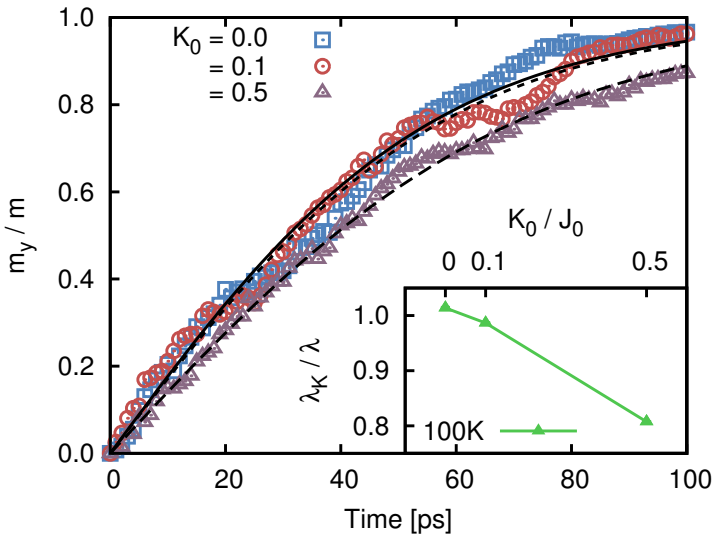


Figure 6.7.: Damping of the magnetisation towards the field direction for different coupling values. Lines show $m_y(t) = \tanh(\omega_p \lambda t)$ fitted to the data, the extracted damping is shown in the inset (normalised to the input damping).

This decrease is unexpected as the coupling to lattice is intended to transfer energy from the spin system to the lattice. This may arise from the direction in which the field due to the pseudo-dipolar interaction acts as it may, depending on the local position and spin structure, act in the opposite direction to the damping torque. The interaction also will be affecting the equilibrium state of the system, as it will act against the exchange interaction (c.f. the last term in equation 6.29) depending of the sign of $K_0$. At finite temperature the generation and scattering of spin waves plays a role in damping and so the damping will increase with temperature[117]; therefore the role of the pseudo-dipolar interaction may be to alter the underlying dynamics of the system which will require further investigation.

Figure 6.8 shows the magnon dispersion where there is no spin damping and a large coupling $K_0 = 0.5J_0$. Compared to figure 6.5 the same ferromagnetic branch has been excited; since there is no thermal noise this is caused by the coupling term. There is a low energy branch appearing which is on the scale of the phonon modes and is likely due to the method used to compute the structure factor but may be coupled modes.

The effect of the coupling term can be seen by comparing the relative distribution in the Brillouin zone. Figure 6.9 shows the values of the peaks for each k vector normalised to the value at the Γ point for the two cases. For the case without the coupling term but with thermal noise an equilibrium distribution is obtained

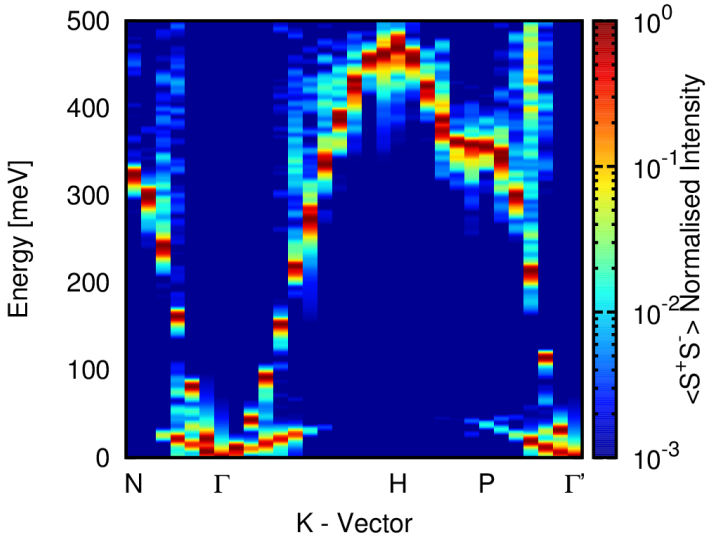


Figure 6.8.: The magnon dispersion without any thermal noise and the coupling term set with $K_0 = 0.5J_0$. The ferromagnetic bands are visible implying that the coupling term is exciting modes. Some low energy bands are also present which are likely to be the phonon modes that are visible due to the computational method.

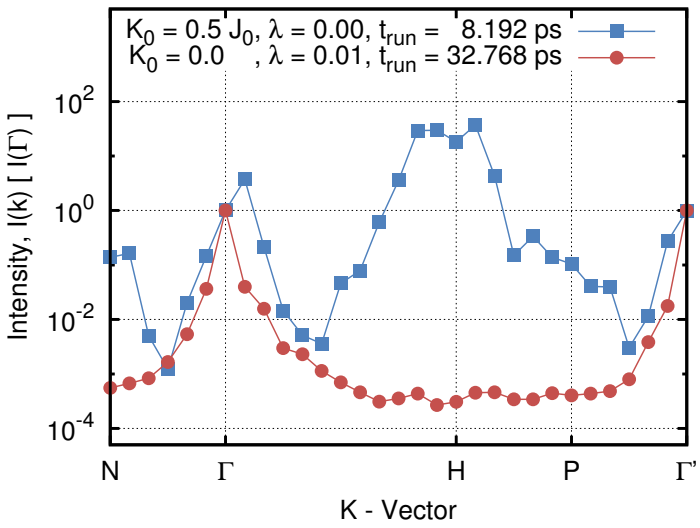


Figure 6.9.: The relative peak values of each the magnon dispersions where the values are normalised to the value at the Γ point. With out the coupling but with thermal noise (circles) the power is distributed close and primarily at the Γ point. Without the thermal noise but with the coupling term included (squares) the system is still out of equilibrium with most of the power at the edge of the Brillouin zone.

with the majority of power close to the Γ point. However for the case without thermal noise and the coupling term included the distribution is not in equilibrium, partially due to the limited run time, and the distribution is mostly at the edges of the Brillouin zone. Since the coupling term is short ranged this likely drives the magnon modes at the edge of the Brillouin zone. There appears to be some relaxation processes occurring as there is an similar amount of power in modes close to the Γ point so the coupling term is exciting modes at short wavelengths which then relaxing to longer wavelengths.

## 6.5 EFFECTS DUE TO FREE SURFACES

We now turn to the effects generated by creating a surface in the system. The surface spins have different local fields from first missing exchange interactions and second from a reconstruction of the surface compared to the bulk. Figure 6.10 shows the spin auto-correlation function calculated for a system with non-periodic boundaries in the z-direction. The solid black line shows the magnon dispersion for a bulk system from figure 6.5. Whilst the bulk ferromagnetic branch is still distinct it does vary around P and N. Both P and N are along $k_z$ and so the change represents a change in the exchange in this orientation. At P the surface modes are at a higher energy than the bulk mode which would imply a stronger exchange interaction. This may be possible if the surface reconstructs so the surface layer lies closer to the layer below it thus giving a larger exchange interaction. Figure 6.10 also shows low energy surface magnon modes that would appear to be at a similar energy to the phonon modes and thus more easily accessible for the transfer of energy.

The surface starts in the bulk equilibrium position but due to the finite boundaries it starts to relax. This triggers phonons travelling in the z direction, which with low friction can be long lived, causing a coherent oscillation of the magnetisation. Figure 6.11 shows how the magnetisation behaves in time at the beginning of the simulation. There is a clear oscillation in the magnitude of the magnetisation in comparison to the relaxation curve shown for bulk. By removing the demagnetisation part of the curve the oscillation can be fitted using

$$m_{\text{osc}}(t) = A\sin(\omega(t-t_0)e^{-t/\tau_d} + m_0 \tag{6.30}$$

with $A, \omega, t_0, \tau_d$ and $m_0$ as fitting parameters. The fitting is shown in the inset of figure 6.11. The fitted mode angular frequency is $\omega = 1.632 \pm 0.002\ \text{ps}^{-1}$ which corresponds to f = 0.259 THz or 1.074 meV. Such an effect is observed experimentally[118–

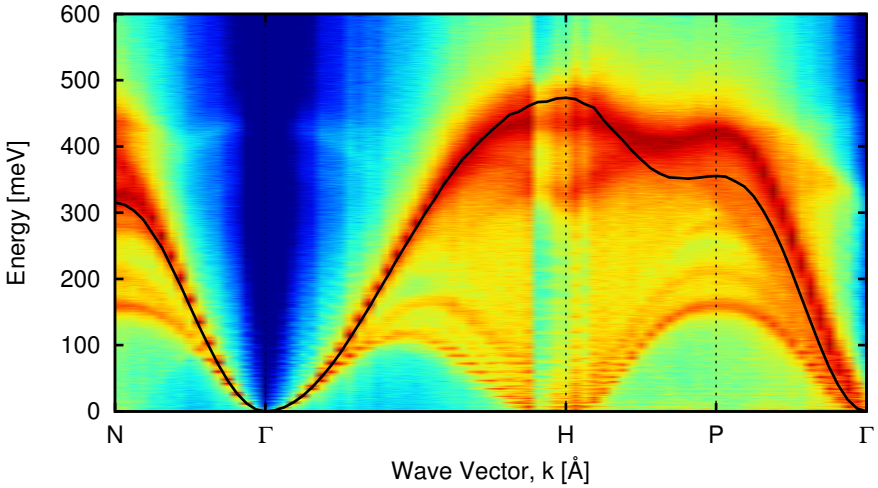


Figure 6.10.: Spin auto-correlation function calculated for a system with finite boundaries in the z direction. The solid line shows the magnon dispersion for a bulk system. There exists some surface modes due to the reconstruction of the surfaces.

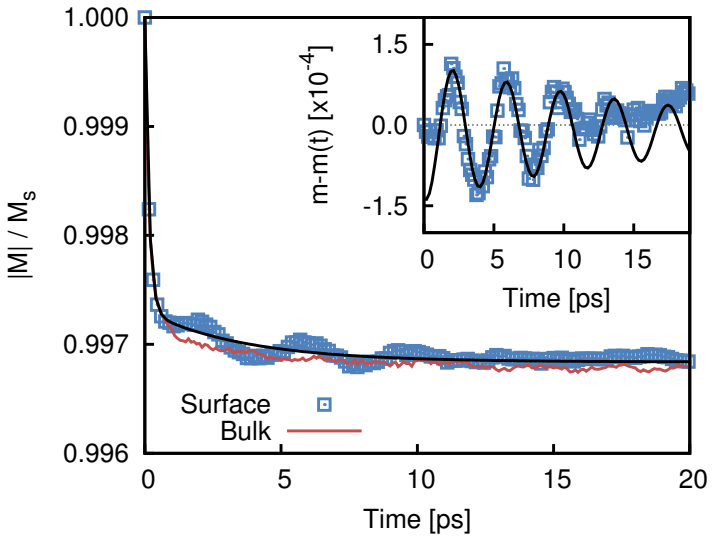


Figure 6.11.: The magnetisation shows oscillations attributed to phonons triggered by the finite surface. The solid red line shows the relaxation curve for a bulk system while the solid black line shows a fitted double exponential which characterises the longitudinal relaxation. The inset shows the longitudinal relaxation subtracted from the magnetisation to highlight the oscillations. The solid line in the inset shows $y(x) = A\sin(\omega(x - x_0))e^{-x/\tau_d} + y0$. The fitted frequency is $\omega = 1.632 \pm 0.002\text{ps}^{-1}$, corresponding to an energy of 1.074 meV.

120] in Gd thin films using femto-second laser pulses to excite the dynamics. In this case the oscillations are attributed to a coupled magnon-phonon mode that occurs at the surface that has a frequency of 2.9 THz, which is much larger than the frequency here. While this is a significant difference, in Gd the magnon frequencies are at a lower energy due to the weaker exchange interaction and the magnetic moment is much larger[5, 36] so the transfer of energy will happen at different points in the Brillouin zone. Experimentally the coupling occurs with the optical branches, thus at a higher energy. Here since the energy is much lower it would correspond to a acoustic branch. The crossing of the acoustic branches was shown in figure 6.6 which shows the magnon and phonon are at similar energies for the first k-vector considered. The magnetisation oscillation was not observed in simulations of N=16 unit cells, for which the first allowed k-vector would be the second point away from $\Gamma$ in figure 6.6 for which the energies are starting to separate. Studying the oscillation frequency over the temperature range T = 1 - 25 K shows little variation on this scale. Despite the differences between the coupled modes, the aim here was to demonstrate that these effects will occur through a dynamical exchange interaction in the simple model for Fe where as the potentials for Gd are less well known.

## 6.6 CONCLUSION

To summarise, a model of the coupled spin and lattice dynamics has been developed to explore the effect of the lattice acting as a heat bath. An example system of bcc Fe was modelled and was tested for first the energy conservation and the phonon dispersion. With thermal noise and damping incorporated on both the spin and lattice system the equilibrium magnetisation and susceptibility showed $T_C \approx 1050$ K. The phonon and magnon dispersion relations were calculated using the velocity auto-correlation function and dynamical structure factor respectively. The phonon dispersion showed similar energies and features to the experimental values given by Minkiewicz *et al.*[112] but do not match over the full range. The magnon dispersion shows a clear ferromagnetic branch which is at a much higher energy than the phonons. There is some crossing at low k due to the different behaviour of the excitations; a much larger system would be required to observe any coupling between the bands at these k vectors.

The range dependent exchange interaction does not provide a suitable coupling due to the symmetry of the equations of motion and so a specific coupling term is also included based on the spin-orbit coupling. The induced damping was measured from

the magnetisation dynamics in an applied field and showed that a strong coupling to the lattice reduces the damping slightly. With no spin damping, $\lambda = 0$, the coupling term excites magnons at the Brillouin zone boundary which decay to the Gamma point indicating that some relaxation processes are occurring. Whilst the coupling term is transferring energy between the sub-systems it requires a large value to induce any magnetisation change on a picosecond timescale. This would indicate that the lattice may not act as a sufficient thermal bath for spin dynamics simulations.

A thin film was considered for which the magnon dispersion showed a main ferromagnetic branch as well as surface modes. The surface modes occur at higher energies than the bulk modes for k-vectors with some $k_z$ component indicating that the surface relaxes to a shorter separation from the second layer. Alongside the relaxation of the surface, the magnetisation shows a coherent oscillation that arises from a dynamic change in the exchange interaction at a frequency of $\mathrm{f} = 0.259\,\mathrm{THz}$. Whilst at a different frequency the process agrees with that seen experimentally for Gd.

# 7

# CONCLUSION

This thesis has explored the paradigm of heat assisted magnetic recording in relation to the high density granular media required for further development of recording devices. In this chapter the main results and conclusions presented throughout this thesis are summarised and discussed. The final section concludes the chapter with a discussion of the future prospects for the research.

*Finite Size Effects On Linear Reversal In FePt*

In Chapter 2 a model for FePt was introduced based on *ab-initio* calculations which show that the Pt magnetic moments depend linearly on the exchange field from the neighbouring Fe atoms. This allows the Hamiltonian to be expressed in terms of only the Fe spins with mediated exchange and anisotropy parameters. Due mediation through the Pt they are both long ranged, extending for 5 unit cells (1.93 nm) before they can be suitably truncated. Therefore with the aim to develop magnetic recording devices with grain sizes of a few nm the finite size effects are very important.

These finite size effects have been investigated systematically using the atomistic spin model. Calculations of the equilibrium magnetisation show that the truncation of the exchange interaction at the surfaces significantly reduces the apparent Curie temperature. Using the constrained Monte-Carlo method the variation of the magnetisation with polar angle shows that the magnetisation varies less for smaller grains. Using Langevin dynamics the longitudinal and transverse susceptibilities have been calculated for the range of grain sizes. These have been fitted which allows for them to be used with the Landau-Lifshitz-Bloch model. By comparing the ratio of the susceptibilities the critical temperature for the linear reversal range drops for smaller grains and temperature range between this and the Curie temperature widens. This indicates that if the free energy model is valid for these grains

then the linear reversal regime will occur at small temperatures and exist over a larger temperature range.

Following this the reversal properties were directly simulated. The reversal paths show that the magnetisation does switch through a linear path in the temperature range indicated by the equilibrium susceptibilities. However in the smaller grains the ellipticity of the reversal path predicted from the free energy over-estimates in comparison with the simulation results. The mean first passage time was calculated and shows that the combination of reduced anisotropy and different switching mechanism means smaller grains reverse faster over the temperature range.

*Exchange In Granular Media*

After investigating the finite size effects in FePt grains, the inter-granular exchange coupling was investigated. In granular media understanding the interactions between grains is important for the stability of bits. The dipolar interactions tend to introduce errors into stored bits but the exchange interaction between grains will reinforce grain stability. The effective exchange between grains is assumed to arise from magnetic impurities in the inter-layer. These impurities form spin chains between the grains.

To model this a sample grain structure was simulated atomistically, comprising of a central grain surrounded by 6 grains, all hexagonal in shape. The non-magnetic atoms in the inter-layer are not simulated so the magnetic impurities only have a specified density which was varied. The exchange was extracted using a hybrid CMC-MC model, where the magnetisation of each grain was fixed and the inter-layer unconstrained following the usual MC method. The torque for the central grain was calculated with the surrounding grains fixed. By fitting the gradient of the torque with polar angle the effective inter-granular exchange was found.

The inter-granular exchange depends quite strongly on the density of magnetic atoms in the inter-layer. The atoms were set on an fcc lattice which has a percolation threshold of 19%. Since the grain separation is varied down to 0.5 nm the percolation threshold is not exact but the inter-granular exchange is negligible below this limit. The temperature dependence of the inter-granular exchange was found and is seen to exist up to the Curie temperature. In agreement with experimental results, the inter-granular exchange is found to decay exponentially with grain separation. This indicates that as the recording media reduces the grain size and thus the grain separation the inter-granular exchange will become more significant. The exponen-

tial dependence on distance also shows that any distribution in the grain separation when the mean separation is small will have a drastic effect on the inter-granular exchange. The inter-granular exchange is likely to be beneficial to the long term stability of data bits as it reinforces the grain orientation whilst since its temperature dependence shows that there is no coupling above the Curie temperature it will not inhibit any switching during the HAMR process.

*Ultrafast Switching In FePt*

Recent experimental and theoretical work has observed that the magnetisation in transition metal rare earth ferrimagnets can be switched using a femtosecond laser pulse. It was first observed using circularly polarised light but has recently been shown to occur in linearly polarised light, now known as thermally induced magnetisation switching. Theoretical efforts have shown that TIMS requires a antiferromagnetic exchange coupling between two sub-lattices with different magnetic moments. What was observed as helicity dependent all optical switching has now been explained as the magnetic circular dichroism linked to this underlying TIMS. It is therefore unexplained when helicity dependent all optical switching was observed in ferromagnetic FePt granular media. Using the atomistic model of FePt the all optical switching was investigated. Since the Pt sub-lattice is polarised and ferromagnetically coupled to the Fe sub-lattice TIMS is not expected to occur. The effect of the femtosecond laser is modelled using the two temperature model. These electron and phonon temperatures are distinct and the laser directly heats the electron temperature before thermalisation occurs into the phonons. The spins are coupled to the electron temperature through the Langevin dynamics.

The experimentally observed switching is first assumed to be driven by the presence of a field generated through the inverse Faraday effect (IFE). The magnitude and duration of the inverse Faraday field were varied to find the regime where switching occurs. The required field for FePt would need to be either $> 60\,\mathrm{T}$ or have a duration of 1 ps after the laser pulse. A duration of 500 fs would still require a field strength of $> 30\,\mathrm{T}$. Whilst the strength or duration of a field caused by the IFE is unknown the parameters required here are unlikely to occur.

An alternative explanation of the experimental results is through the thermal activation of grains. The probability of a grain switching without a field increases with fluence. The helicity dependent switching in different orientation of grains absorbs either or less energy from the polarised laser. A simple two state master

equation is then used to model the effect of a differential absorption of the laser heat on the final magnetisation of the system. Using the transition rates calculated from the atomistic model for different fluences the master equation predicts an induced magnetisation in the orientation of the low absorption state. Whilst the induced magnetisation is small it agrees well with the experiments for a magnetic circular dichroism of 3%. Experimentally it is also shown that an applied field of 700 Oe can stop the switching entirely. The effect of the applied field is incorporated into the Master equation model and shows that it will indeed limit the induced magnetisation when the applied field is against the low absorption orientation.

*Coupled Spin-Lattice Dynamics In Fe*

For magnetic reversal the damping plays an important role. If larger damping can be engineered then the switching characteristics can also be controlled. In the atomistic spin model described in chapter 2 the damping is included as a phenomenological term so here a model incorporating the lattice dynamics is simulated. The model utilises molecular dynamics to evolve the positions and velocities of the atoms alongside the spin dynamics. For simplicity bcc Fe is modelled as this has been simulated in the literature. In this simple model it is clear that the lattice will not induce any damping as the exchange interaction is isotropic. Therefore an anisotropic coupling term is introduced which represents the spin-orbit interaction. Using this term it is shown that angular momentum is transferred between the spins and lattice. By calculating the magnon dispersion a ferromagnetic branch is populated and through analysing the relative amplitudes it is shown that the magnons are being excited at the edge of the Brillouin zone and decay to reach the Gamma point. This implies that the coupling term is exciting and removing energy from the spin system.

## 7.1 FURTHER WORK

*Multi-Scale Modelling Of Granular Media*

The topic of multi-scale modelling is currently at the forefront of research; by coupling the length scales provided by *ab-initio* atomistic spin models and micromagnetics it is possible to simulate a large scale magnetic system or device from essentially first principles. In chapter 3 *ab-initio* parameters were used to investigate small grains of FePt for which the equilibrium magnetisation and susceptibilities

were computed for various grain sizes. By using these parameters, for which fitted functions have been calculated, it is possible to model these finite grains using the Landau-Lifshitz-Bloch model. The simulation of a granular recording media utilising these parameters would be able to investigate the stability of a full data bits (comprised of multiple grains) on a much longer timescale that is accessible in atomistic spin dynamics

Whilst it was concluded that the LLB model is applicable down to grain sizes of $\approx 3.5\,\text{nm}$ it would improve the accuracy of the modelling if a realistic free energy could be derived or calculated for finite size grains. There exists such techniques for calculating free energies from molecular dynamics and therefore it would be possible to translate these algorithms to atomistic spin models. A method known as Metadynamics uses biased steering to force a system out of a local energy minima, which can be used to model rare events such as magnetic reversal over high energy barriers. The resulting bias used to force the system is then directly relatable to the free energy of the system. A method such as this could be employed to extract the free energy in a finite system; which could then be entered into micro-magnetic models directly or a suitable functional form fitted.

The results of Ch. 4 could also be incorporated in to the micro-magnetic modelling using finite parameters to provide an almost complete model of granular media parametrised from an atomistic model. Again by incorporating the inter-granular exchange parameters into a micro-magnetic model it would be possible to investigate it's effects on a much longer time scale. This would allow for a detailed analysis of the effects of inter-granular exchange on the recording and long time stability of bits. In addition to this a more detailed investigation of inter-granular exchange utilising *ab-initio* modelling would provide a more realistic model of the magnetic impurity density and the exchange interaction between them which is important on the overall interaction.

*All Optical Switching In Granular Media*

From the simulations performed here it was concluded that the helicity dependent all optical switching in granular FePt arises from the different switching rates caused by the orientations absorbing different amounts of energy from the laser. A simple Master equation model was presented which provided a qualitative agreement with the experimental findings. This model could be developed further to provide a more accurate comparison to the experiments. The model does not account for any many-

body interactions that would occur in a real system. As a larger magnetisation is induced in the sample the increased dipole may act to reduce the switching rate. This however may only be a small effect as the magnetisation only switched after demagnetisation for which the dipole field would be very small.

*Coupled Spin-Lattice Dynamics*

The spin-lattice model presented represents only a prototype developed to initially investigate the effects caused by coupling the sub-systems. A further aim would be to develop a more advanced model that would allow for the investigation of the spin dynamics driven by coupling to a phonon thermal reservoir. The pseudo-dipolar coupling term has been shown to drive dynamics in the spin system but further work is required to understand the behaviour and limits of utilising this as a coupling to the heat bath. Further work must also be under taken to fully parameterise the exchange interaction. The pseudo-dipolar term is required as the exchange is isotropic; if an exchange interaction that has a more complicated dependence on the atomic structure was to be developed then a stronger coupling to the lattice may be possible. This is non-trivial however as the dependence of the exchange interaction on the local environment cannot be simply calculated.

# A

## CALCULATION OF THE SUSCEPTIBILITY FROM AVERAGES

This appendix details the derivation of how the susceptibility can be calculated from the atomistic spin simulations using the averages for $m$ and $m^2$. The susceptibility tensor is defined as

$$\chi_{\alpha\beta} = \frac{\partial M_\alpha}{\partial H_\beta}, \tag{A.1}$$

and the magnetisation is given by

$$M_\alpha = \frac{\partial \mathcal{F}}{\partial H_\alpha}. \tag{A.2}$$

To calculate these we first use the definition of the Helmholtz free energy,

$$\mathcal{F} = -k_B T \ln \mathcal{Z}, \tag{A.3}$$

where $\mathcal{Z}$ is the partition function that is calculated using.

$$\mathcal{Z} = \sum_\sigma \exp\left(-\frac{\mathcal{H}}{k_B T}\right). \tag{A.4}$$

In this expression the sum extends over all the possible system states, $\sigma$. To calculate this we utilise a Hamiltonian which is split into two parts; the underlying Hamiltonian $\mathcal{H}_0$ and the Zeeman term:

$$\mathcal{H} = \mathcal{H}_0 - \mu_s \sum_i \mathbf{S}_i \cdot \mathbf{H} \tag{A.5}$$

$\mathcal{H}_0$ contains all the other microscopic interactions that do not involve the applied field and thus no restrictions are made on this. Using these definitions to find the magnetisation we first take the derivative of the free energy with respect to the applied field

$$\frac{\partial \mathcal{F}}{\partial H_\alpha} = -k_B T \frac{\partial \ln \mathcal{Z}}{\partial H_\alpha} \tag{A.6}$$

$$= \frac{k_B T}{\mathcal{Z}} \frac{\partial \mathcal{Z}}{\partial H_\alpha} \tag{A.7}$$

We next calculate the derivative of the partition function, which is

$$\frac{\partial \mathcal{Z}}{\partial H_\alpha} = \frac{\partial}{\partial H_\alpha} \left[ \sum_\sigma \exp\left( -\frac{\mathcal{H}}{k_B T} \right) \right] \tag{A.8}$$

$$= \sum_\sigma \left( -\frac{1}{k_B T} \right) \exp\left( -\frac{\mathcal{H}}{k_B T} \right) \frac{\partial \mathcal{H}}{\partial H_\alpha} \tag{A.9}$$

Under the assumption that the applied field only appears in the Zeeman term the derivative of the Hamiltonian is

$$\frac{\partial \mathcal{H}}{\partial H_\alpha} = \frac{\partial \mathcal{H}_0}{\partial H_\alpha} - \mu_s \sum_i \frac{\partial}{\partial H_\alpha} \left( \mathbf{S}_i \cdot \mathbf{H} \right) \tag{A.10}$$

$$= -\mu_s \sum_i S_\alpha \tag{A.11}$$

By returning this to the derivative of the partition function we notice that the term on the right hand side is the definition of the ensemble average of the magnetisation.

$$\frac{\partial \mathcal{Z}}{\partial H_\alpha} = \frac{1}{k_B T} \sum_\sigma \left( \mu_s \sum_i S_{i\alpha} \right) \exp\left( -\frac{\mathcal{H}}{k_B T} \right) \tag{A.12}$$

$$= \frac{\mathcal{Z}}{k_B T} \langle M_\alpha \rangle \tag{A.13}$$

Returning to the susceptibility:

$$\chi_{\alpha\beta} = \frac{\partial M_\alpha}{\partial H_\beta} \tag{A.14}$$

$$= \frac{\partial}{\partial H_\beta} \frac{\partial \mathcal{F}}{\partial H_\alpha} \tag{A.15}$$

$$= \frac{\partial}{\partial H_\beta} \left( \frac{k_B T}{\mathcal{Z}} \frac{\partial \mathcal{Z}}{\partial H_\alpha} \right) \tag{A.16}$$

$$= k_B T \left( \frac{1}{\mathcal{Z}} \frac{\partial^2 \mathcal{Z}}{\partial H_\alpha \partial H_\beta} - \frac{1}{\mathcal{Z}^2} \frac{\partial \mathcal{Z}}{\partial H_\alpha} \frac{\partial \mathcal{Z}}{\partial H_\beta} \right) \tag{A.17}$$

Using A.13 the second term can be expressed as:

$$\frac{1}{\mathcal{Z}^2}\frac{\partial \mathcal{Z}}{\partial H_\alpha}\frac{\partial \mathcal{Z}}{\partial H_\beta} = \left(\frac{1}{k_B T}\right)^2 \langle M_\alpha \rangle \langle M_\beta \rangle \tag{A.18}$$

The first term can be calculated by taking the derivation of eqn. A.12:

$$\frac{\partial^2 \mathcal{Z}}{\partial H_\alpha \partial H_\beta} = \frac{\partial}{\partial H_\beta}\left[\frac{1}{k_B T}\sum_\sigma M_\alpha \exp\left(-\frac{\mathcal{H}}{k_B T}\right)\right] \tag{A.19}$$

$$= \frac{1}{k_B T}\sum_\sigma M_\alpha \exp\left(-\frac{\mathcal{H}}{k_B T}\right)\left(\frac{-1}{k_B T}\right)\frac{\partial \mathcal{H}}{\partial H_\beta} \tag{A.20}$$

$$= \left(\frac{1}{k_B T}\right)^2 \sum_\sigma M_\alpha M_\beta \exp\left(-\frac{\mathcal{H}}{k_B T}\right) \tag{A.21}$$

$$= \left(\frac{1}{k_B T}\right)^2 \langle M_\alpha M_\beta \rangle \tag{A.22}$$

Combining these two into eqn. A.17 we arrive at a relation for the isothermal zero field susceptibility that can be easily computed from equilibrium properties:

$$\chi_{\alpha\beta} = \frac{1}{k_B T}\left(\langle M_\alpha M_\beta \rangle - \langle M_\alpha \rangle \langle M_\beta \rangle\right) \tag{A.23}$$

The derivation used the total magnetisation but the reduced magnetisation, $m_\alpha = M_\alpha / M_s V$, can be used to calculate the reduced susceptibility

$$\tilde{\chi}_{\alpha\beta} = \frac{\chi_{\alpha\beta}}{M_s V} = \frac{M_s V}{k_B T}\left(\langle m_\alpha m_\beta \rangle - \langle m_\alpha \rangle \langle m_\beta \rangle\right) \tag{A.24}$$

# LIST OF SYMBOLS

$a$ . . . . . unit cell size
$\alpha$ . . . . . Gilbert damping parameter
$\alpha_0$ . . . . . Morse potential width constant
$\alpha_{x,y,z}$ . . . . . directional cosines
$\alpha_{ijk}$ . . . . . linear coefficient in dielectric tensor expansion
$\mathbf{a}(\mathbf{S},t)$ . . . . . cross product drift function
$A$ . . . . . exchange stiffness constant
$A^p(\mathbf{k},\omega)$ . . velocity auto-correlation function for polarisation $p$ in Fourier space
$\mathbf{A}(\mathbf{S},t)$ . . . . . semi-implict scheme generator
$\mathbf{A}_O(\mathbf{S},t)$ . . . . . semi-implict scheme orthogonal generator
$\mathbf{b}(\mathbf{S},t)$ . . . . . cross product diffusion function
$\beta$ . . . . . magnetisation critical exponent
$\beta_{ijk}$ . . . . . cubic coefficient in dielectric tensor expansion
$c$ . . . . . unit cell height
$C(\mathbf{r}-\mathbf{r}',t)$ . . . . . equal time spin-spin correlation function
$C_e$ . . . . . electron specific heat capacity
$C_l$ . . . . . lattice specific heat capacity
$\mathcal{C}$ . . . . . Coulomb integral
$\mathrm{Cay}(\mathbf{A})$ . . . . . Cayley transform of $\mathbf{A}$
$d^{(0)}$ . . . . . FePt mediated onsite uniaxial anisotropy
$d_0$ . . . . . Curie temperature scaling constant
$d^{(1)}$ . . . . . FePt mediated two-ion anisotropy
$D$ . . . . . Morse potential energy constant
$\Delta$ . . . . . MCD ratio
$\Delta t$ . . . . . time step
$D_p$ . . . . . minimum stable grain size
$\mathbf{D}_{ij}$ . . . . . Dzyaloshinskii-Moriya interaction vector
$\delta_{ij}$ . . . . . Kronecker delta
$\delta_{\pm}$ . . . . . MCD absorption factor
$\delta(x)$ . . . . . Dirac delta function
$\boldsymbol{\delta}$ . . . . . Monte-Carlo vector step

$E_{S(T)}$ . . . . . energy of the singlet (triplet) state
$E_{\text{cont}}^{disc}$ . . . . . continuous inter-granular exchange energy
$E_{\text{exch}}^{disc}$ . . . . . discrete inter-granular exchange energy
$\mathcal{E}(\omega)$ . . . . . electric field component of light with a frequency $\omega$
$e$ . . . . . ellipticity of reversal path
$\hat{\mathbf{e}}_{ij}$ . . . . . unit vector pointing between spin i and j
$\hat{\mathbf{e}}_{u}$ . . . . . uniaxial anisotropy axis unit vector
$\varepsilon$ . . . . . spin-wave correction factor
$\varepsilon_0$ . . . . . vacuum permittivity
$\varepsilon_{ijk}$ . . . . . Levi-Cevita anti-symmetric tensor
$\varepsilon_{ij}^{(a)}$ . . . . . anti-symmetric part of dielectric tensor
$\varepsilon_{jj}^{(s)}$ . . . . . symmetric part of dielectric tensor
$f_l$ . . . . . repetition frequency of the laser pulses
$f(t)$ . . . . . temporal shape of inverse Faraday field
$\mathbf{F}_i$ . . . . . force acting on atom $i$
$\mathbf{f}(\mathbf{S},t)$ . . . . . deterministic drift function
$F$ . . . . . laser fluence
$F_0$ . . . . . probability of switching critical fluence
$\Delta F$ . . . . . probability of switching fluence width
$\mathcal{F}$ . . . . . free energy
$\Delta\mathcal{F}$ . . . . . free energy difference
$\mathcal{F}_{\text{aniso}}$ . . . . . magnetic anisotropy free energy
$\mathbb{F}\left[M_x(t)\right](\omega)$ . . . . . Fourier transform of $M_x(t)$
$G_{el}$ . . . . . electron-lattice coupling factor
$\mathbf{g}(\mathbf{S},t)$ . . . . . multiplicative diffusion tensor
$g$ . . . . . Landé g-factor
$\gamma$ . . . . . gyromagnetic ratio
$\gamma_e$ . . . . . electron heat capacity linear constant
$\gamma_{ijk}$ . . . . . quadratic coefficient in dielectric tensor expansion
$\mathbf{\Gamma}$ . . . . . lattice thermal noise term
$\mathbf{H}_i$ . . . . . effective local field for spin i
$\mathbf{H}_{\text{app}}$ . . . . . externally applied magnetic field
$\mathbf{H}_{\text{IFE}}$ . . . . . opto-magnetic field from inverse Faraday effect
$h_{\text{IFE}}$ . . . . . magnitude of inverse Faraday field
$\mathcal{H}$ . . . . . total Hamiltonian
$\mathcal{H}_{\text{Zeeman}}$ . . . . . Zeeman Hamiltonian

$\mathcal{H}_{\text{ani}}$ . . . . . anisotropy Hamiltonian terms
$\mathcal{H}_{\text{dipole}}$ . . . . . magnetic dipole Hamiltonian
$\mathcal{H}_{\text{exch}}$ . . . . . exchange Hamiltonian terms
$\mathcal{H}_{\text{spin}}$ . . . . . spin dependent Hamiltonian
$\mathcal{H}_c$ . . . . . spin-lattice coupling Hamiltonian
$\hbar$ . . . . . reduced Planck constant
$\eta$ . . . . . energy dissipation constant
$\eta$ . . . . . lattice friction
$i$ . . . . . imaginary number
$I_0$ . . . . . fluence absorption factor
$\tilde{I}$ . . . . . FePt intra-atomic exchange interaction
$J$ . . . . . total angular momentum quantum number
$\mathcal{J}$ . . . . . exchange integral
$\mathcal{J}_{\text{eff}}$ . . . . . Effective inter-granular exchange constant
$\tilde{J}_{ij}$ . . . . . FePt mediated exchange interaction between Fe atoms i and j
$J^{\text{iso}}$ . . . . . isotropic exchange constant
$\mathbb{J}$ . . . . . exchange tensor interaction
$\mathbb{J}^{\text{sym}}$ . . . . . symmetric part of the exchange tensor
$K_0$ . . . . . pseudo-dipolar coupling constant
$K_c$ . . . . . cubic anisotropy constant
$K(r_{ij})$ . . . . . pseudo-dipolar coupling strength
$K_u$ . . . . . uniaxial anisotropy constant
$k^{(0)}_{\text{Fe(Pt)}}$ . . . . . Fe (Pt) onsite uniaxial anisotropy
$k_B$ . . . . . Boltzmann constant
$k_c$ . . . . . cubic spin anisotropy constant
$k_u$ . . . . . uniaxial spin anisotropy constant
$\mathbf{k}$ . . . . . lattice wave vector
$l$ . . . . . orbital angular momentum quantum number
$\lambda$ . . . . . atomistic damping constant and coupling to heat bath
$L$ . . . . . total orbital angular momentum quantum number
$\hat{L}_{r/v/s}$ . . . . . Liouville operator for position, velocity or spin
$\mathbf{M}$ . . . . . net magnetisation
$M^0_\nu$ . . . . . magnitude of polarised Pt moment
$M_s$ . . . . . saturation net magnetisation
$\mathbf{m}$ . . . . . reduced magnetisation (magnetisation per atom)
$m_e$ . . . . . equilibrium reduced magnetisation

$m_i$ . . . . . mass of atom $i$
$m^\infty$ . . . . . equilibrium induced magnetisation
$m_s$ . . . . . spin magnetic quantum number
$m_t$ . . . . . final value of the magnetisation after temperature step
$\boldsymbol{\mu}$ . . . . . vector atomic magnetic moment
$\mu_0$ . . . . . magnetic constant (permeability of free space)
$\mu_B$ . . . . . Bohr magneton
$\mu_s$ . . . . . spin magnetic moment
$n_+$ . . . . ratio of grains with magnetisation in the high absorption orientation
$n_-$ . . . . . ratio of grains with magnetisation in the low absorption orientation
$n_\pm^\infty$ . . . . . equilibrium solution for $n_\pm$
$\hat{\mathbf{n}}$ . . . . . film normal vector
$N_e^{\text{maj}}$ . . . . . number of majority electrons
$N_e^{\text{min}}$ . . . . . number of majority electrons
$\nu$ . . . . . Curie temperature scaling power
$P(t)$ . . . . . laser heating power
$P(\theta, \phi)$ . . . . . Boltzmann probability
$P_s$ . . . . . probability of switching
$P_\infty$ . . . . . probability of switching fit parameter
$p_c$ . . . . . percolation threshold
$p_i$ . . . . . probability of occupying state $i$
$\mathcal{P}$ . . . . . probability of accepting Monte-Carlo state
$\phi$ . . . . . spherical polar coordinates - Polar angle
$\phi_{a(b)}$ . . . . . single electron spatial wave-function for state $a(b)$
$\phi(r_{ij})$ . . . . . pairwise interatomic potential energy between atoms $i$ and $j$
$\mathbf{\Phi}_{\text{sym/anti}}$ . . . . . symmetric / anti-symmetric spatial many-body wave-function
$\mathbf{\Psi}$ . . . . . Tttal many-body wave-function
$\mathbf{\Psi}_S$ . . . . . singlet total wave-function
$\mathbf{\Psi}_T$ . . . . . triplet total wave-function
$\mathcal{R}$ . . . . . Rayleigh dissipation functional
$r_0$ . . . . . Morse potential minimum position
$r_c$ . . . . . exchange function cut off radius
$\mathbf{r}_i$ . . . . . position of atom $i$
$\mathbf{r}_{ij}$ . . . . . separation vector between spin i and j
$\hat{\mathbf{r}}_{ij}$ . . . . . separation unit vector
$r_{ij}$ . . . . . magnitude of separation vector

$\mathcal{S}(\mathbf{k},\omega)$ . . . . . spin dynamical structure
$S$ . . . . . total spin quantum number
$\mathbf{S}$ . . . . . normalised spin vector
$\mathbf{S}_i$ . . . . . spin vector at site i
$\sigma_{\pm}$ . . . . . left (-) and right (+) circular polarisation of light
$\mathbf{T}$ . . . . . macroscopic torque
$T$ . . . . . temperature
$T^*$ . . . . . critical temperature for linear reversal
$T_C$ . . . . . Curie temperature
$T_C^{\infty}$ . . . . . Curie temperature for an infinitely large system
$T_e$ . . . . . electron temperature
$T_l$ . . . . . lattice temperature
$T_s$ . . . . . spin temperature
$t_0$ . . . . . centre of laser pulse
$t_0^1$ . . . . . minimum pulse duration from $m_z = 1$ to $m_z = 0$
$\tau$ . . . . . characteristic switching time
$\tau_+$ . . . . . switching time from + to - orientation
$\tau_-$ . . . . . switching time from - to - orientation
$\tau_{ij}^{-1}$ . . . . . transition time between state $i$ and $j$
$\tau_0$ . . . . . characteristic attempt time
$\tau_l$ . . . . . laser pulse width
$\tau_p h$ . . . . . cooling time constant
$\mathrm{Tr}(\mathbb{A})$ . . . . . trace of tensor A
$\theta$ . . . . . spherical polar coordinates - Azimuthal angle
$U(r_{ij})$ . . . . . pairwise inter-atomic potential energy
$(u,v,w)$ . . . . . independent Gaussian random numbers
$\mathbf{v}_i$ . . . . . velocity of atom $i$
$V$ . . . . . grain volume
$\mathbf{W}$ . . . . . vector Weiner process
$\Delta\mathbf{W}$ . . . . . discrete differential of the vector Weiner process
$d\mathbf{W}$ . . . . . differential of the vector Weiner process
$\mathcal{W}_{ij}$ . . . . . transition matrix
$\omega_d$ . . . . . damping frequency
$\omega_p$ . . . . . precession frequency
$\mathbf{X}(t)$ . . . . . extended variable
$X_{\mathrm{sym/anti}}$ . . . . . symmetric / anti-symmetric spin many-body wave-function

$\chi_{\alpha(\beta)}$ . . . . . single electron spin wave-function for state $\alpha(\beta)$
$\chi_\nu$ . . . . . Pt local susceptibility
$\tilde{\chi}_\parallel$ . . . . . reduced longitudinal susceptibility
$\tilde{\chi}_\perp$ . . . . . reduced transverse susceptibility
$\boldsymbol{\xi}_i$ . . . . . thermal noise vector for spin i
$z$ . . . . . number of nearest neighbours
$\mathcal{Z}$ . . . . . Partition function

# LIST OF ABBREVIATIONS

AOS . . . . . All Optical Switching
ASD . . . . . Atomistic Spin Dynamics
BER . . . . . Bit Error Rate
BPMR . . . . . Bit Patterned Magnetic Recording
CLSDA . . . . . Constrained Local Spin Density Approximation
CMC . . . . . Constrained Monte-Carlo
DFT . . . . . Density Functional Theory
DM . . . . . Dzyaloshinskii-Moriya (interaction)
HAMR . . . . . Heat Assisted Magnetic Recording
HD-AOS . . . . . Helicity Dependent All Optical Switching
IFE . . . . . Inverse Faraday Effect
LD . . . . . Langevin Dynamics
LL . . . . . Landau-Lifshitz
LLG . . . . . Landau-Lifshitz-Gilbert
MAMR . . . . . Microwave Assisted Magnetic Recording
MC . . . . . Monte-Carlo
MCD . . . . . Magnetic Circular Dichroism
MD . . . . . Molecular Dynamics
RE-TM . . . . . Rare Earth - Transition Metal
SD . . . . . Spin Dynamics
sLLG . . . . . Stochastic Landau-Lifshitz-Gilbert
TIMS . . . . . Thermally Induced Magnetisation Switching

# REFERENCES


[1] R. L. Stamps, S. Breitkreutz, J. Åkerman, A. V. Chumak, Y. Otani, G. E. W. Bauer, J.-U. Thiele, M. Bowen, S. a. Majetich, M. Kläui, I. L. Prejbeanu, B. Dieny, N. M. Dempsey, and B. Hillebrands, "The 2014 Magnetism Roadmap," *J. Phys. D. Appl. Phys.*, vol. 47, p. 333001, 2014.

[2] M. Hilbert and P. López, "The world's technological capacity to store, communicate, and compute information.," *Science*, vol. 332, pp. 60–65, apr 2011.

[3] G. Binasch, P. Grünberg, F. Saurenbach, and W. Zinn, "Enhanced magnetoresistance in layered magnetic structures with antiferromagnetic interlayer exchange," *Phys. Rev. B*, vol. 39, no. 7, pp. 4828–4830, 1989.

[4] M. N. Baibich, J. M. Broto, A. Fert, F. Nguyen Van Dau, F. Petroff, P. Eitenne, G. Creuzet, A. Friederich, and J. Chazelas, "Giant Magnetosresistance of (001)Fe/(001)Cr Magnetic Superlattices," *Phys. Rev. Lett.*, vol. 61, no. 21, pp. 2472–2475, 1988.

[5] R. F. L. Evans, W. J. Fan, P. Chureemart, T. A. Ostler, M. O. A. Ellis, and R. W. Chantrell, "Atomistic spin model simulations of magnetic nanomaterials.," *J. Phys. Condens. Matter*, vol. 26, p. 103202, mar 2014.

[6] S. Piramanayagam and K. Srinivasan, "Recording media research for future hard disk drives," *J. Magn. Magn. Mater.*, vol. 321, pp. 485–494, mar 2009.

[7] L. Néel, "Théorie du traînage magnétique des ferromagnétiques en grains fins avec application aux terres cuites," *Ann. Géophysique*, vol. 5, pp. 99–136, 1949.

[8] R. F. L. Evans, R. W. Chantrell, U. Nowak, A. Lyberatos, and H.-J. Richter, "Thermally induced error: Density limit for magnetic data storage," *Appl. Phys. Lett.*, vol. 100, no. 10, p. 102402, 2012.

[9] Y. Shiroishi, K. Fukuda, I. Tagawa, H. Iwasaki, S. Takenoiri, H. Tanaka, H. Mutoh, and N. Yoshikawa, "Future Options for HDD Storage," *IEEE Trans. Magn.*, vol. 45, pp. 3816–3822, oct 2009.

[10] D. Weller, G. Parker, O. Mosendz, E. Champion, B. Stipe, X. Wang, T. Klemmer, G. Ju, and A. Ajan, "A HAMR media technology roadmap to an areal density of 4 Tb/in2," *IEEE Trans. Magn.*, vol. 50, no. 1, 2014.

[11] D. Thompson and J. Best, "The future of magnetic data storage technology," *IBM J. Res. Dev.*, vol. 44, no. 3, pp. 311–322, 2000.

[12] D. Weller, A. Moser, L. Folks, and M. Best, "High Ku materials approach to 100 Gbits/in2," *IEEE Trans. Magn.*, vol. 36, no. 1, pp. 10–15, 2000.

[13] L. Zhang, Y. K. Takahashi, a. Perumal, and K. Hono, "L10-ordered high coercivity (FePt)AgC granular thin films for perpendicular recording," *J. Magn. Magn. Mater.*, vol. 322, no. 18, pp. 2658–2664, 2010.

[14] D. Weller, O. Mosendz, G. Parker, S. Pisana, and T. S. Santos, "L10 FePtX-Y media for heat-assisted magnetic recording," *Phys. Status Solidi*, vol. 210, pp. 1245–1260, 2013.

[15] J. U. Thiele, M. E. Best, M. F. Toney, and D. Weller, "Grain size control in FePt thin films by Ar-ion etched Pt seed layers," *IEEE Trans. Magn.*, vol. 37, no. 4 I, pp. 1271–1273, 2001.

[16] R. Cuadrado and R. W. Chantrell, "Electronic and magnetic properties of bimetallic L10 cuboctahedral clusters by means of fully relativistic density-functional-based calculations," *Phys. Rev. B*, vol. 86, p. 224415, 2012.

[17] R. V. Chepulskii and W. H. Butler, "Ab initio magnetocrystalline anisotropy at nanoscale: The case of FePt," *Appl. Phys. Lett.*, vol. 100, no. 14, p. 142405, 2012.

[18] T. W. McDaniel, "Application of Landau-Lifshitz-Bloch dynamics to grain switching in heat-assisted magnetic recording," *J. Appl. Phys.*, vol. 112, no. 1, p. 013914, 2012.

[19] S. Greaves, "Micromagnetic Simulations of Magnetic Recording Media," *High Perform. Comput. Vector Syst. 2007*, pp. 229–244, 2007.

[20] O. N. Mryasov, U. Nowak, R. W. Chantrell, and K. Y. Guslienko, "Temperature-dependent magnetic properties of FePt: Effective spin Hamiltonian model," *Europhys. Lett.*, vol. 69, no. 5, pp. 805–811, 2005.

[21] O. N. Mryasov, "Magnetic interactions and phase transformations in FeM, M=(Pt, Rh) ordered alloys," *Phase Transitions*, vol. 78, pp. 197–208, jan 2005.

[22] M. O. A. Ellis, R. F. L. Evans, T. A. Ostler, J. Barker, U. Atxitia, O. Chubykalo-Fesenko, and R. W. Chantrell, "The Landau Lifshitz equation in atomistic models," *Low Temp. Phys.*, vol. 41, no. 9, pp. 908–916, 2015.

[23] N. Kazantseva, D. Hinzke, R. W. Chantrell, and U. Nowak, "Linear and elliptical magnetization reversal close to the Curie temperature," *EPL (Europhysics Lett.*, vol. 86, p. 27006, apr 2009.

[24] V. Sokalski, D. E. Laughlin, and J.-G. Zhu, "Experimental modeling of intergranular exchange coupling for perpendicular thin film media," *Appl. Phys. Lett.*, vol. 95, no. 10, p. 102507, 2009.

[25] R. F. L. Evans, Q. Coopman, S. Devos, W. J. Fan, O. Hovorka, and R. W. Chantrell, "Atomistic calculation of the thickness and temperature dependence of exchange coupling through a dilute magnetic oxide," *J. Phys. D. Appl. Phys.*, vol. 47, p. 502001, 2014.

[26] C.-H. Lambert, S. Mangin, B. S. D. C. S. Varaprasad, Y. K. Takahashi, M. Hehn, M. Cinchetti, G. Malinowski, K. Hono, Y. Fainman, M. Aeschlimann, and E. E. Fullerton, "All-optical control of ferromagnetic thin films and nanostructures.," *Science (80-. ).*, vol. 345, pp. 1337–1340, aug 2014.

[27] P.-W. Ma, C. Woo, and S. Dudarev, "Large-scale simulation of the spin-lattice dynamics in ferromagnetic iron," *Phys. Rev. B*, vol. 78, p. 024434, jul 2008.

[28] K. Binder, "Applications of Monte Carlo methods to statistical physics," *Reports Prog. Phys.*, vol. 60, pp. 487–559, 1997.

[29] T. A. Ostler, J. Barker, R. F. L. Evans, R. W. Chantrell, U. Atxitia, O. Chubykalo-Fesenko, S. El Moussaoui, L. Le Guyader, E. Mengotti, L. J. Heyderman, F. Nolting, A. Tsukamoto, A. Itoh, D. Afanasiev, B. A. Ivanov, A. M. Kalashnikova, K. Vahaplar, J. Mentink, A. Kirilyuk, T. Rasing, and A. V. Kimel, "Ultrafast heating as a sufficient stimulus for magnetization reversal in a ferrimagnet.," *Nat. Commun.*, vol. 3, p. 666, jan 2012.

[30] J. Barker, R. F. L. Evans, R. W. Chantrell, D. Hinzke, and U. Nowak, "Atomistic spin model simulation of magnetic reversal modes near the Curie point," *Appl. Phys. Lett.*, vol. 97, no. 19, p. 192504, 2010.

[31] R. F. L. Evans, T. A. Ostler, R. W. Chantrell, I. Radu, and T. Rasing, "Ultrafast thermally induced magnetic switching in synthetic ferrimagnets," *Appl. Phys. Lett.*, vol. 104, p. 082410, feb 2014.

[32] N. Kazantseva, D. Hinzke, U. Nowak, R. W. Chantrell, U. Atxitia, and O. Chubykalo-Fesenko, "Towards multiscale modeling of magnetic materials: Simulations of FePt," *Phys. Rev. B*, vol. 77, p. 184428, may 2008.

[33] B. Skubic, J. Hellsvik, L. Nordström, and O. Eriksson, "A method for atomistic spin dynamics simulations: implementation and examples," *J. Phys. Condens. Matter*, vol. 20, p. 315203, aug 2008.

[34] S. Blundell, *Magnetism in Condensed Matter*. Oxford Master Series in Condensed Matter Physics, OUP Oxford, 2001.

[35] J. Stöhr and H. C. Siegmann, *Magnetism: From Fundamentals to Nanoscale Dynamics*. Springer Series in Solid-State Sciences, Springer Berlin Heidelberg, 2006.

[36] I. Turek, J. Kudrnovský, G. Bihlmayer, and S. Blugel, "Ab initio theory of exchange interactions and the Curie temperature of bulk Gd," *J. Phys. Condens. Matter*, vol. 15, p. 2771, 2003.

[37] M. Pajda, J. Kudrnovský, I. Turek, V. Drchal, and P. Bruno, "Ab initio calculations of exchange interactions, spin-wave stiffness constants, and Curie temperatures of Fe, Co, and Ni," *Phys. Rev. B*, vol. 64, p. 174402, oct 2001.

[38] I. Dzyaloshinsky, "A thermodynamic theory of weak ferromagnetism of antiferromagnetics," *J. Phys. Chem. Solids*, vol. 4, no. 4, pp. 241–255, 1958.

[39] T. Moriya, "Anisotropic superexchange interaction and weak ferromagnetism," *Phys. Rev.*, vol. 120, no. 1, pp. 91–98, 1960.

[40] C. J. Aas, P. J. Hasnip, and R. Cuadrado, "Exchange coupling and magnetic anisotropy at Fe/FePt interfaces," *Phys. Rev. B*, vol. 88, p. 174409, 2013.

[41] P. Asselin, R. Evans, J. Barker, R. Chantrell, R. Yanes, O. Chubykalo-Fesenko, D. Hinzke, and U. Nowak, "Constrained Monte Carlo method and calculation

of the temperature dependence of magnetic anisotropy," *Phys. Rev. B*, vol. 82, p. 054415, aug 2010.

[42] J. H. Van Vleck, "On the anisotropy of cubic ferromagnetic crystals," *Phys. Rev.*, vol. 52, no. 11, pp. 1178–1198, 1937.

[43] E. R. Callen and H. B. Callen, "Static magnetoelastic coupling in cubic crystals," *Phys. Rev.*, vol. 129, no. 2, p. 578, 1963.

[44] J. M. Yeomans, *Statistical Mechanics of Phase Transitions*. Clarendon Press, 1992.

[45] L. D. Landau and E. M. Lifshitz, "Theory of the dispersion of magnetic permeability in ferromagnetic bodies," *Phys. Z. Sowietunion*, vol. 8, no. 153, pp. 14–22, 1935.

[46] G. V. Skrotskii, "The Landau-Lifshitz equation revisited," *Physics (College. Park. Md).*, vol. 27, no. 12, p. 977, 1984.

[47] S. Iida, "The difference between gilbert's and landau-lifshitz's equations," *J. Phys. Chem. Solids*, vol. 24, pp. 625–630, may 1963.

[48] T. Gilbert, "Classics in Magnetics A Phenomenological Theory of Damping in Ferromagnetic Materials," *IEEE Trans. Magn.*, vol. 40, pp. 3443–3449, nov 2004.

[49] G. Woltersdorf, M. Kiessling, G. Meyer, J. Thiele, and C. Back, "Damping by Slow Relaxing Rare Earth Impurities in Ni80Fe20," *Phys. Rev. Lett.*, vol. 102, no. 25, p. 257602, 2009.

[50] J. Becker, O. Mosendz, D. Weller, A. Kirilyuk, J. C. Maan, P. C. M. Christianen, T. Rasing, and A. V. Kimel, "Laser induced spin precession in highly anisotropic granular L10 FePt," *Appl. Phys. Lett.*, vol. 104, p. 152412, apr 2014.

[51] S. Mizukami, S. Iihama, N. Inami, T. Hiratsuka, G. Kim, H. Naganuma, M. Oogane, and Y. Ando, "Fast magnetization precession observed in L1_0-FePt epitaxial thin film," *Appl. Phys. Lett.*, vol. 98, no. 5, p. 052501, 2011.

[52] W. F. Brown, "Thermal fluctuations of a single-domain particle," *Phys. Rev.*, vol. 130, no. 5, 1963.

[53] H. Risken, *The Fokker-Planck Equation: Methods of Solution and Applications*. Lecture Notes in Mathematics, Springer Berlin Heidelberg, 1996.

[54] P. E. Kloeden and E. Platen, *Numerical Solution of Stochastic Differential Equations*. Stochastic Modelling and Applied Probability, Springer Berlin Heidelberg, 2011.

[55] J. H. Mentink, M. V. Tretyakov, A. Fasolino, M. I. Katsnelson, and T. Rasing, "Stable and fast semi-implicit integration of the stochastic LandauLifshitz equation," *J. Phys. Condens. Matter*, vol. 22, no. 17, p. 176001, 2010.

[56] M. D'Aquino, C. Serpico, and G. Miano, "Geometrical integration of Landau-Lifshitz-Gilbert equation based on the mid-point rule," *J. Comput. Phys.*, vol. 209, pp. 730–753, nov 2005.

[57] M. D'Aquino, C. Serpico, G. Coppola, I. D. Mayergoyz, and G. Bertotti, "Mid-point numerical technique for stochastic Landau-Lifshitz-Gilbert dynamics," *J. Appl. Phys.*, vol. 99, no. 8, p. 08B905, 2006.

[58] D. Lewis and N. Nigam, "Geometric integration on spheres and some interesting applications," *J. Comput. Appl. Math.*, vol. 151, pp. 141 – 170, 2003.

[59] U. Nowak, "Classical spin models," in *Handb. Magn. Adv. Magn. Mater. Vol 2* (H. Kronmuller and S. Parkin, eds.), Hoboken, N.J.: John Wiley & Sons, Ltd, mar 2007.

[60] O. Bottauscio and A. Manzin, "Efficiency of the geometric integration of Landau-Lifshitz-Gilbert equation based on Cayley transform," *IEEE Trans. Magn.*, vol. 47, no. 5, pp. 1154 – 1157, 2011.

[61] D. A. Garanin, "Fokker-Planck and Landau-Lifshitz-Bloch equations for classical ferromagnets," *Phys. Rev. B*, vol. 55, p. 3050, feb 1997.

[62] H. Kachkachi and D. A. Garanin, "Magnetic free energy at elevated temperatures and hysteresis of magnetic particles," *Physica A*, vol. 291, pp. 485–500, mar 2001.

[63] A. Lyberatos, D. Weller, and G. J. Parker, "Finite size effects in L1_0-FePt nanoparticles," *J. Appl. Phys.*, vol. 114, no. 23, p. 233904, 2013.

[64] O. Hovorka, S. Devos, Q. Coopman, W. J. Fan, C. J. Aas, R. F. L. Evans, and X. Chen, "The Curie temperature distribution of FePt granular magnetic recording media," *Appl. Phys. Lett.*, vol. 101, no. 052406, pp. 1–5, 2012.

[65] P.-W. Huang, X. Chen, and R. H. Victora, "Time Dependence of Magnetic Anisotropy at Finite Temperature for Homogeneous and Composite Media," *IEEE Trans. Magn.*, vol. 48, pp. 3188–3191, nov 2012.

[66] S. D. Granz and M. H. Kryder, "Intergranular Exchange Coupling in FePt:X:FePt (X= B, C, SiO_x, Cr and TaO_x) Thin Films for Heat Assisted Magnetic Recording," *IEEE Trans. Magn.*, vol. 48, no. 11, pp. 2746–2748, 2012.

[67] R. Araki, Y. Takahashi, I. Takekuma, and S. Narishige, "High-Resolution TEM Analysis of Perpendicular CoCrPt-SiO_2 Media," *IEEE Trans. Magn.*, vol. 44, no. 11, pp. 3496–3498, 2008.

[68] S. Greaves, "Readwrite issues in ultra-high density perpendicular recording," *J. Magn. Magn. Mater.*, vol. 321, pp. 477–484, mar 2009.

[69] M. Donahue, "Exchange energy representations in computational micromagnetics," *Phys. B Condens. Matter*, vol. 233, pp. 272–278, jun 1997.

[70] D. Hinzke, N. Kazantseva, U. Nowak, O. Mryasov, P. Asselin, and R. Chantrell, "Domain wall properties of FePt: From Bloch to linear walls," *Phys. Rev. B*, vol. 77, p. 094407, mar 2008.

[71] U. Atxitia, D. Hinzke, O. Chubykalo-Fesenko, U. Nowak, H. Kachkachi, O. Mryasov, R. Evans, and R. W. Chantrell, "Multiscale modeling of magnetic materials: Temperature dependence of the exchange stiffness," *Phys. Rev. B*, vol. 82, p. 134440, oct 2010.

[72] E. Y. Huang and M. H. Kryder, "Effects of temperature on intergranular exchange coupling in L10 FePt thin films," *J. Appl. Phys.*, vol. 115, no. 21, p. 213906, 2014.

[73] E. Beaurepaire, J. Merle, A. Daunois, and J. Bigot, "Ultrafast spin dynamics in ferromagnetic nickel.," *Phys. Rev. Lett.*, vol. 76, pp. 4250–4253, may 1996.

[74] C. Stanciu, F. Hansteen, A. V. Kimel, A. Kirilyuk, A. Tsukamoto, A. Itoh, and T. Rasing, "All-Optical Magnetic Recording with Circularly Polarized Light," *Phys. Rev. Lett.*, vol. 99, p. 47601, jul 2007.

[75] J. Barker, U. Atxitia, T. A. Ostler, O. Hovorka, R. W. Chantrell, O. Chubykalo-Fesenko, and R. W. Chantrell, "Two-magnon bound state causes ultrafast thermally induced magnetisation switching Supplementary Information," *Sci. Rep.*, vol. 3, p. 3262, jan 2013.

[76] R. Hertel, "Theory of the inverse Faraday effect in metals," *J. Magn. Magn. Mater.*, vol. 303, pp. L1–L4, aug 2006.

[77] K. Vahaplar, A. M. Kalashnikova, A. V. Kimel, D. Hinzke, U. Nowak, R. Chantrell, A. Tsukamoto, A. Itoh, A. Kirilyuk, and T. Rasing, "Ultrafast Path for Optical Magnetization Reversal via a Strongly Nonequilibrium State," *Phys. Rev. Lett.*, vol. 103, pp. 66–69, sep 2009.

[78] M. I. Kaganov, I. M. Lifshitz, and L. V. Tanatarov, "Relaxation between electrons and crystalline lattices.," *JETP*, vol. 173, 1957.

[79] S. I. Anisimov, B. L. Kapeliovich, and T. L. Perelman, "Electron emission from metal surfaces exposed to ultrashort laser pulses," *Sov. Phys.-JETP*, vol. 39, no. 2, pp. 375–377, 1974.

[80] J. Chen, D. Tzou, and J. Beraun, "A semiclassical two-temperature model for ultrafast laser heating," *Int. J. Heat Mass Transf.*, vol. 49, pp. 307–316, jan 2006.

[81] J. Mendil, P. Nieves, O. Chubykalo-Fesenko, J. Walowski, T. Santos, S. Pisana, and M. Münzenberg, "Resolving the role of femtosecond heated electrons in ultrafast spin dynamics.," *Sci. Rep.*, vol. 4, p. 3980, jan 2014.

[82] M. O. A. Ellis, T. A. Ostler, and R. W. Chantrell, "Classical spin model of the relaxation dynamics of rare-earth doped permalloy," *Phys. Rev. B*, vol. 86, p. 174418, 2012.

[83] P.-W. Ma, S. Dudarev, A. Semenov, and C. Woo, "Temperature for a dynamic spin ensemble," *Phys. Rev. E*, vol. 82, p. 031111, sep 2010.

[84] P.-W. Ma, S. Dudarev, and C. Woo, "Spin-lattice-electron dynamics simulations of magnetic materials," *Phys. Rev. B*, vol. 85, pp. 30–37, may 2012.

[85] I. Radu, K. Vahaplar, C. Stamm, T. Kachel, N. Pontius, H. Dürr, T. A. Ostler, J. Barker, R. F. L. Evans, R. W. Chantrell, A. Tsukamoto, A. Itoh, A. Kirilyuk, T. Rasing, and A. V. Kimel, "Transient ferromagnetic-like state

mediating ultrafast reversal of antiferromagnetically coupled spins," *Nature*, pp. 5–9, mar 2011.

[86] L. Pitaevskii, "Electric forces in a transparent dispersive medium," *Sov. Phys. JETP*, vol. 12, no. 5, p. 1008, 1961.

[87] J. P. van der Ziel, P. S. Pershan, and D. Malmstrom, "Optically-Induced Magnetization Resultin From The Inverse Faraday Effect," *Phys. Rev. Lett.*, vol. 15, no. 5, 1965.

[88] A. V. Kimel, A. Kirilyuk, and T. Rasing, "Femtosecond opto-magnetism: ultrafast laser manipulation of magnetic materials," *Laser Photonics Rev.*, vol. 1, pp. 275–287, dec 2007.

[89] T. Yoshino, "Simple theory of the inverse Faraday effect with relationship to optical constants N and K," *J. Magn. Magn. Mater.*, vol. 323, pp. 2531–2532, oct 2011.

[90] Z. H. Cen, B. X. Xu, J. F. Hu, J. M. Li, K. M. Cher, Y. T. Toh, K. D. Ye, and J. Zhang, "Optical property study of FePt-C nanocomposite thin film for heat-assisted magnetic recording," *Opt. Express*, vol. 21, no. 8, pp. 9906–9914, 2013.

[91] M. Battiato, G. Barbalinardo, and P. M. Oppeneer, "Quantum theory of the inverse Faraday effect," *Phys. Rev. B*, vol. 89, p. 014413, jan 2014.

[92] A. R. Khorsand, M. Savoini, A. Kirilyuk, A. V. Kimel, A. Tsukamoto, A. Itoh, and T. Rasing, "Role of magnetic circular dichroism in all-optical magnetic recording," *Phys. Rev. Lett.*, vol. 108, p. 127205, 2012.

[93] A. Lyberatos, D. Weller, and G. J. Parker, "Memory Erasure and Write Field Requirements in HAMR Using L1_0 -FePt Nanoparticles," *IEEE Trans. Magn.*, vol. 50, no. 11, 2014.

[94] K. Sato, A. Mizusawa, K. Ishida, T. Seki, T. Shima, and K. Takanashi, "Magneto-Optical Spectra of Ordered and Disordered FePt Films Prepared at Reduced Temperatures," *Trans. Magn. Soc. Japan*, vol. 4, pp. 297–300, 2004.

[95] S. Karakurt, R. Chantrell, and U. Nowak, "A model of damping due to spin-lattice interaction," *J. Magn. Magn. Mater.*, vol. 316, pp. e280–e282, sep 2007.

[96] D. Beaujouan, P. Thibaudeau, and C. Barreteau, "Anisotropic magnetic molecular dynamics of cobalt nanowires," *Phys. Rev. B*, vol. 86, p. 174409, nov 2012.

[97] P.-W. Ma and S. L. Dudarev, "Longitudinal magnetic fluctuations in Langevin spin dynamics," *Phys. Rev. B*, vol. 86, p. 054416, aug 2012.

[98] L. A. Girifalco and V. G. Weizer, "Application of the Morse potential function to cubic metals," *Phys. Rev.*, vol. 114, no. 3, pp. 687–690, 1959.

[99] X. D. Dai, Y. Kong, J. H. Li, and B. X. Liu, "Extended FinnisSinclair potential for bcc and fcc metals and alloys," *J. Phys. Condens. Matter*, vol. 18, pp. 4527–4542, may 2006.

[100] C. Kittel, *Introduction to Solid State Physics*. New York: Wiley, 7th editio ed., 1996.

[101] P. Derlet and S. Dudarev, "Million-atom molecular dynamics simulations of magnetic iron," *Prog. Mater. Sci.*, vol. 52, pp. 299–318, feb 2007.

[102] CIAAW, "(2015, Aug. 1). Atomic weights of the elements 2015[On-line]. Available: ciaaw.org/atomic-weights.htm,"

[103] M. Suzuki, "General nonsymmetric higher-order decomposition of exponential operators and symplectic integrators," *Phys. Lett. A*, vol. 165, pp. 387–395, 1992.

[104] I. Omelyan, I. Mryglod, and R. Folk, "Algorithm for Molecular Dynamics Simulations of Spin Liquids," *Phys. Rev. Lett.*, vol. 86, pp. 898–901, jan 2001.

[105] I. Omelyan, I. Mryglod, and R. Folk, "Optimized Verlet-like algorithms for molecular dynamics simulations," *Phys. Rev. E*, vol. 65, p. 056706, may 2002.

[106] S.-H. Tsai, M. Krech, and D. P. Landau, "Symplectic Integration Methods in Molecular and Spin Dynamics Simulations," *Brazilian J. Phys.*, vol. 34, no. 2A, pp. 384–391, 2004.

[107] S.-H. Tsai, H. K. Lee, and D. P. Landau, "Molecular and spin dynamics simulations using modern integration methods," *Am. J. Phys.*, vol. 73, no. 7, p. 615, 2005.

[108] F. Körmann, A. Dick, B. Grabowski, B. Hallstedt, T. Hickel, and J. Neugebauer, "Free energy of bcc iron: Integrated ab initio derivation of vibrational,

electronic, and magnetic contributions," *Phys. Rev. B*, vol. 78, p. 033102, jul 2008.

[109] P. Heino, "Dispersion and thermal resistivity in silicon nanofilms by molecular dynamics," *Eur. Phys. J. B*, vol. 60, pp. 171–179, dec 2007.

[110] N. Papanicolaou, I. Lagaris, and G. Evangelakis, "Modification of phonon spectral densities of the (001) copper surface due to copper adatoms by molecular dynamics simulation," 1995.

[111] W. Setyawan and S. Curtarolo, "High-throughput electronic band structure calculations: Challenges and tools," *Comput. Mater. Sci.*, vol. 49, pp. 299–312, aug 2010.

[112] V. Minkiewicz, G. Shirane, and R. Nathans, "Phonon dispersion relation for iron," *Phys. Rev.*, vol. 162, no. 3, 1967.

[113] M. Krech, A. Bunker, and D. Landau, "Fast spin dynamics algorithms for classical spin systems," *Comput. Phys. Commun.*, vol. 111, pp. 1–13, jun 1998.

[114] X. Tao, D. Landau, T. Schulthess, and G. Stocks, "Spin Waves in Paramagnetic bcc Iron: Spin Dynamics Simulations," *Phys. Rev. Lett.*, vol. 95, pp. 1–4, aug 2005.

[115] K. Chen and D. P. Landau, "Spin-dynamics study of the dynamic critical behavior of the three-dimensional classical Heisenberg ferromagnet," *Phys. Rev. B*, vol. 49, no. 5, pp. 3266–3274, 1994.

[116] A. I. Akhiezer, V. G. Bar'yakhtar, and S. V. Peletminskii, *Spin Waves*. Amsterdam: North-Holland Publishing Company, 1st ed., 1968.

[117] K. Usadel, "Temperature-dependent dynamical behavior of nanoparticles as probed by ferromagnetic resonance using Landau-Lifshitz-Gilbert dynamics in a classical spin model," *Phys. Rev. B*, vol. 73, p. 212405, 2006.

[118] A. Melnikov, I. Radu, U. Bovensiepen, O. Krupin, K. Starke, E. Matthias, and M. Wolf, "Coherent optical phonons and parametrically coupled magnons induced by femtosecond laser excitation of the Gd(0001) surface.," *Phys. Rev. Lett.*, vol. 91, no. 22, p. 227403, 2003.

[119] U. Bovensiepen, "Coherent and incoherent excitations of the Gd(0001) surface on ultrafast timescales," *J. Phys. Condens. Matter*, vol. 19, no. 8, p. 083201, 2007.

[120] U. Bovensiepen, "Ultra-fast dynamics of coherent lattice and spin excitations at the Gd(0001) surface," *Appl. Phys. A Mater. Sci. Process.*, vol. 82, no. 3 SPEC. ISS., pp. 395–402, 2006.